11-10-2018

The Effects of Pressure and Magnetic Field on Phase Transitions and Related Physical Properties in Solid State Caloric Materials

Ahmad Ikhwan Us Saleheen
Louisiana State University and Agricultural and Mechanical College

THE EFFECTS OF PRESSURE AND MAGNETIC FIELD ON PHASE TRANSITIONS AND RELATED PHYSICAL PROPERTIES IN SOLID STATE CALORIC MATERIALS

A Dissertation

Submitted to the Graduate Faculty of the
Louisiana State University and
Agricultural and Mechanical College
in partial fulfillment of the
requirements for the degree of
Doctor of Philosophy

in

Department of Physics and Astronomy

by
Ahmad Ikhwan Us Saleheen
B.S., University of Dhaka, 2009
December 2018

Dedicated to the memory of my late grandfather,

Mr. M. A. Rashid

Acknowledgments

During my years as a doctoral student at the Louisiana State University, I have had the good fortune of being acquainted with a number of people, whose kindness, guidance, and cooperation helped me to arrive at this point. First of all, I would like to express my sincere gratitude to my adviser, Professor Shane Stadler. In my second year at LSU, he introduced me to his lab, and I was instantly drawn into the world of experimental condensed matter physics. Without his guidance, mentoring, and support, I would not have come this far. I also appreciate the academic freedom he has given me to explore ideas and projects, which helped me to mature as a researcher.

Another person I am indebted to is Dr. Tapas Samanta, who had been a postdoctoral researcher in our group. He had generously shared his knowledge with me, and involved me in many of his projects. I will always cherish the scientific (and not so scientific) discussions I have had with him. I am especially grateful to the current postdoctoral researcher of our group, Dr. Jing-Han Chen, for his invaluable suggestions, insights, cooperation, and coffee-breaks. Early in my career, I was fortunate enough to work with Dr. Joseph Prestigiacomo, who trained me to use the experimental devices, and taught me a wide variety of experimental techniques and skills.

My research owes a great deal to Professor David Young. He has generously allowed us to use his laboratory where we synthesized all of our samples. I am indebted to him for his guidance and help. I would also like to thank Professor Philip Adams and Professor John DiTusa for allowing me to use their laboratories, and conducting measurements. I thank Professor Dana Browne and Professor Mark Jarrell for their support throughout my doctoral studies. I am grateful to Professor Hwang Lee, Professor Daniel Sheehy, and Professor Pramod Achar for being in my graduate committee.

I am honored to have Dr. Amir Javaid as my friend, who has helped me in writing a code, which was instrumental in finishing one of my projects. His kind advice and encouragement are invaluable to me. I am indebted to Dr. Mojammel Alam Khan for

his help in the laboratory. I express my sincere gratitude to Dr. Chetan Dhital, Frank Womack, Alok Shankar, Daniel Lepkowski, Matthew Champagne, and Dr. Amber Lauer for their support. I thank the office staff members of the department for their cooperation, and especially, Arnell Nelson for her kind help in navigating the administrative processes leading to the graduation.

Finally, I thank my parents for their support throughout my life, and for their unwavering faith in me.

Table of Contents

List of Tables

List of Figures

Abstract

Solid-state caloric effects, such as the magnetocaloric (MCE) and barocaloric (BCE) effects, may be utilized in future cooling technologies that are more efficient and environment-friendly. Large caloric effects often occur near phase transitions, especially near coupled first-order magnetostructural transitions (MST), and are initiated by external parameters, such as magnetic field or hydrostatic pressure. In this dissertation, the effects of pressure, temperature, and magnetic field on the phase transitions in three material systems are studied in order to elucidate how the respective caloric effects are affected.

In the first study, the realization of a coupled MST in a MnNiSi-based system through isostructural alloying is explored, which resulted in a giant conventional MCE. The MST shifts towards lower temperature with increasing applied hydrostatic pressure, whereas it shifts towards higher temperature with an increase in magnetic field. The strong pressure dependence along with a large volume change during the MST suggested the possibility of pressure-induced BCE in this material. In a subsequent study, we observed a giant hydrostatic pressure induced inverse BCE through pressure-dependent calorimetric measurements. The multiple caloric effects in the same material for the same phase transition qualify this material as a multicaloric material.

In second study, we investigated the hydrostatic pressure dependence of the metamagnetic transitions in $DyRu_2Si_2$, which shows multiple metamagnetic transitions at atmospheric pressure. With the application of moderate hydrostatic pressure, the metamagnetic transitions disappeared, but then reappeared with increasing pressure. We discuss the pressure-induced magnetostrictive behavior, the variation of the entropy changes with pressure, and a possible origin of the pressure-dependent behavior in light of the variation of the Ruderman-Kittel-Kasuya-Yosida (RKKY) exchange interactions.

For $x = 0.25$ in the $Ni_2Mn_{1-x}Cu_xGa$ Heusler alloy series, the structural and magnetic transitions coincide to create a coupled first-order MST. Since giant MCE was reported for this system, it is useful to understand the underlying physics driving the coupling of

transitions. Although first-order transitions cannot be investigated through the critical behavior analysis, the structural and magnetic transitions in Ni_2MnGa (parent alloy) and $Ni_2Mn_{0.85}Cu_{0.15}Ga$ are not coupled. In this case, investigating the critical behaviors of the two alloys near their second-order phase transitions will provide insight as to how the magnetism in these materials evolve with increasing copper doping. In this study, through the calculated critical exponent values, we identified the universality classes which best described the parent and Cu-doped (x = 0.15) alloys. The exponent values shed light into the range of the magnetic interactions, and the evolution of the interactions due to the non-magnetic Cu substitution scheme. This type of analysis can be performed in other material systems to get a picture of the systematic trends, through doping or other processes, such as applied pressure, that lead to first-order phase transitions.

Chapter 1
Introduction

1.1 Solid State Caloric Phenomena

In light of global energy and environmental concerns, it is becoming increasingly important to develop more efficient and environment-friendly options for commercial and household devices. In the United States, 42% of the total energy production is consumed by the residential and commercial sectors. A significant portion of this energy is used for various temperature control purposes, such as air-conditioning, refrigeration, freezing, etc. For instance, around 50% of the total residential energy consumption is spent on temperature control, whereas this number is 57% for the commercial establishments [1, 2]. Moreover, household refrigeration alone is responsible for 14% of the total energy consumption worldwide [3].

Conventional cooling technology is based on the absorption or emission of heat due to a change in pressure in the working material, usually a chlorofluorocarbon (CFC) gas, the type of which has been linked to the depletion of the ozone layer [4]. Moreover, the efficiency of this cooling technology is rather low, around 40%, even for the best commercial refrigerators. In this regard, solid-state cooling technology has the potential to replace conventional CFC gas-based cooling technology, and provide a more efficient and environmentally friendly solution.

Solid-state cooling is based on solid-state caloric effects, which are defined as the change of the temperature of a material due to an abrupt change of an external parameter. It has been shown that magnetic refrigeration using the magnetocaloric effect can reach 60% of the ideal Carnot efficiency [1], and has the potential to reduce the energy consumption by 20-30% relative to conventional CFC gas based cooling technology [5, 6]. In addition, solid-state cooling does not require environmentally harmful CFC gases, making it both an efficient and environmentally friendly alternative to conventional cooling technologies.

Apart from refrigeration technologies, solid-state caloric materials may be used in a

variety of other potential applications. For instance, the magnetocaloric effect can be utilized in energy harvesting [7], thermomagnetic generators [8], and even in drug delivery systems or in thermoseeds for cancer treatment [9, 10].

As stated earlier, the solid-state caloric effect in a material is induced by an abrupt change of an external parameter, such as magnetic field, electric field, pressure, stress, etc. The applied external stimulus modifies the material's order parameter, such as the magnetization (M), electric polarization (P), or strain (ε), etc. This creates a change in entropy, and a corresponding change in temperature. The caloric effects are quantified by the isothermal entropy change, ΔS_{iso}, and the adiabatic temperature change, ΔT_{ad}. For brevity, these quantities are often reported as ΔS and ΔT. All materials show caloric effects upon a change in an external applied parameter, however, this effect is often negligible [11]. Nevertheless, by employing various strategies, especially by tailoring the phase transitions of materials, the caloric effects can be modified to a level where practical application becomes feasible.

The isothermal application of an external parameter such as magnetic field usually decreases the material's entropy, whereas the adiabatic application increases the temperature. This behavior is observed for most materials, and this type of caloric effect is known as a "conventional caloric effect". However, the opposite scenario, i.e., increasing entropy and decreasing temperature, is not rare, and is known as the "inverse caloric effect" [11]. Table 1.1 summarizes these features for an increase in the external driving field.

Table 1.1: Changes in solid state caloric effect parameters due to conventional and inverse caloric effects.

Caloric Effect	Adiabatic Temperature Change	Isothermal Entropy Change	Isothermal Heat
Conventional	$\Delta T_{ad} > 0$	$\Delta S_{iso} < 0$	$Q < 0$
Inverse	$\Delta T_{ad} < 0$	$\Delta S_{iso} > 0$	$Q > 0$

Caloric effects can be divided into different categories based on the external driving field and the order parameter it modifies, as illustrated in Fig. 1.1. We now briefly define some of these effects [12].

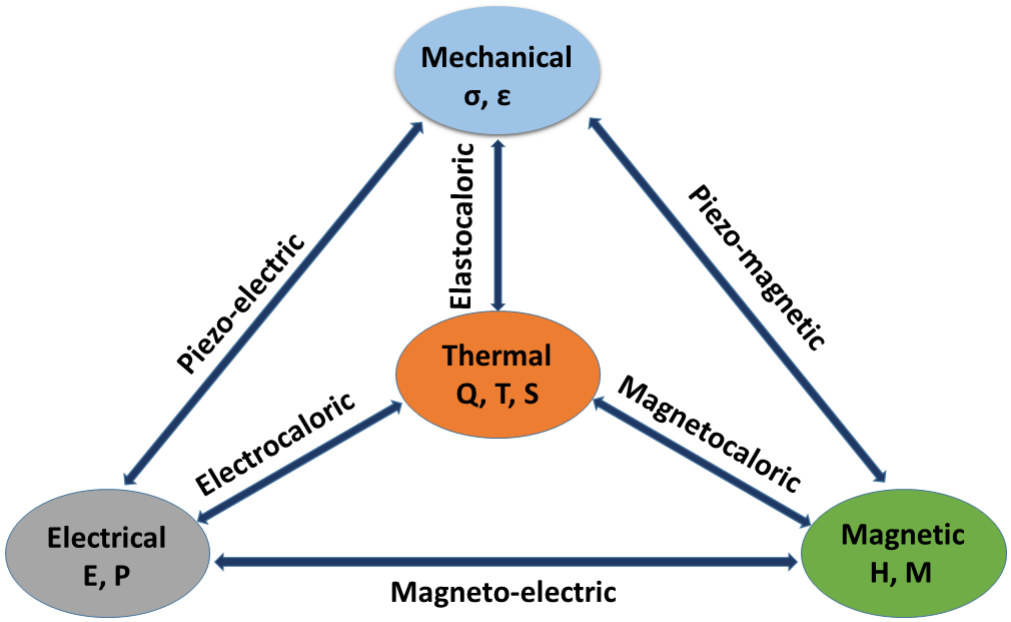

Figure 1.1: A schematic diagram of various solid state caloric effects. This diagram has been reproduced based on a diagram by Melvin M Vopson [3].

Magnetocaloric effect: In this case, a magnetic field acts as the external driving field, which modifies the magnetization (M). Changes in the applied magnetic field (ΔH) cause thermal changes. Here, the thermal changes are defined as the isothermal entropy change, ΔS, the adiabatic temperature change, ΔT_{ad}, and isothermal heat, Q.

Electrocaloric effect: An applied electric field (ΔE) modifies the electric polarization (P), which gives rise to thermal changes.

Mechanocaloric effect: An applied stress ($\Delta\sigma$) modifies the structural, magnetic, or polar degrees of freedom, and generates thermal changes. If the applied stress is uniaxial, the caloric effect is called an elastocaloric effect, whereas the applied hydrostatic pressure or isotropic stress induced caloric effects are known as barocaloric effects.

Multicaloric effect: If more than one type of caloric effect can be driven simultaneously or sequentially in the same sample, then the caloric effect can be described as a multicaloric effect. A "multicaloric material" can show multiple caloric effects, each driven by a different external parameter.

In the next few sections, further details about these caloric effects will be discussed. Since our research was mostly focused on magneto- and barocaloric effects, these two effects will now be discussed in more detail.

1.2 The Magnetocaloric Effect (MCE)

Since the early nineteenth century, the interplay between magnetism and heat had intrigued numerous scientists, for example Faraday and Joule [13, 14]. Later, Lord Kelvin laid out groundwork based on the general thermodynamics of the thermoelastic, thermomagnetic, and pyroelectric properties of matter [13, 15]. It was known at that time that the magnetism would be lost in a ferromagnetic material if sufficiently heated. Lord Kelvin proposed that an applied magnetic field can modify the temperature dependence of magnetization. He also predicted that the temperature of iron would decrease if it was slowly pulled away from a magnet near the temperature where iron losses its magnetization, and the temperature would increase if the iron is moved closer to a magnet. This effect is exactly what we now refer to as the magnetocaloric effect [13].

Magnetic cooling is based on the magnetocaloric effect (MCE) observed in magnetic materials. The MCE results from the alignment of magnetic moments due to the application of an external magnetic field, which reduces the magnetic randomness, thereby decreasing the magnetic component of the total entropy. This reduction in magnetic entropy is compensated by an increase in other components of the total entropy, such as electronic and lattice entropy, which results in a temperature increase of the material. This is the case for the conventional magnetocaloric effect, where the temperature of the material increases during magnetization and decreases during demagnetization. However, if the material shows an inverse magnetocaloric effect, then its temperature decreases during magnetization and increases during demagnetization. The inverse magnetocaloric effect is usually observed in materials that have antiferromagnetic interactions.

In most of the literature, Warburg is credited with the discovery of the magnetocaloric effect. However, Anders Smith [13, 16] pointed out that Warberg neither claimed to have

discovered MCE, nor was it possible to measure the temperature change due to the MCE from his experiment [17]. Warburg studied the magnetic hysteresis of iron during magnetization and demagnetization. He postulated that the area of the hysteresis loop in the magnetization (M) versus field (H) curve represents the work done on the magnetic material by the field. Since iron shows a reversible MCE due to a second-order phase transition, the total temperature change during magnetization and demagnetization would be zero.

There had been efforts to employ magnetothermal effects to other applications in the late 19^{th} century. For instance, the concept of the "thermomagnetic motor" was introduced by J. Stefan [13, 18, 19]. According to this concept, electricity could be generated by thermally cycling a ferromagnetic material through its Curie temperature. Both Edison and Tesla designed and patented devices known as "pyromagnetic generators" based on the effects described as pyromagnetic or thermomagnetic effects [13, 20–23].

In their 1918 report, Weiss and Piccard coined the term "magnetócalorique" in French scientific literature [12, 24]. Near the Curie temperature of nickel (627 K), they reported a temperature change of 0.7 K for a 1.5 T field change [16, 24]. They also pointed out that the effect is reversible, and that it is most prominent near the phase transition temperature. These are the characteristic features of the conventional magnetocaloric effect. The authors provided an explanation for this effect from a thermodynamics point of view, which was later developed further by Debye and Weiss et al. [16, 25, 26].

In the 1920s, Giauque and Debye proposed to use the magnetocaloric effect to reach very low temperatures—near absolute zero [25, 27]. In 1933, Giaucque and MacDougall reached a temperature of 250 mK by using the adiabatic demagnetization of a paramagnetic salt $Gd_2(SO_4)_3.8H_2O$, and breaking the 1 K barrier for the first time [28]. For this work, Giauque won the Nobel Prize in chemistry in 1949. This technique is still used in laboratories around the world to reach millikelvin temperatures [12]. However, the paramagnetic salts usually exhibit very small MCEs, and this is why adiabatic demagnetization of paramagnetic salts is primarily used to reach ultra-low temperatures rather than in near-room-temperature

applications.

The true beginning of near-room-temperature magnetic cooling can be traced back to the seminal paper by Brown [29]. Brown showed that, if a device operates continuously, much larger temperature spans than the maximum observed magnetocaloric effect (ΔT) can be achieved. In his refrigerator, 1 mm thick Gd plates separated by wire screens were used as the MCE material. An 80% water - 20% ethanol solution was used as the regenerator, while a 70 kOe alternating magnetic field was supplied by a superconducting magnet. According to the definition by J. A. Barclay [30], the function of a regenerator is to absorb heat from the working material in one stage of a cycle, and to return the heat to the working material on the next stage of the cycle. A maximum temperature span of 47 K was achieved with this system after 50 cycles with T_{hot} = 319 K (46 °C) and T_{cold} = 272 K (-1°C), where T_{hot} and T_{cold} are the temperatures of the hot and cold ends, respectively. This temperature span is three times larger than the maximum MCE (ΔT) of Gd metal between 272 K (ΔT_{ad} = 11 K) and 319 K (ΔT_{ad} = 13 K) [6].

The concept of active magnetic regenerators (AMR) was introduced by Steyert in 1978 following the works of Brown [6, 31]. In 1982, Barclay and Steyert proposed that a MCE material can be used simultaneously as an active magnetic component and as a regenerator. In this way, temperature changes greater than the adiabatic temperature change can be obtained in the magnetic refrigerant [32]. This concept of AMR has been used, in one form or another, in most of the later devices [16].

At this point, the significant impact of the collaboration between Ames Laboratory and the American Astronautics Corporation on realizing feasible, near-room-temperature magnetic cooling must be noted. In 1997, this collaboration led to a proof-of-principle magnetic refrigeration device, which demonstrated the feasibility of the magnetic refrigeration technology to be on par with conventional cooling technology near room temperature. This device was built on the active magnetic regeneration (AMR) principle, where commercial grade gadolinium was used as the AMR. Gadolinium rods were prepared at Ames Labo-

ratory from raw ingots, which were later converted into spheres using a plasma rotating electrode process (PREP) at the Starmet Powders Corporation. The device was operated continuously for 18 months with only minor maintenance. A superconducting magnet was used to apply up to a 50 kOe magnetic field, and it had a temperature span of 10 K (between 281 K and 291). It delivered a cooling power of around 600 W, and reached a maximum Carnot efficiency of 60% [6, 33, 34].

Another important breakthrough was delivered by the same group in 2001, when they replaced the superconducting magnet in the device with permanent magnets. Magnetic fields up to 15 kOe were applied using a permanent magnet array, which resulted in a temperature span of 5 K, and a cooling power of around 200 W [6, 35]. After this successful demonstration of the feasibility of magnetic cooling, numerous prototypes have been built around the world. Currently, there are many companies, such as BASF, Haier, General Electric, Camfridge Ltd., Cooltech Applications, etc., that are engaged in developing and delivering commercial magnetic cooling devices in the near future [6, 16].

Despite the limited successes of these prototypes, there are numerous challenges that still need to be overcome in order to realize the full-scale commercial operation of magnetic refrigeration technology. One of the principle challenges is to design or discover an ideal material to be used as the magnetic refrigerant (working material) in the device. One major breakthrough that prompted a paradigm shift in magnetocalorics research was the discovery of the giant MCE in $Gd_5Si_2Ge_2$ near room temperature by Pecharsky and Gschneidner in 1997 [36, 37]. Previously, magnetocaloric effects from materials only near second-order phase transitions were investigated and used in prototype devices. The second-order magnetic phase transitions limited the magnitude of the MCE, despite the absence of thermal hysteresis. However, in $Gd_5Si_2Ge_2$, a coupled magnetostructural transition (i.e., both second-order magnetic and first-order structural transitions) was responsible for the giant MCE and, consequently, a scurry of subsequent research efforts followed, leading to discoveries of large MCEs in materials showing first-order magnetostructural transitions.

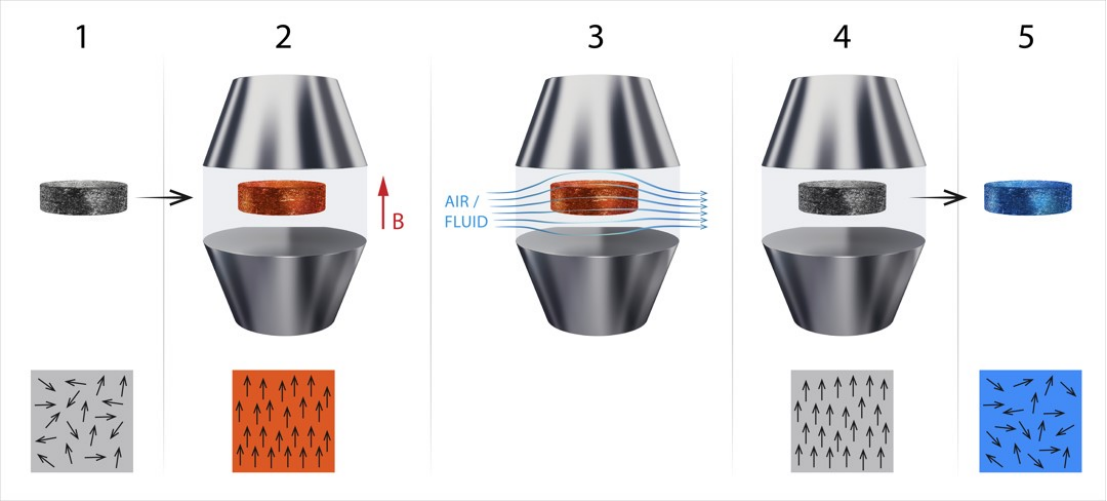

Figure 1.2: A simple magnetic cooling cycle using an MCE material.

This also prompted the search for methods to tailor materials to undergo first-order coupled magnetostructural transitions, and to investigate the underlying physics that drives them.

In order to illustrate the practical function of a cooling device that employs MCE materials, we now describe a simple magnetic cooling cycle (Fig. 1.2). In step 1, no applied magnetic field is present and the moments in the material are disordered. In step 2, a magnetic field is applied and the magnetic moments align with the field direction, become more ordered, and the magnetic entropy decreases. Consequently, the temperature of the material increases because of the compensating increase in lattice and electronic entropy. In step 3, while the field is still present, a heat conducting fluid conducts heat away from the MCE material. In step 4, the material returns to ambient temperature while the moments are still aligned. In step 5, the moments become disordered as the field is removed and the temperature of the material drops below ambient temperature, following the opposite mechanism described in steps 1 and 2, and can now be used to cool a load.

The importance of MCE materials in magnetic cooling technology cannot be over emphasized. Until now, few systems had been discovered that show a giant MCE near room temperature. These include, but are not limited to, MnAs based systems [38, 39], $La(Fe_{1-x}Si_x)_{13}$ [40], Ni_2MnGa based Heusler alloys [41, 42], MnCoGe alloys [43], MnNiSi

alloys [44, 45], and so on. A large MCE at low temperatures, especially around the boiling temperatures of various gases is also useful for gas liquification purposes [46–48]. Even though these materials exist, none have been successfully employed in a system that could be commercially realized. The reason for this lack of success is that a viable material must possess multiple properties in addition to a large isothermal entropy change (ΔS) and adiabatic temperature change (ΔT_{ad}).

In order to be an ideal functional device candidate, working materials should satisfy the following criteria [4, 49, 50]:

- The phase transition responsible for the MCE should be reversible with respect to temperature and magnetic field.
- There should be low magnetic hysteretic losses.
- The MCE must occur near the working temperature (i.e., near room temperature for room-temperature magnetic refrigeration).
- It should have large MCE potentials (ΔS_{iso} and ΔT_{ad}) for a reasonable applied magnetic field, preferably not exceeding 2 T so that permanent magnets can be used instead of superconducting magnets.
- The MCE material should have low specific heat and high thermal conductivity.
- The material should be non-toxic with low manufacturing costs, and with no potential harmful effects on the environment.
- The material should retain its structural form or shape even after temperature and field cycling, unless systems are developed to incorporate powders.

1.3 The Mechanocaloric Effect (mCE)

Although the magnetocaloric effect (MCE) is probably the most studied solid state caloric phenomenon so far, there are other mechanisms that can generate significant caloric

effects in solid materials. Research in materials that exhibit the mechanocaloric effect (mCE) is still in its early stages, however, the enormous potential of this technology has been acknowledged by researchers [51]. The mechanocaloric effect arises when an applied stress modifies the structural, magnetic, or polar degrees of freedom [51]. Moreover, it is possible for the applied stress to modify multiple degrees of freedom, which will generate a multicaloric effect. Depending on the nature of the applied stress, the mechanocaloric effect can be divided into two categories: elastocaloric and barocaloric. The elastocaloric effect (eCE) originates from a change in the applied uniaxial stress $\mid \Delta\sigma \mid$, whereas a change in the applied isotropic stress, that is, a change in the hydrostatic pressure (ΔP), is responsible for the barocaloric effect (BCE) [12].

In most cases, mechanocaloric effects are seen in materials that show structural phase transitions accompanied by a modification of the unit cell [51]. There are various mechanisms by which the crystal unit cell can be modified, namely, shear, dilation, and a combined effects of shear and dilation. Brief descriptions of materials that show mechanocaloric effects owing to stress-induced structural changes will now be discussed.

Materials with Purely Structural Transitions

Giant mechanocaloric effects are often seen in non-magnetic shape memory alloys (SMA), where the phase transition is purely structural [51]. These alloys exhibit shape memory effects, which are defined as the ability of a material to repeatedly recover from large plastic deformation[52]. The structural phase transitions in these types of alloys are known as martensitic transformations, through which the crystal lattice is modulated via a shear mechanism. Martensitic transformations are classified as first-order phase transitions, which usually involve large volume effects, latent heat, and thermal hysteresis [53]. These transitions occur between a high-temperature, high-symmetry crystal phase, known as the austenite phase, and a low-temperature, low-symmetry phase, known as the martensite phase [51, 53]. In general, martensitic transitions are very sensitive to uniaxial pressure, due to the large shear-induced crystal distortions that usually accompany these transitions.

On the other hand, these materials show little sensitivity to applied hydrostatic pressure or isotropic stress. Moreover, due to the first-order nature of the transitions, large latent heats are generated, which in turn give rise to large elastocaloric effects.

Some of the materials that show large elastocaloric effects include Cu-Zn-Al alloys [54–56], Ni-Ti alloys [57–59], Cu doped Ni-Ti alloys [60, 61], and so on [51]. In a Cu-Zn-Al single crystal, an entropy change of $\Delta S \simeq 21$ J/kg K was observed for ≈ 0.1 GPa of applied uniaxial stress [51, 54, 55]. An adiabatic temperature change of $\Delta T_{ad} \simeq 6$ K was also observed in a single crystal with slightly different stoichiometry through an infrared thermal imaging technique [51, 56]. An inherent advantageous property of non-magnetic shape memory alloys is their ductility, and the ability to retain their shapes fairly well over multiple stress and/or temperature cycles.

Materials with Magnetostructural Transitions

Mechanocaloric effects are also observed in materials that show first-order magnetostructural transitions, where magnetic and structural degrees of freedom are coupled, and external fields, such as magnetic field and stress, can alter the magnetization and/or strain. In this case, the structural transition can occur through two mechanisms: dilation, where the crystal lattice uniformly expands or contracts with no change in crystal symmetry, or a combination of dilation and shear in which the lattice completely transforms from one crystal symmetry to another [51]. In most of the giant MCE materials, coupled first-order magnetostructural transitions are responsible for the giant caloric effects.

Both elastocaloric and barocaloric effects can be expected in materials where the lattice undergoes uniform expansion or contraction due to applied stress (uniaxial or hydrostatic pressure). One early example is Fe-Rh alloys, which show both of these effects [51, 62–64] along with the magnetocaloric effect [65]. Fe-Rh alloys have a cubic CsCl-type crystal structure and, when the stoichiometry is close to FeRh, the phase transition occurs between a ferromagnetic (high-temperature) phase to an antiferromagnetic (low-temperature) phase. The crystal symmetry does not change during the phase transition, but its volume changes

(by around 1%) as the high temperature ferromagnetic (FM) phase has a larger volume than the low-temperature antiferromagnetic (AFM) phase. This change in the structure is due to dilation [51, 66]. In $Fe_{49}Rh_{51}$, an entropy change of $\Delta S \simeq 12$ J/kg K and an adiabatic temperature change of $\Delta T \simeq 10$ K were observed for an applied hydrostatic pressure of around 0.25 GPa, due to the barocaloric effect [51, 63, 64]. On the other hand, an adiabatic temperature change of $\Delta T \simeq$ -5 K was observed for an applied tensile stress of $\sigma \simeq 0.5$ GPa [51, 62]. It should be noted that the elastocaloric effect is inverse for this material, i.e., the entropy change is positive, whereas the barocaloric effect is conventional [51].

Another class of materials that exhibits mechanocaloric effects is the La-Fe-Si family of compounds, which has a cubic $NaZn_{13}$-type crystal structure. The first-order magnetostructural transition is from a paramagnetic phase to a ferromagnetic phase during cooling [51, 67]. In the Co substituted sample, $LaFe_{11.33}Co_{0.47}Si_{1.2}$, an entropy change of $\Delta S \simeq 9$ J/kg K for an applied hydrostatic pressure of around 0.2 GPa was observed due to an inverse barocaloric effect [68]. In this case, an adiabatic temperature change of $\Delta T \simeq$ 2 K was measured through direct measurements. Giant barocaloric effects have also been reported for Mn_3GaN [51, 69].

Magnetostructural Transitions with Changes in Crystal Symmetry

Materials exist that undergo a first-order magnetostructural transition involving a structural transition between two completely different crystallographic symmetries, e.g., from cubic to tetragonal, from hexagonal to orthorhombic, etc. In such a case, a combination of shear and dilation mechanisms is involved in the structural transition, which often exhibits a high sensitivity to applied hydrostatic pressure [51]. Moreover, these transitions usually give rise to giant MCEs. The total entropy change for materials showing these types of transitions is a sum of the magnetic and structural entropy changes. It had been observed that materials that exhibit large volume changes during the phase transition, along with strong hydrostatic pressure sensitivity, are the most likely candidates to show

large barocaloric effects [70].

The well known giant MCE material $Gd_5(Si_xGe_{1-x})_4$ also shows large barocaloric effects [71]. In this case, there is a magnetostructural transition from a paramagnetic monoclinic structure to a ferromagnetic orthorhombic phase [50, 51]. This transition is responsible for the barocaloric effect, which is accompanied by an entropy change, $\Delta S \simeq 11$ J/kg K for an applied hydrostatic pressure of 0.2 GPa [51, 71]. A further discussion of this material will be provided in later sections.

Another class of materials that shows magnetostructural transitions is the MnTX (T = Ni, Co, and X = Si, Ge) system [43, 51]. These materials also undergo coupled magnetostructural transitions. The transitions usually have to be tuned through various strategies such as substitution, stoichiometry variation, etc., that sometimes exhibit giant MCEs and BCEs. We have investigated giant caloric effects in one such system, and the details will be discussed in chapter 4.

Based on the abovementioned discussion, it can be summarized that hydrostatic pressure has a weak effect in materials where the structural transition occurs through a purely shear mechanism. This factor, along with the small volume change, render large barocaloric effects unlikely in these materials. However, uniaxial stress usually has a stronger affect on these materials, resulting in possible large elastocaloric effects. On the other hand, when the structural transition is a combination of shear and dilation mechanisms, hydrostatic pressure is likely to strongly affect the transition, leading to potential barocaloric effects. However, a large volume change must also occur in this case [51, 70].

The reported direct measurements of the temperature change due to elastocaloric effects are close to the theoretically estimated maximum values. On the other hand, direct measurements of the temperature change due to barocaloric effects yield far lower values than the estimated values. The lack of proper adiabatic measurement conditions are likely responsible for this trend [51]. To apply hydrostatic pressure, it is necessary to have a pressure conducting fluid, which makes it challenging to achieve adiabatic conditions. This

feature will be discussed in chapter 4.5, where a description of the experimental setup we constructed to measure the temperature change due to the barocaloric effect will be provided.

Currently, no prototype cooling device based solely on the solid-state barocaloric effect exists. There are, however, prototype devices based on the elastocaloric effect. These devices utilize non-magnetic shape memory alloys such as Ni-Ti as the working materials [51, 72, 73]. Although the research in this field is still in its early stage, it shows promise for future solid-state cooling technologies.

1.4 The Electrocaloric Effect (ECE)

The electrocaloric effect arises when an applied electric field modifies the electric polarization in a dielectric material. This change in polarization causes an entropy change, and consequently, a temperature change [74]. Similar to other caloric materials, electorcaloric materials have the potential to be used as the working material in a solid-state cooling device. One particularly promising aspect of ECEs is that large ECE parameters have been observed in thin-films, which can be used to create chip-scale micro-cooling devices [74, 75]. Furthermore, the ECE may have potential applications in sensors, medical applications, and electronic devices [74, 75].

Similar to the magnetocaloric effect (MCE), the ECE is characterized by the isothermal entropy change (ΔS) and the adiabatic temperature change (ΔT). As the MCE is maximum near a magnetic phase transition, a large ECE is usually observed near the ferroelectric (F) to paraelectric (P) transition. Similiar to the MCE, the ECE is usually the largest for first-order phase transitions, and moderate for second-order transitions [75–77].

A typical cooling cycle using ECE materials is identical to the MCE cooling cycle. In this case, an electric field is applied in the first stage, which aligns the electric dipoles, and reduces the entropy contribution from the dipoles to the total entropy. In order to compensate this reduction in dipole entropy, contributions from other sources (e.g., lattice, vibrational, etc.) increase, and the temperature of the material increases. In the second

stage, a heat conducting fluid conducts heat away from the material. This reduces the temperature of the material, while the dipoles remain aligned because of the electric field. In the third stage, the electric field is removed, the dipoles become disordered, and the temperature of the material drops below the ambient temperature following the opposite mechanism described in the first stage. At this point, the ECE material can be used to cool a load as its temperature is lower than that of the environment [75].

In 1930, Kobeko and Kurtschatov first studied the ECE in Rochelle salt [74, 78], but they did not report any specific values. A few decades later, in 1963, an adiabatic temperature change of $\Delta T = 0.0036$°C was reported for Rochelle salt by Wiseman and Keubler for an applied electric field of 1.4 kV cm^{-1} at 22°C [79]. ECEs were further investigated in various ceramics and single crystals, such as KH_2PO_4 crystals [80], $SrTiO_3$ ceramics [81], $Pb(Sc_{0.5}Ta_{0.5})O_3$ ceramics [82], and so on. However, the ECEs in these materials are not large, and a large electric field cannot be applied to these materials because of their low breakdown fields [74]. Since the breakdown fields are larger in thin films and polymers, the ECE has been widely investigated in these materials. A significant breakthrough took place when Mischenko et al. [83] reported a giant ECE in thin films of $PbZr_{0.95}Ti_{0.05}O_3$ in 2006. They observed an adiabatic temperature change of $\Delta T = 12$°C at 226°C for an applied electric field of 48 MV/m [74, 75, 83].

Since the discovery of giant ECEs, there has been vigorous research activity in this field. A few prototypes based on ECE materials have been built [82, 84, 85]. However, the ECEs in these materials are relatively low, which reduce the possibility of full-scale practical applications. Nevertheless, this field is relatively unexplored, and further investigations may open up new possibilities.

1.5 The Multicaloric Effect

It is possible for two or more solid state caloric effects to occur simultaneously in the same material. According to the definition by Moya et al., [12], if more than one type of caloric effect can be driven simultaneously or sequentially in the same sample, then the

combined caloric effects can be described as a multicaloric effect. In this respect, the multiferroic materials are the most promising class of materials to show multicaloric effects, since these materials can simultaneously exhibit multiple ferroic ordered phases, such as electric, magnetic, or elastic. The concept of multicaloric effects in multiferroic materials was first introduced theoretically in 2012 by Melvin M. Vopson [86]. He pointed out that the multicaloric effect is strongly dependent on the cross-coupling between the various ferroic ordered states in a multiferroic material [3]. For instance, in a multiferroic material, either the electric field (E) or the magnetic field (H) can modify the polarization and magnetization, which can lead to the multicaloric effect. The phenomenon has the potential to drastically enhance the caloric effects, and advance solid-state cooling technology. Furthermore, it can have promising application in sensor technology [87, 88], memory technology [89–91], transformers [92], and energy harvesting devices [93].

A typical refrigeration cycle using multicaloric effects would be similar to the previously mentioned cycles. For instance, if the applied magnetic field (H), or the electric field (E), or both, can align the magnetic and electric dipole moments, then the material's temperature will increase. The heat can then be conducted away through a heat-conducting fluid. This will reduce the material's temperature to the ambient temperature. Now, if the magnetic field (H) or the electric field (E) is removed, the magnetic and electric dipole moments will be disordered, and the temperature of the material will be less than the ambient temperature. At this point, this material can be used to cool a load [3, 86].

It is known that an applied hydrostatic pressure can modify the magnetic entropy of a solid, which is called the barocaloric effect [70, 94]. N. A. de Oliveira [70] theoretically studied the effect of observing the magneto- and barocaloric effects in the same material undergoing a first-order phase transition. He pointed out that the application of a magnetic field can also change the barocaloric potentials, i.e., the isothermal entropy change (ΔS_{BCE}) and the adiabatic temperature change (ΔT_{BCE}). Although the first-order transitions usually generate large entropy changes, these changes occur over a very narrow temperature

span. In other words, the entropy change (ΔS) versus temperature (T) curves would have a very sharp peak for materials showing first-order transitions. N. A. de Oliveira showed that, by simultaneously varying the pressure and magnetic field, a table-like shape in the ΔS vs. T curve could be achieved. This could, in effect, increase the working temperature range of the magnetocaloric materials. This feature, however, relies on the fact that the hydrostatic pressure can shift the first-order transition temperature, and the entropy change does not reduce significantly throughout the applied pressure range [70]. We observed similar magneto- and barocaloric effects in a single material for the same first-order transition. A detailed discussion on this topic will be provided in chapter 4.4.

Chapter 2
Theoretical Aspects

2.1 Thermodynamics of the Magnetocaloric Effect

In this section, a brief description of the origin of the magnetocaloric effect will be provided from a theoretical point of view. The relationship between different thermodynamic variables, such as magnetization, magnetic field, pressure, temperature, and entropy will be established. Although the magnetocaloric effect is intrinsic to all magnetic materials, pronounced effects are seen only in materials where the magnetic part of the entropy is significantly changed due to the application of magnetic field (or pressure, electric field, etc.).

The magnetocaloric effect is quantified by the isothermal entropy change (ΔS_{iso}) and the adiabatic temperature change (ΔT_{ad}). These two quantities are often referred to as magnetocaloric potentials. The total entropy of a magnetic material consists of contributions from the crystalline lattice (S_{lat}), conduction electrons (S_{el}), atomic magnetic moments (S_{mag}), and atomic nucleus (S_{nuc}). We can neglect the contribution from the nucleus as it is significant only at very low temperatures. Therefore, the total entropy of a solid can be written as [95, 96]

$$S(T, B, P) = S_{el}(T, B, P) + S_{mag}(T, B, P) + S_{lat}(T, B, P). \tag{2.1}$$

For simplicity, it can be assumed that the electronic and lattice entropies do not change with applied magnetic field and pressure. Although this is not true in certain situations, such as first-order coupled magnetostructural transitions, this assumption is valid for materials undergoing second-order phase transitions. As mentioned in the previous chapter, an external magnetic field aligns the magnetic moments, and hence reduces the magnetic component of the total entropy. Consequently, other components of the total entropy, such as lattice entropy and electronic entropy, increase to compensate the reduction in the

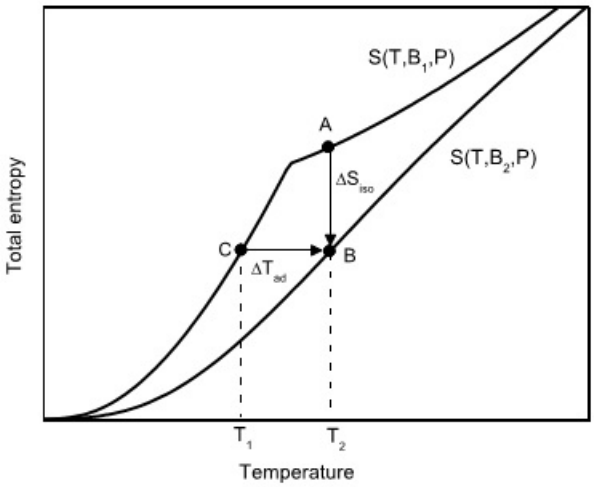

Figure 2.1: Entropy versus temperature for two values of applied magnetic field, B_1 and B_2, where $B_2 > B_1$ [96].

magnetic entropy, causing a temperature change of the material [41].

In Fig. 2.1, a schematic diagram of the total entropy (S) versus temperature (T) for a typical ferromagnet is plotted for two external magnetic field strengths, B_1 and B_2, where $B_2 > B_1$. From this figure, magnetocaloric potentials ΔS_{iso} and ΔT_{ad} can be easily described. ΔS_{iso} is the difference between the entropies in the final and initial states of any isothermal process, such as the path AB in Fig. 2.1. The isothermal entropy change, ΔS_{iso} for a magnetic field variation from B_1 to B_2 is given by

$$\Delta S_{iso}(T, B_2 - B_1, P) = S(T, B_2, P) - S(T, B_1, P). \tag{2.2}$$

The adiabatic temperature change, ΔT_{ad}, is calculated by taking the difference between the temperature of the initial and final states of an adiabatic process. When a magnetic field is applied adiabatically, as represented by the path CB in Fig. 2.1, $\Delta T_{ad} > 0$, and the temperature of the material increases. On the other hand, $\Delta T_{ad} < 0$ for an adiabatic removal of the magnetic field, as in path BC, for which the material's temperature decreases. The adiabatic temperature change (ΔT_{ad}) upon a magnetic field variation from B_1 to B_2

is given by

$$\Delta T_{ad}(T, B_2 - B_1, P) = T_2(B_2) - T_1(B_1), \tag{2.3}$$

under adiabatic conditions, $S(T_2, B_2, P) = S(T_1, B_1, P)$.

In order to determine the MCE potentials from real experiments, it is necessary to express these potentials in terms of experimentally measurable quantities. MCE potentials can be analytically expressed in terms of total entropy and heat capacity. These potentials can also be determined indirectly from magnetization data. Let us start by considering that the entropy is a function of temperature, pressure, and magnetic field,

$$S = S(T, B, P). \tag{2.4}$$

In this case, we can write the total differential as [97]

$$dS(T, B, P) = \left[\frac{\partial S(T, B, P)}{\partial T}\right]_{B,P} dT + \left[\frac{\partial S(T, B, P)}{\partial B}\right]_{T,P} dB + \left[\frac{\partial S(T, B, P)}{\partial P}\right]_{T,B} dP. \tag{2.5}$$

For an isobaric process, $dP = 0$, and therefore eq. (2.5) becomes

$$dS(T, B) = \left[\frac{\partial S(T, B)}{\partial T}\right]_{B} dT + \left[\frac{\partial S(T, B)}{\partial B}\right]_{T} dB. \tag{2.6}$$

For an istohermal process (i.e., $dT = 0$), an expression for the isothermal entropy change, ΔS_{iso}, can be obtained from eq. (2.6) for a field varying from B_1 to B_2:

$$\Delta S_{iso} = \int_{B_1}^{B_2} \left[\frac{\partial S(T, B)}{\partial B}\right]_{T} dB. \tag{2.7}$$

For an adiabatic process, $S(T_2, B_2) = S(T_1, B_1)$, and therefore $dS(T, B) = 0$. Hence, the left side of eq. (2.6) would be zero, and we can express the adiabatic temperature

change, ΔT_{ad}, as the magnetic field changes from B_1 to B_2 as :

$$\Delta T_{ad} = -\int_{B_1}^{B_2} \frac{1}{\left[\frac{\partial S(T,B)}{\partial T}\right]_B} \left[\frac{\partial S(T,B)}{\partial B}\right]_T dB. \tag{2.8}$$

By using the expression for the heat capacity, $C_B(T,B) = T\left[\partial S(T,B)/\partial T\right]_B$, in the previous equation, we find

$$\Delta T_{ad} = -\int_{B_1}^{B_2} \frac{T}{C_B(T,B)} \left[\frac{\partial S(T,B)}{\partial B}\right]_T dB. \tag{2.9}$$

The previous two expressions for ΔS_{iso} and ΔT_{ad} are given in terms of entropy, which is not convenient from a practical measurement point of view, as entropy is not an experimentally measurable quantity. The expressions for these two MCE potentials can be given in terms of the magnetization, which can be easily measured in laboratories. For this purpose, let us consider the Gibbs free energy as a function of temperature and magnetic field, $G = G(T,B)$. As before, we can write the total differential as

$$dG(T,B) = \left[\frac{\partial G(T,B)}{\partial T}\right]_B dT + \left[\frac{\partial G(T,B)}{\partial B}\right]_T dB. \tag{2.10}$$

Using the thermodynamic relations:

$$\begin{aligned} S &= -\left[\frac{\partial G(T,B)}{\partial T}\right]_B \\ M &= -\left[\frac{\partial G(T,B)}{\partial B}\right]_T, \end{aligned} \tag{2.11}$$

eq. (2.10) can be written as

$$dG(T,B) = -S(T,B)dT - M(T,B)dB. \tag{2.12}$$

By using the fact that $G(T,B)$ is an exact differential, we arrive at the following Maxwell

relation

$$\left[\frac{\partial S(T,B)}{\partial B}\right]_T = \left[\frac{\partial M(T,B)}{\partial T}\right]_B. \tag{2.13}$$

Applying this relationship in eq. (2.7), we get the isothermal entropy change, ΔS_{iso}, in terms of the magnetization (M) as

$$\Delta S_{iso} = \int_{B_1}^{B_2} \left[\frac{\partial M(T,B)}{\partial T}\right]_T dB. \tag{2.14}$$

Near the magnetic ordering temperature, the partial derivative $\partial M/\partial T$ is maximum, and hence the isothermal entropy change is expected to be maximum near the ordering temperature. For practical purposes, we can write the previous equation in the following way, which can be used to calculate ΔS_{iso} from magnetization (M) versus magnetic field (H) data [41, 50],

$$\Delta S_{iso}(T,B) = \frac{1}{\delta T}\int_{B_1}^{B_2} \left[M(T+\delta T,B) - M(T,B)\right] dB. \tag{2.15}$$

Using the Maxwell relation (eq. (2.13)) in eq. (2.9), the adiabatic temperature change is given by

$$\Delta T_{ad} = -\int_{B_1}^{B_2} \frac{T}{C_B(T,B)}\left[\frac{\partial M(T,B)}{\partial T}\right]_B dB. \tag{2.16}$$

Experimentally, bulk magnetization data as a function of temperature and magnetic field are relatively easy to obtain. This is why eq. (2.15) is frequently used to evaluate the isothermal magnetic entropy change in MCE materials [50]. However, it is challenging to obtain magnetic field and temperature dependent heat capacity data with the desired resolution to carry out reliable numerical integration. Consequently, eq. (2.16) is rarely used to evaluate the adiabatic temperature change. The process of estimating ΔT_{ad} from heat capacity measurements will be described in detail in Chapter 5.

2.2 Thermodynamics of the Barocaloric Effect

The application of external pressure can also change the entropy in materials. This is known as the barocaloric effect. Similar to the magnetocaloric effect, it is characterized by the istothermal entropy change (ΔS_{iso}) and adiabatic temperature change (ΔT_{ad}) upon a variation of applied pressure. In the case of magnetic materials, applied pressure can affect the magnetic order. According to the situation depicted in Fig. 2.2, applied pressure increases the magnetic order, and thereby reduces the magnetic entropy. Consequently, other components of the total entropy must compensate, resulting in a temperature change of the material.

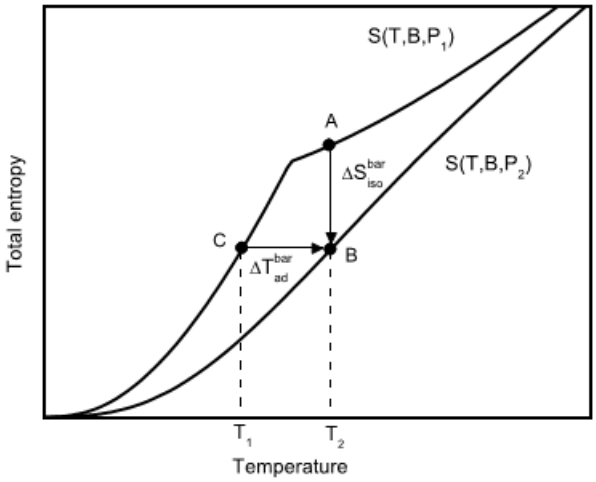

Figure 2.2: Entropy versus temperature for two values of applied pressure, P_1 and P_2, where $P_2 > P_1$ [96].

The isothermal entropy change, ΔS_{iso}, according to Fig. 2.2 for a variation of pressure from P_1 to P_2 is given by

$$\Delta S_{iso}(T, B, P_2 - P_1) = S(T, B, P_2) - S(T, B, P_1). \tag{2.17}$$

The adiabatic temperature change, ΔT_{ad}, for a variation of pressure from P_1 to P_2 is given by

$$\Delta T_{ad}(T, B, P_2 - P_1) = T_2(P_2) - T_1(P_1), \tag{2.18}$$

under adiabatic conditions, $S(T_2, B, P_2) = S(T_1, B, P_1)$.

From the total differential dS given in eq. (2.5), the mathematical expressions for the barocaloric effect can be derived. For an isothermal process at constant magnetic field, we write [97]

$$\Delta S_{iso}^{bar}(T, B, \Delta P) = \int_{P_1}^{P_2} \left[\frac{\partial S(T, B, P)}{\partial P}\right]_{T,B} dP. \tag{2.19}$$

Similarly, the adiabatic temperature change at constant magnetic field is given by

$$\Delta T_{ad}^{bar}(T, B, \Delta P) = -\int_{P_1}^{P_2} \frac{T}{C_{B,P}} \left[\frac{\partial S(T, B, P)}{\partial P}\right]_{T,B} dP. \tag{2.20}$$

Here, $\Delta P = P_2 - P_1$, and $C_{B,P} = T\left[\partial S(T, B, P)/\partial T\right]_{B,P}$ is the heat capacity at constant magnetic field and pressure.

2.3 Thermodynamics of the Multicaloric Effect

According to the theoretical treatment by Melvin M. Vopson [3], for the generalized forces/fields x_i [x_i = magnetic field (H), electric field (E), stress (σ), etc.] and independent variables X_i [x_i = magnetization (M), polarization (P), strain ε), etc.], the generalized Maxwell relations can be given as

$$\left(\frac{\partial S}{\partial x_i}\right)_{T, x_{j\neq i}} = \left(\frac{\partial X_i}{\partial T}\right)_{x_j}, \tag{2.21}$$

$$\left(\frac{\partial X_j}{\partial x_i}\right)_{T, x_{j\neq i}} = \left(\frac{\partial X_i}{\partial x_j}\right)_{T, x_i}. \tag{2.22}$$

Here, S is the entropy and T is the temperature. In light of eq. 2.22, Vopson argued that a cross coupling between the forces/fields (x_i) and the independent variables (X_j) can occur. The forces are conjugated to the independent variables thermodynamically. A coupling

coefficient can be defined assuming a linear coupling between these quantities:

$$\left(\frac{\partial X_j}{\partial x_i}\right)_{T,x_{j\neq i}} = \left(\frac{\partial X_i}{\partial x_j}\right)_{T,x_{i\neq j}} = \alpha_{ij} = \alpha_{ji} = \alpha. \tag{2.23}$$

This coupling feature points toward the fact that a particular generalized independent variable [e.g., magnetization (M), polarization (P), volume (V), strain (ε), etc.] can be modified due to a change in more than one force/field [e.g., magnetic field (H), electric field (E), stress (σ), etc.]. For instance, in a multiferroic material, an applied magnetic field (H) can modify the magnetization (M) as well as the electric polarization (P). In the opposite scenario, an applied electric field (E) can modify the electric polarization (P) as well as the magnetization (M). This cross coupling gives rise to the multicaloric effect, for which the adiabatic temperature change can be given by [3]

$$\Delta T = -\frac{T}{C}\sum_{i;i\neq j}\int_{x_j}\left[\left(\frac{\partial X_i}{\partial T}\right)_{x_j}\frac{\alpha_{ij}}{\chi_i} + \left(\frac{\partial X_j}{\partial T}\right)_{x_i}\right]dx_j. \tag{2.24}$$

Here, $\chi_i = \frac{\partial X_i}{\partial x_i}$ is the generalized susceptibility and C is the heat capacity. In eq. 2.24, the first term inside the brackets represents the multicaloric contribution to the total temperature change due to the cross coupling, and the second term corresponds to the standard caloric effect. Moreover, it is clear that the adiabatic application of only one field can modify more than one independent variable, and enhance the total temperature change. However, in order to enhance the total temperature change, it is necessary that the standard and multicaloric terms have the same signs. It is also possible for them to have opposite signs and, in that case, the total temperature change will be reduced or even canceled [3, 86].

For instance, if we consider a multiferroic material with magnetoelectric coupling, the total electrically induced adiabatic temperature change due to a change in the applied

electric field from E_i to E_f can be given by [86]

$$\Delta T_E = -T \int_{E_i}^{E_f} \frac{1}{C_{E,H}} \left[\frac{\alpha_e}{\mu_0 \chi^m} \left(\frac{\partial M}{\partial T} \right)_{H,E} + \left(\frac{\partial P}{\partial T} \right)_{H,E} \right] dE. \tag{2.25}$$

For a change in the applied magnetic field from H_i to H_f, the total magnetic field induced temperature change would be [86]

$$\Delta T_H = -T \int_{H_i}^{H_f} \frac{1}{C_{E,H}} \left[\left(\frac{\partial M}{\partial T} \right)_{H,E} + \frac{\alpha_m}{\varepsilon_0 \chi^e} \left(\frac{\partial P}{\partial T} \right)_{H,E} \right] dH. \tag{2.26}$$

Here, μ_0, ε_0, χ^m, and χ^e are the magnetic permeability of vacuum, dielectric permittivity of vacuum, magnetic susceptibility, and electric susceptibility, respectively. α_e and α_m are the electrically and magnetically induced coupling constants, respectively. In this scenario, an electric field (E) can modify the polarization (P) as well as the magnetization (M), whereas an applied mangetic field (H) can modify the magnetization (M) as well as the polarization (P). Due to the magnetoelectric coupling, the standard and multicaloric effects can aggregate if they have the same signs, and enhance the total adiabatic temperature change. It can be noted that, in eqs. 2.25 and 2.26, if there is no coupling (i.e., $\alpha_e = \alpha_m = 0$), then the equations reduce to the well known conventional electrocaloric and magnetocaloric effects [3, 86].

2.4 Phase Transitions and the Magnetocaloric Effect

Large entropy changes (ΔS) and adiabatic temperature changes (ΔT_{ad}) are the most desired characteristics in a magnetocaloric material. Over the years, extensive experimental and theoretical investigations have shown that the magnetic entropy change strongly depends on the nature of the phase transition. Magnetic phase transitions can be divided into two classes: first-order phase transitions (FOPT) and second-order phase transitions (SOPT). For a second-order phase transition, the second derivative of the thermodynamic potential with respect to a generalized force (temperature, pressure, or magnetic field) undergoes a discontinuous change, whereas the first-derivatives are continuous functions [98]. For example, the magnetization and entropy in terms of the Gibbs free energy (G) are given by the following relations:

$$S(T,B) = -\left[\frac{\partial G(T,B)}{\partial T}\right]_B \tag{2.27}$$

$$M(T,B) = -\left[\frac{\partial G(T,B)}{\partial B}\right]_T. \tag{2.28}$$

Here, the magnetization (M) and entropy (S) are first-order derivatives of the thermodynamic potential (Gibbs free energy, G). These derivatives would be continuous for a second-order transition. In other words, there would be no jump or discontinuity in the magnetization or entropy for a second-order phase transition. This also means that no latent heat ($\Delta Q = T\Delta S$) is involved during a second-order phase transition.

The heat capacity in terms of the Gibbs free energy is given by the following relation:

$$C_B(T,B) = -T\left[\frac{\partial^2 G}{\partial T^2}\right]_B. \tag{2.29}$$

Here the heat capacity (C) is a second-order derivative of the thermodynamic potential, which is not continuous for a second-order transition. This is why, in the vicinity of a second-order transition, the heat capacity (C) vs. temperature (T) plot will show a

jump/discontinuity.

The magnetocaloric effect due to a second-order phase transition is usually small, and spread over a broad temperature range [99]. The effects due to hysteresis, anisotropy, coercive fields, and remanence are considered negligible, and do not affect the MCE [100]. These aspects of the second-order phase transition are advantageous for a practical application in devices. However, the discovery of giant MCE in the $Gd_5Si_xGe_{4-x}$ system due to coupled first-order magnetostructural transitions shifted the focus of the magnetocaloric research towards materials that undergo first-order phase transitions [36, 37].

Through a first-order phase transition, the first-order derivative of the thermodynamic potential with respect to the generalized force (temperature, pressure, or magnetic field) undergoes a discontinuous change. Therefore, the entropy and magnetization as given by eqs. (2.27) and (2.28) would be discontinuous, and show a jump at the point of transition [98]. Because of this discontinuous change, a latent heat ($\Delta Q = T\Delta S$) is generated during a FOPT [98]. It is also characterized by a hysteresis (thermal or magnetic), as one of the generalized forces, such as temperature, magnetic field, or pressure is varied across the phase transition region. From an experimental point of view, a FOPT can be confirmed by determining the latent heat. However, in many real systems, the latent heat is too small to detect experimentally [101]. In magnetic systems, the first-order nature of the phase transition is often recognized by a temperature hysteresis in the temperature dependent magnetization (M(T)) data. However, hysteresis alone is not a definitive proof of a first-order phase transition [16, 102]. In some cases, identifying the order of phase transition is quite challenging, and detailed analysis is required for such task. For instance, a widely used procedure is to apply the Banerjee criterion [103] to identify FOPTs using the Arrott plot. Details of this method will be discussed in chapters 5 and 6.

First-order phase transitions can be of different types. For instance, a metamagentic transition is defined as a transition between two different magnetic structures. It can be antiferromagnetic to ferromagnetic, ferromagnetic to ferromagnetic, ferromagnetic to

ferrimagnetic, and so on [16]. In a coupled magnetostructural transition (MST), magnetic ordering as well as the lattice structure can change simultaneously with a variation in temperature, magnetic field, or pressure. In these magnetic materials, external magnetic field, temperature, or pressure can modify the lattice (non-magnetic) degrees of freedom. This is due to a coupling between the spin and elastic degrees of freedom [101], which is responsible for the coupled MST. This type of transition produces giant MCEs observed in material systems such as $Gd_5(Si, Ge)_4$ [36], Ni_2MnGa Heusler alloy compounds [41, 42], MnCoGe-based materials [43], MnAs-based materials [38, 39], etc.

According to Pecharsky et al. [104, 105], in materials showing coupled MSTs, the total field-induced MCE is a sum of the magnetic (ΔS_M) and structural (ΔS_{st}) entropy changes,

$$\Delta S_T = \Delta S_M + \Delta S_{st}. \tag{2.30}$$

Here, ΔS_M is the magnetic entropy change at a conventional second-order magnetic phase transition, whereas ΔS_{st} is the entropy difference between two different crystallographic polymorphs. As an example, consider the case of $Gd_5Si_2Ge_2$, where a coupled MST gives rise to a giant MCE. In this material, the Gd and (Si,Ge) atoms are arranged in distinct layers and, during the coupled first-order MST, the layers shift with respect to each other. This shifting can be up to $\sim 0.5\,\text{Å}$, which creates a phase-volume change of around 0.94% [104–106]. This phase-volume change generates a significant structural entropy change, which is comparable to the magnetic entropy change. These two forms of entropy changes aggregate in the case of $Gd_5Si_2Ge_2$ to produce a giant MCE.

Experimentally, the entropy change is often calculated from bulk magnetization measurements, which yield the total entropy change (eq. (2.30)). It is impossible to independently estimate either the magnetic (ΔS_M) or the structural entropy (ΔS_{st}) changes from magnetization measurements. However, Gschneidner et al. estimated the contribution from the structural entropy changes for various giant MCE materials using an indirect approach. They utilized the fact that, by using different heat treatments, $Gd_5(Si_{4-x}Ge_x)$

near the composition with x = 2 forms in either the orthorhombic or monoclinic structures. $Gd_5Si_{2.09}Ge_{1.91}$ with an orthorhombic structure undergoes a second-order, purely magnetic phase transition at $T_C = 301$ K. In this material, the crystal structure remains orthorhombic throughout the entire temperature range. However, the same material with a monoclinic structure, goes through a first-order, coupled magentostructural transition at $T = 292$ K. At this temperature, the system transforms from a paramagnetic (PM) monoclinic phase to a ferromagnetic (FM) orthorhombic phase. In this case, the total entropy change (ΔS_T) is the sum of the structural (ΔS_{st}) and magnetic entropy changes (ΔS_M), whereas in the previous case (orthorhombic sample) there would be zero contribution from a structural entropy change. Next, the structural entropy change ($\Delta S_{st} = 9.2$ J/kg K) was estimated by subtracting the total entropy change for the orthorhomic sample (purely magnetic) from the total entropy change of the monoclinic sample (magnetic and structural). For the monoclinic $Gd_5(Si_{4-x}Ge_x)$ sample, a comparison of the structural entropy change, $\Delta S_{st} = 9.2$ J/kg K to the total entropy change, $-\Delta S_T = 18.4$ J/kg K clearly reveals that ΔS_{st} contributes about half of the total entropy change (ΔS_T). This is how coupled MSTs, where the structural entropy change can add to the magnetic entropy change, give rise to giant MCEs. A somewhat similar scenario will be discussed in chapter 4, where we will discuss the giant MCE in $(MnNiSi)_{1-x}(FeCoGe)_x$.

It is to be noted that the structural entropy change can work against the magnetic entropy change, and reduce the total entropy change [107]. A theoretical study by Vittorio Basso laid out the conditions for which the lattice entropy changes can add to the magnetic entropy changes to produce a large MCE [108].

FOPTs often yield large or giant MCEs, however the MCE usually occurs over a very narrow region because of the sharp nature of the phase transition [99]. In addition, the hysteresis effects generate energy loss, reducing the technological feasibility of the first-order materials. However, in a recent paper, Pecharsky et al. [109] laid out a framework in which giant MCEs from first-order materials can be utilized for magnetic refrigeration. It

is still a vibrant field of research, and extensive investigations are being conducted to find the ideal candidate for magnetic refrigeration as well as to understand the fundamental mechanism behind FOPTs.

Chapter 3
Experimental Methods for Studying Caloric Effects

3.1 Experimental Methods to Determine the MCE

A wide variety of techniques exists to experimentally determine the MCE potentials, the isothermal entropy changes (ΔS), and the adiabatic temperature changes (ΔT). These measurement techniques can be classified into two categories, direct and indirect measurements. Because of their convenience relative to direct measurements, MCE materials are often characterized through indirect measurements, for which widely used laboratory instruments, such as the SQUID MPMS by Quantum Design, vibrating sample magnetometers (VSM), the PPMS by Quantum Design, differential scanning calorimetry, etc. are used. The adiabatic temperature change, ΔT, can also be measured directly. However, direct measurements require purpose-built experimental setups, which are not commercially available. In our investigations, we mostly measured ΔS and ΔT indirectly from magnetization and heat capacity measurements. Brief descriptions of those measurements will be provided in this chapter.

Indirect Measurements Using Magnetization

The relation $\Delta S_{iso} = \int_{B_1}^{B_2} \left[\frac{\partial M(T,B)}{\partial T}\right]_T dB$ (eq. 2.14) is frequently used to calculate the isothermal entropy change (ΔS_{iso}) from experimental magnetization data. The isothermal entropy change is expected to be maximum around the ordering temperature, where the partial derivative $\partial M/\partial T$ is maximum. For practical purposes, we write eq. (2.14) in the following way to calculate ΔS_{iso} from the magnetization (M) versus magnetic field (B) data:

$$\Delta S_{iso}(T, B, P) = \frac{1}{\Delta T} \int_{B_1}^{B_2} [M(T + \Delta T, B, P) - M(T, B, P)]\, dB. \tag{3.1}$$

Fig. 3.1 shows the magnetization isotherms for $(MnNiSi)_{0.6}$ $(MnFeGe)_{0.4}$, measured at different temperatures spanning a MST. Each isotherm was measured in an applied magnetic field that increased from zero to $H = 5$ T. According to eq. (3.1), ΔS_{iso} between a

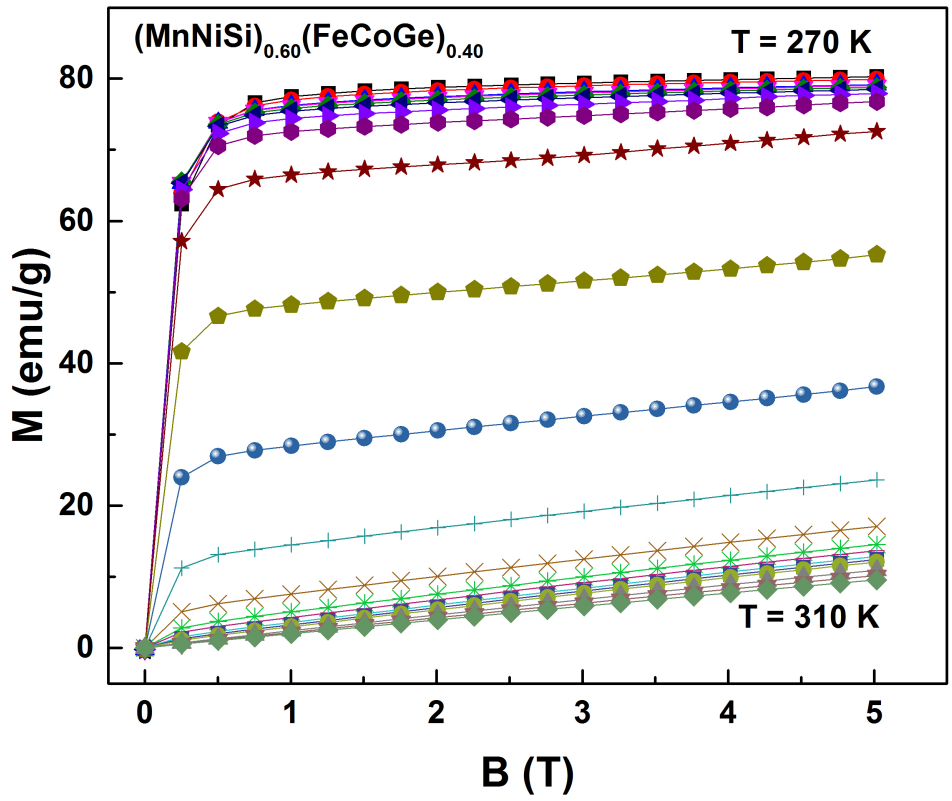

Figure 3.1: Magnetization isotherms (M vs. H) for $(MnNiSi)_{1-x}$ $(MnFeGe)_x$ at different temperatures for a field variation of 5 T. Each color and symbol represents a different isotherm.

given temperature is the area between two consecutive isotherms, separated by a temperature interval ΔT. For example, if we calculate the area under the isotherms at $T = 270$ K and 271 K, subtract the areas, and divide the value by the temperature interval, ΔT, the result would be the isothermal entropy change, ΔS_{iso}, at $T = 270.5$ K for a field variation of 5 T. This process is continued for a temperature span covering well above and below the phase transition temperature. From these data, a ΔS_{iso} vs. T plot is usually created for a full picture of the entropy change with respect to temperature. In most literature, ΔS_{iso} is reported in units of J/kg K. In order to better understand the applicability of a particular material in solid-state refrigeration devices, it is sometimes more insightful to report these values based on volume entropy density (i.e., mJ/cm^3 or J/m^3) [50]. This stems from the fact that the largest possible entropy change in the smallest possible volume is desirable for practical application purposes.

The isothermal entropy change (ΔS_{iso}) and adiabatic temperature change (ΔT_{ad}), as described by eqs. (2.16) and (3.1), can be used to accurately evaluate the magnetocaloric potentials for materials showing second order phase transitions. However, they are not technically valid in describing the magnetocaloric effects in the vicinity of first order phase transitions. By definition, the partial first derivatives of the Gibbs free energy (G) with respect to variables, such as temperature (T), magnetic field (B), or pressure (P), vary discontinuously at first order phase transitions. Therefore, in the vicinity of a truly discontinuous first order phase transition, the quantities $[\partial M(T,B)/\partial T]_B$, $[T/C_B(T,B)]$, or both, do not exist. Gschneidner et al. argued that these equations can still be applied, because first-order phase transitions in real systems occur over a finite temperature or field range [50]. This is the reason why Eq. 2.14 is widely used to evaluate the isothermal entropy change in MCE materials.

It had been proposed by Giguere et al. [110, 111] that, for materials undergoing FOPTs, the Clausius-Clapeyron equation should be used to estimate the entropy change instead of the Maxwell relation. However, Sun et al. [112] pointed out that the Clausius-Clapeyron equation can be derived as a special case of the Maxwell relation. They also argued that the Maxwell relation can take into account the changes in both the magnetic order and the order parameter (e.g., the coupled MST in $Gd_5Si_2Ge_2$), whereas the Clausius-Clapeyron equation only accounts for the change in magnetic order. Based on these arguments, Smith et al. [16] stated that the first-order nature of the transition by itself is not responsible for the breakdown of the Maxwell relation. During a FOPT, the system goes through a non-equilibrium process where two phases coexist (e.g., PM and FM phases). This is why the magnetization history of the sample can affect the value of the entropy change calculated using the Maxwell relation. Nevertheless, proceeding cautiously regarding factors such as the magnetization history of the sample and the rate of magnetic field and temperature changes, the entropy change can be evaluated accurately by using the Maxwell relation.

Through the Clausius-Clapeyron equation, the entropy change (ΔS_{iso}) can be calcu-

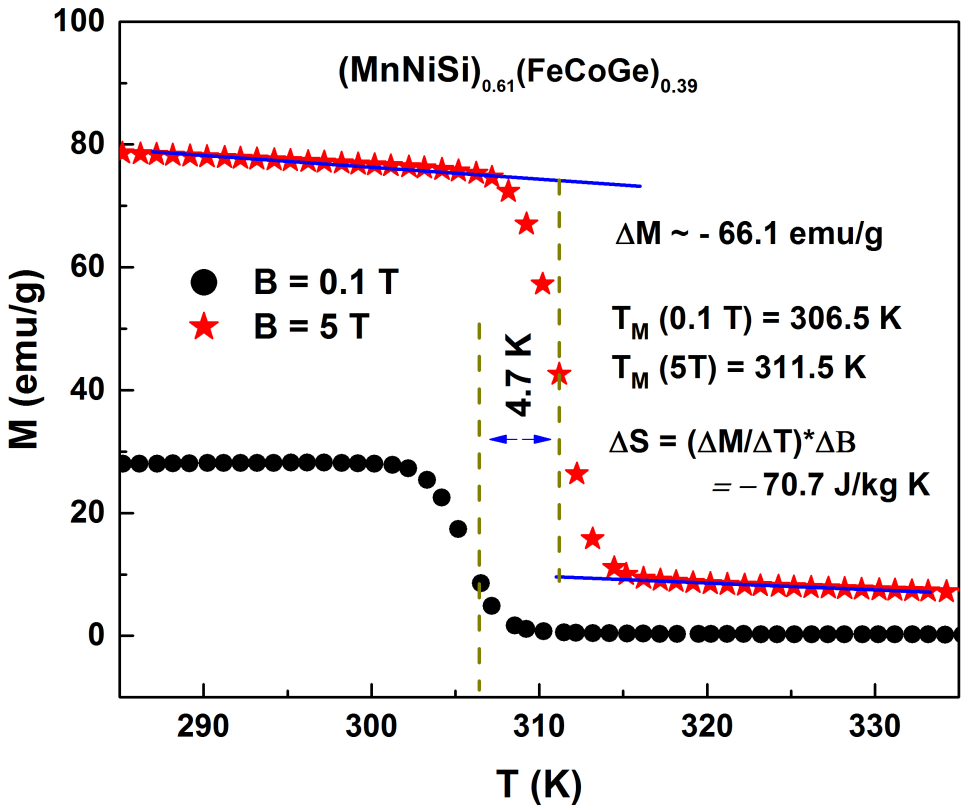

Figure 3.2: Temperature dependent magnetization (M vs. T) data for $(MnNiSi)_{1-x}$ $(MnFeGe)_x$ at $B = 0.1$ T and 5 T.

lated from temperature dependent magnetization (M vs. T) data. The equation is given by

$$\Delta S_{iso}(T, B, P) = \left(\frac{\Delta M(T, B, P)}{\Delta T}\right) \Delta B. \tag{3.2}$$

Fig. 3.2 shows the data and calculation of ΔS_{iso} using eq. (3.2). Here the magnetization as a function of temperature was measured in applied fields of $B = 0.1$ T and 5 T. According to this plot, the transition temperature shifts to higher temperature with increasing magnetic field. The shift in the transition temperature is ΔT and, in this case, is equal to 6 K. The difference between the magnetization values at the beginning and end of the transition, calculated from the high-field curve, gives the quantity ΔM. For this particular measurement, ΔB was 5 T. Using these values in eq. (3.2), the isothermal entropy change was estimated as $\Delta S_{iso} \simeq (\Delta M/\Delta T) \times \Delta B = [(-66.1/4.7) \times 5]\,\mathrm{J/kg\,K} \approx$ -70 J/kg K.

From an experimental point of view, bulk magnetization data as a function of temperature and magnetic field are relatively easy to obtain. This is why eq. (3.1) is frequently used to evaluate the isothermal entropy change in MCE materials [50]. In our investigations, we also used this method to calculate ΔS, which will be described in the following chapters.

Indirect Heat Capacity Measurements

The adiabatic temperature change (ΔT_{ad}) is often measured indirectly from heat capacity data. This data can also be used to estimate ΔS_{iso}. A detailed description of this procedure can be found in Chapter 5, where ΔS_{iso} and ΔT_{ad} for $DyRu_2Si_2$ were estimated indirectly from the heat capacity measurements. The measurements were performed using the heat capacity option in a Quantum Design Physical Property Measurement System (PPMS).

Direct Measurements of MCE

One very important parameter needed to characterize a MCE material is the adiabatic temperature change (ΔT_{ad}). The direct measurement of ΔT_{ad} requires purpose-built experimental setups. In principle, this measurement is rather simple; measuring the temperature change of the sample due to an applied magnetic field varied in time. However, maintaining adiabatic conditions is the most challenging and difficult obstacle that needs to be tackled when designing such device. In experimental conditions, the sample is often maintained in a quasi-adiabatic condition, which can be achieved by following one of two approaches. In the first approach, the sample is held stationary, while the magnetic field is varied. One benefit of this approach is that the sample can be placed in vacuum, which helps ensuring a high degree of adiabatic conditions. In the second approach, the magnetic field is kept constant, and the sample is moved relative to (out of) the constant magnetic field. In this way, even if the sample is not in complete thermal isolation, the quick extraction or insertion of a small sample from a fixed magnet ensures near adiabatic conditions [16].

Various kinds of magnets have been used to measure ΔT_{ad} directly. Electromagnets are often used, however they require a large amount of power, and the magnet itself creates

heat which needs to be kept away from the sample. On the other hand, permanent magnets do not require any additional power source, and various configurations are often used to achieve a varying magnetic field. This can be done by rotating the magnets, or by moving two magnets with respect to each other [16]. Superconducting magnets have also been used to reach high magnetic fields [113]. Another approach is to use pulsed magnetic fields to overcome the slow ramp rate of electromagnets [114]. The temperature is usually measured directly through thermocouples. The indirect measurement of the temperature through an acoustic detection technique was also conducted by Otowski et al. [16, 115].

At this point, a brief description of the experimental setup built by Bjøork et al. [116] to directly measure ΔT_{ad} may be helpful. In their setup, a thermocouple was sandwiched between two identical plates of the MCE material. This "sandwich" was then wrapped in insulating foam for thermal insulation, and placed in a sample holder. A hall probe to measure the magnetic field was inserted into the sample holder. The sample holder was then connected to a piston rod which moves the sample in and out of a magnetic field. A concentric Halbach cylinder was used as the permanent magnetic field source. While the piston was moved in and out of the magnet, the temperature of the sample was sensed by the thermocouple. The extraction movement of the sample was completed in less than 100 ms to ensure near adiabatic conditions. In order to measure the ΔT_{ad} vs. T data for a wide temperature range, the sample temperature was controlled by changing the temperature of the sample environment [16].

3.2 Experimental Methods to Determine the BCE

The barocaloric effect (BCE) generally arises due to first-order phase transitions, which are often hydrostatic pressure sensitive, and involve large volume changes during the phase transition. First-order transitions involve latent heat, which can be measured using a calorimeter. From the latent heat released/absorbed during a first-order transition, the isothermal entropy change can be calculated. Calorimetric measurements under applied pressure can be used to measure the isothermal entropy change (ΔS_{BCE}) due to the

barocaloric effect.

Calrimeters can be classified into two categories. One type of calorimeter is the differential scanning calorimeters (DSC). A DSC measures the heat-flux between the sample and a thermal bath, while the temperature is continuously changed (scanned). In these calorimeters, a dummy or reference sample is often measured in parallel with the sample to be measured, so that the measurement is differential. The other type of calorimeter applies a small heat pulse to the sample, and then the temperature of the sample is measured. This is also called adiabatic, relaxation, or ac calorimetry. This kind of calorimeter is best suited to study materials that undergo second-order continuous phase transitions, and have been used to directly measure the magnetocaloric effects in second-order MCE materials. On the other hand, DSCs are best suited to study the first-order phase transitions, since they measure the heat-flux, which can be used to calculate the latent heat of the transition [16, 117].

Since the barocaloric effect usually originates from first-order phase transitions, DSCs have been used to calculate ΔS_{BCE} through hydrostatic pressure calorimetry [71, 118]. In these devices, heat-flow curves ($\frac{dq}{dT}$ vs. T) are measured at various applied pressures, and in a temperature range that spans the first-order phase transition. The peaks in the DSC heat-flow data are a measure of the latent heat of the transition, which can be estimated by calculating the area under the heat-flow curve. From this data, the transition entropy can be calculated by using the relation

$$\Delta S_t(T,P) = S(T,P) - S(T_0,P) = \int_{T_0}^{T} \frac{1}{T}\frac{\dot{Q}(P)}{\dot{T}} dT, \tag{3.3}$$

where $\dot{Q}$ and $\dot{T}$ are the heat flux and temperature rate, respectively. From the pressure-dependent calorimetric data, the corresponding transition entropies for various applied pressures can be found. Next, ΔS_{BCE} can be easily calculated through the relation

$$\Delta S_{BCE} = \Delta S_t(T,P) - \Delta S_t(T,0). \tag{3.4}$$

Here, $\Delta S_t(T, 0)$ and $\Delta S_t(T, P)$ are the transition entropies at ambient pressure and at an applied pressure (P), respectively. Detailed descriptions of these measurements will be provided in Chapter 4.4. We have also designed and constructed an experimental setup to directly measure the adiabatic temperature change (ΔT_{BCE}) due to the barocaloric effect. A detailed description of this device is given in Chapter 4.5.

Chapter 4
The Magnetocaloric and Barocaloric Properties of $(MnNiSi)_{1-x}(FeCoGe)_x$

4.1 Introduction

As discussed in the previous chapters, a first-order coupled magnetostructural transition (MST) often gives rise to giant magnetocaloric effects. In this type of phase transition, the structural and magnetic entropy changes can sum together to create a large entropy change. In this regard, Mn-based MnTX systems (T = Co, Ni, and X = Ge, Si) are quite attractive, since some of the members of this family of compounds, such as MnNiGe, MnCoGe, CoMnSi, etc., exhibit both magnetic and structural phase transitions [119–127]. However, in order to generate a large magnetocaloric effect from this type of materials, some challenges must be overcome. First, the structural and magnetic transitions must coincide (i.e., they should occur simultaneously) to create a coupled MST. Second, the process of coupling the two phase transitions should not significantly decrease the overall magnetization of the system, as it might reduce the net entropy change. Third, in order to increase the real-life applicability, the coupled MST should occur near room temperature. These features can be achieved by tuning the phase transitions through various strategies, such as elemental substitution, stoichiometry variation, chemical or hydrostatic pressure application, and so on. As is the case with other well-known magnetocaloric materials, near MSTs a strong coupling between the magnetic and structural degrees of freedom usually gives rise to giant MCEs. The MSTs often involve a change in the crystal symmetry or

Parts of this chapter were published previously as Tapas Samanta, Pol Lloveras, Ahmad Us Saleheen, Daniel L. Lepkowski, Emily Kramer, Igor Dubenko, Philip W. Adams, David P. Young, Maria Barrio, Josep Ll. Tamarit, Naushad Ali, and Shane Stadler, *Applied Physics Letters* **112(2)**, 021907 (2018) and Tapas Samanta, Daniel L. Lepkowski, Ahmad Us Saleheen, Alok Shankar, Joseph Prestigiacomo, Igor Dubenko, Abdiel Quetz, Iain W. H. Oswald, Gregory T. McCandless, Julia Y. Chan, Philip W. Adams, David P. Young, Naushad Ali, and Shane Stadler, *Journal of Applied Physics* **117(12)**, 123911 (2015). Please refer to Appendix A for the permission of AIP Publishing. The author performed materials synthesis, including the exploratory single-element substitutions, room temperature XRD measurements, and pressure-dependent magnetization measurements. The pressure-dependent DSC measurements were performed in Spain at the Universitat Politècnica de Catalunya. The temperature-dependent XRD measurements were done at the University of Texas at Dallas. The author designed and constructed the experimental setup for the direct measurements of ΔT_{BCE} at the Louisiana State University.

volume, which can generate a large structural entropy change, increasing the likelihood of observing large caloric effects.

Stoichiometric MnNiSi undergoes two transitions. First is a second-order ferromagnetic (FM) to paramagnetic (PM) transition at $T_C = 662$ K. Secondly, it undergoes a structural transition from a low-temperature orthorhombic TiNiSi-type structure to a high-temperature hexagonal Ni_2In-type structure at a relatively high temperature of about 1200 K in the paramagnetic (PM) state [128, 129]. Our first objective was to couple these two transitions together and bring the resulting coupled MST to room temperature. In order to achieve this, a single-element substitution strategy was initially employed, with the intention to modify both the lattice parameters and the electronic structure. For this purpose, multiple elements, including Al, Sn, B, Ga, Cr, Ge, etc. were substituted at various sites in stoichiometric MnNiSi. However, this single element substitution strategy was not successful in coupling the two transitions; either the two transitions did not shift in the required directions (or not enough), or the other physical properties were not preferable. Once the single-element method was exhausted, an isostructural substitution strategy was employed, where MnNiSi was alloyed with FeCoGe. This material was chosen for two reasons: (i) it has a stable hexagonal Ni_2In-type structure with a purely second-order magnetic phase transition at $T_C = 370$ K and (ii) it has a large saturation magnetization ($M_S \sim 2\mu_B$) [130]. As a result of this substitution strategy, we observed a coupled MST near room temperature in $(MnNiSi)_{1-x}(FeCoGe)_x$, in a very narrow concentration range ($0.37 \leq x \leq 0.40$). The resulting transition was found to be highly sensitive to both FeCoGe concentration (x) and applied hydrostatic pressure. More interestingly, this MST gave rise to a large magnetocaloric effect in this system close to room temperature.

An external magnetic field acts as the stimulus that drives the MCE in a magnetic material. Apart from magnetic field, other forms of external stimuli such as stress, pressure, and electric field can generate caloric responses in materials. Probably the least studied solid state caloric phenomenon is the hydrostatic-pressure-induced caloric effect, known

as the barocaloric effect (BCE). This effect has shown promise for practical application after recent discoveries of this phenomenon in solid-state materials [51, 63, 64, 69, 118, 131–134]. It is also possible for a material to exhibit more than one caloric effect (even simultaneously) and hence function as a multicaloric material. The highly pressure sensitive nature of the MST along with the large volume change during the phase transition in $(MnNiSi)_{1-x}(FeCoGe)_x$, prompted the study of its barocaloric properties. These features of large magneto- and barocaloric materials were also predicted in theoretical calculations [135]. In this chapter, we will discuss the large MCE and BCE in $(MnNiSi)_{1-x}(FeCoGe)_x$. The observance of both BCE and MCE in the same material for the same phase transition qualifies it as a multicaloric material. From an applications perspective, this suggests the possibility of developing a refrigeration cycle that exploits both effects. In order to directly measure the adiabatic temperature change due to applied pressure, we constructed a purpose-built experimental setup in our lab. A detailed description of this setup will be discussed at the end of this chapter.

4.2 Experimental Methods

Pollycrystalline $(MnNiSi)_{1-x}(FeCoGe)_x$ (x = 0.37, 0.38, 0.39, and 0.40) were fabricated from the high-purity elements (better than 99.9%) Mn, Ni, Si, Fe, Co, and Ge by conventional arc-melting in an argon atmosphere. The materials for the barocaloric measurements were fabricated in an induction furnace under an argon atmosphere, since larger sample masses were required. The properties of the samples did not show any dependency on the fabrication method. The weight loss after melting was found to be negligible in both cases. After melting, the samples were placed inside an evacuated quartz tube and annealed at 750 °C in a tube furnace for 3 days, and subsequently quenched in ice-water. Room-temperature X-ray diffraction (XRD) measurements were done with a X-ray diffractometer using Cu Kα radiation and a θ - θ geometry. Temperature-dependent X-ray diffraction (XRD) measurements were conducted on a Bruker D8 Advance diffractometer using a Cu Kα radiation source (1.54060 Å) equipped with a LYNXEYE XE detector.

Rietveld refinement was used to determine unit cell volumes and phase fractions above and below the phase transition temperatures using TOPAS software by Bruker Corporation. The temperature-dependent X-ray measurements and refinements were performed by our collaborators at the University of Texas at Dallas. Magnetization measurements within a temperature interval of 10 - 400 K and up to 5 T applied magnetic fields were done with a superconducting quantum interference device (SQUID-MPMS) magnetometer by Quantum Design. Magnetic measurements under hydrostatic pressure were performed using a commercial BeCu cylindrical pressure cell manufactured by Quantum Design. Daphene 7373 oil was used as the pressure transmitting medium. The magnitude of the applied pressure was calibrated by measuring the shift of the superconducting transition temperature of Pb, which was placed in the cell with the sample as a reference manometer. Heat capacity measurements were done with a Quantum Design Physical Properties Measurement System (PPMS). The isothermal entropy changes (ΔS_{MCE}) due to the magnetocaloric effect were estimated from the isothermal magnetization curves [$M(H)$] using the integrated Maxwell relation, $\Delta S_{MCE} = \int_0^H (\partial M/\partial T)_H \, dH$. Calorimetric measurements with and without the application of hydrostatic pressure were carried out by our collaborators in Spain at the Universitat Politècnica de Catalunya, employing a purpose-built calorimeter as described in Ref. [118]. Direct measurements of the adiabatic temperature change on the fast release of hydrostatic pressure were performed in Spain following the procedure described in Ref. [71]. The adiabatic temperature change during pressurization of the sample was carried out using a purpose-built setup, described later in this chapter. In that setup, the temperature was measured with a type-J thermocouple that was embedded in a mixture of the powdered sample and a pressure transfer medium (a mixture of methanol and ethanol with a ratio of 4:1). The sample was pressurized to $P > 2$ kbar in about 30 s, and the temperature data were recorded every 0.04 s. The adiabatic temperature change was estimated from the zero-field heat capacity data and the transition entropy change [$\Delta S_t(T, P)$] curves following Ref. [69].

4.3 Giant MCE in $(MnNiSi)_{1-x}(FeCoGe)_x$

Fig. 4.1 shows the temperature dependent XRD patterns of $(MnNiSi)_{1-x}(FeCoGe)_x$ with x = 0.40, where the coupled MST occurs at $T_M \approx 275$ K. The XRD measurements were performed at $T = 270$ K, in the ferromagnetic (FM) phase just below T_M, and also in the paramagnetic (PM) phase at $T = 290$ K. A hexagonal Ni_2In-type crystal structure at $T = 290$ K indicates that the substitution of FeCoGe in $(MnNiSi)_{1-x}(FeCoGe)_x$ successfully stabilizes the high-temperature hexagonal phase at a much lower temperature than that of the parent MnNiSi. At $T = 270$ K, which is very close to T_M, an orthorhombic TiNiSi-type structure was identified with traces of the hexagonal phase. The coexistence of traces of both phases near the phase transition temperature is not unusual, and indicates that the phase transition involves a first-order structural transition between two crystal structures.

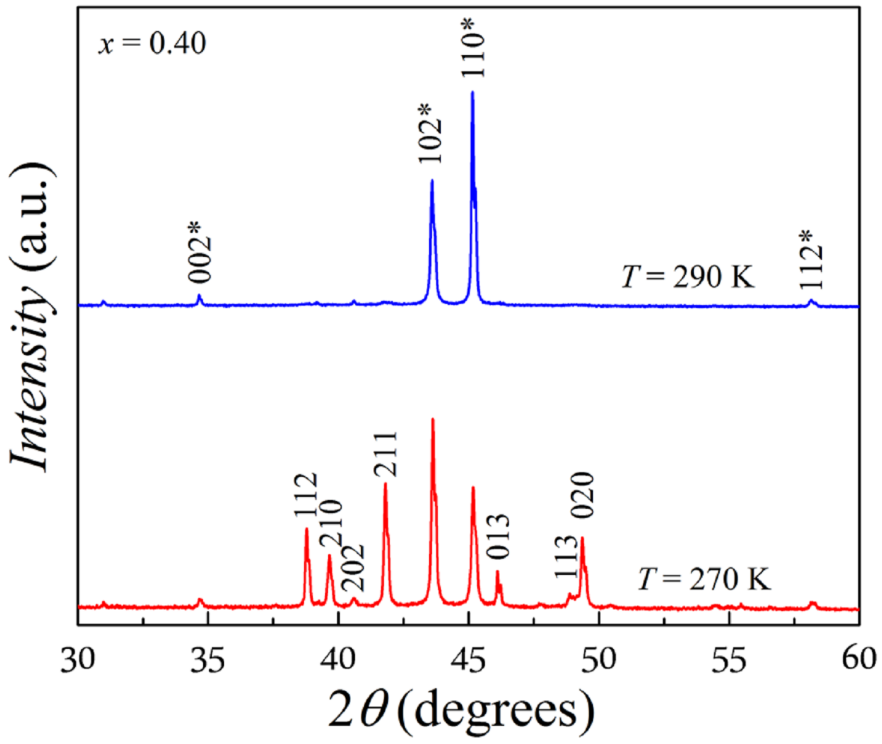

Figure 4.1: XRD patterns for $x = 0.40$ at temperatures just above and below the magnetostructural transition. The Miller indices of the high temperature hexagonal and low temperature orthorhombic phases are designated with and without asterisks (*), respectively.

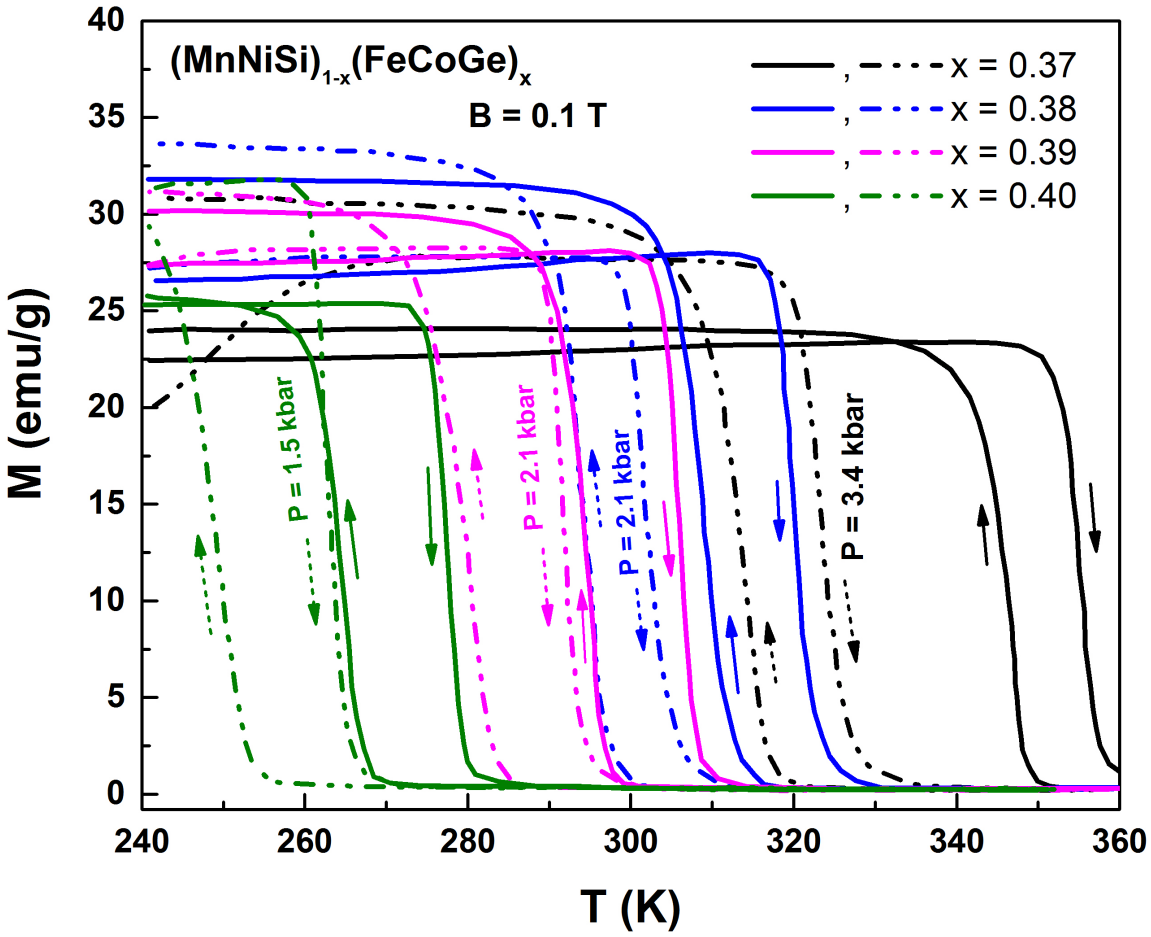

Figure 4.2: Temperature dependence of the magnetization (M) in the presence of a 0.1 T magnetic field (B) during heating and cooling for $(MnNiSi)_{(1-x)}(FeCoGe)_x$ at ambient pressure (solid lines) and at different applied hydrostatic pressures (broken lines).

The temperature-dependent XRD measurements, made just above and below the MST, were used to calculate a relative volume change of $\frac{\Delta V}{V} \sim 2.85\%$.

Fig. 4.2 shows the temperature dependent magnetization $[M(T)]$ data for $(MnNiSi)_{1-x}(FeCoGe)_x$, at ambient pressure as well as under applied hydrostatic pressure. The sample was first cooled down to $T = 10$ K from the paramagnetic state. After that, a 1 kOe magnetic field was turned on, and the magnetization was measured up to $T = 400$ K during heating at a rate of 2 K/minute, which is referred to as the zero-field-cooled (ZFC) protocol. Subsequently, the magnetization was measured under the same 1 kOe magnetic field from $T = 400$ K to $T = 10$ K during cooling, following the field-cooled-cooling (FCC) protocol.

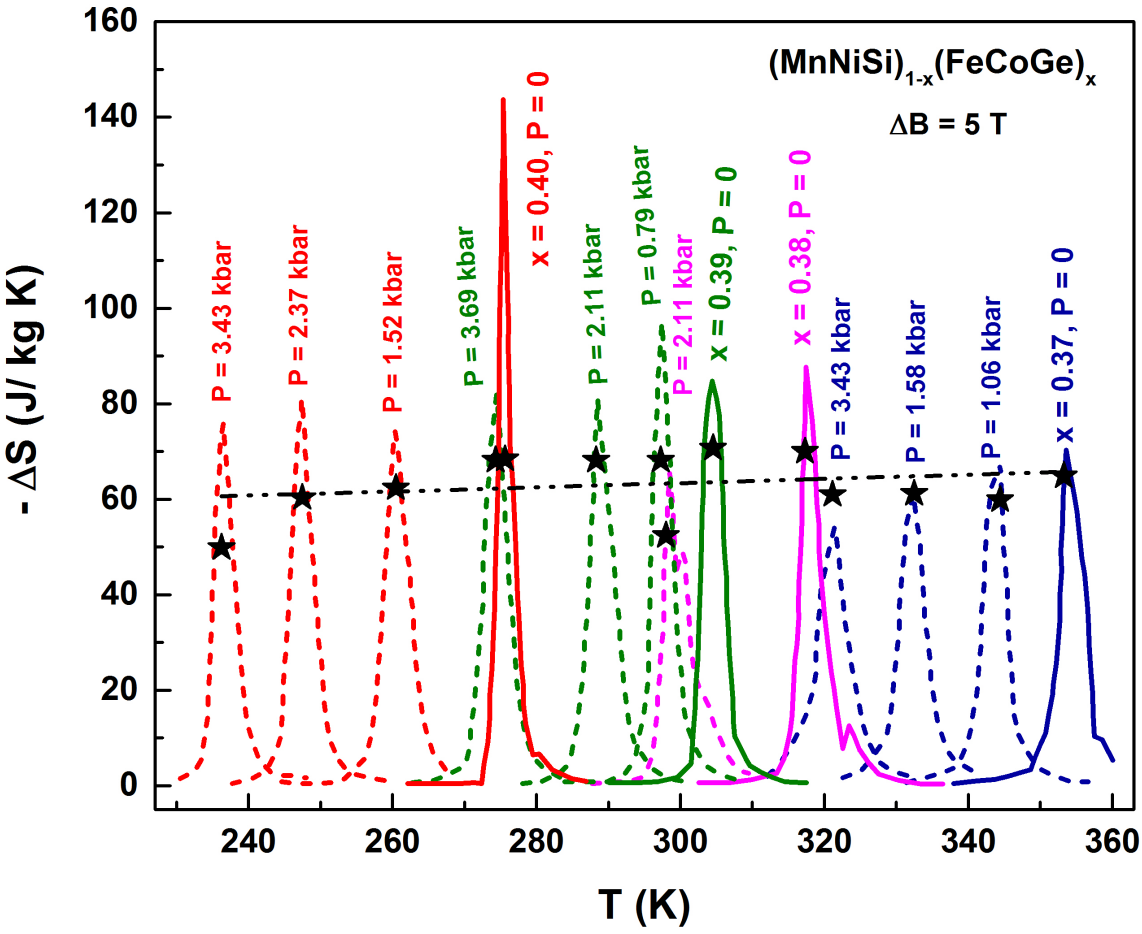

Figure 4.3: The isothermal entropy changes (ΔS) as a function of temperature were estimated for field changes of $\Delta B = 5$ T, measured at ambient pressure (solid lines) and at different hydrostatic pressures (broken lines). The "star" symbols inside each $-\Delta S(T)$ curve represents the corresponding total entropy change estimated by employing the Clausius-Clapeyron equation $[\Delta S \simeq (\frac{\Delta M}{\Delta T})\Delta B]$ for $\Delta B = 5$ T. A linear fit of these values, intended as a guide to the eye, is indicated by a black dotted line.

Near the phase transition temperature, the sharp change in magnetization indicates a magnetic transition from a high-temperature paramagnetic (PM) state to a low-temperature ferromagnetic (FM) state. Each of the $M(T)$ curves in Fig. 4.2 exhibits a thermal hysteresis between the heating (ZFC) and cooling (FCC) curves, indicating a first-order coupled magnetostructural transition (MST). In other words, the structural and magnetic transitions coincide to create a single, coupled, first-order MST at T_M between a low-temperature orthorhombic FM state to a high-temperature hexagonal PM state. The coupled nature of the phase transitions remains intact only for a narrow range of FeCoGe concentration,

Table 4.1: Transition temperatures (T_C or T_M) and $-\Delta S^{max}$ reported for materials exhibiting giant MCEs, including $(MnNiSi)_{1-x}(FeCoGe)_x$ (present work), for a field variation of 5 T near room temperature.

Material	T_C or T_M K	$-\Delta S^{max}$ J/kg K	References
Gd	294	10.2	[50]
$(MnNiSi)_{1-x}(FeCoGe)_x$			Present work
x = 0.40	276	143.7	
x = 0.39	305	85.2	
x = 0.38	318	87.5	
$(MnNiSi)_{0.56}(FeCoGe)_{0.44}$	292	11.5 for ΔB = 1 T	[122]
$(Mn_{1-x}Cu_xCoGe$			[121]
x = 0.08	321	53.3	
x = 0.085	304	52.5	
x = 0.09	289	41.2	
x = 0.095	275	34.8	
x = 0.1	249	36.4	
$MnCoGeB_x$			[120]
x = 0.01	304	14.6	
x = 0.02	287	47.3	
x = 0.03	275	37.7	
$Mn_{1-x}Cr_xCoGe$			[125]
x = 0.04	322	28.5	
x = 0.11	292	27.7	
x = 0.18	274	15.6	
$Mn_{1-x}V_xCoGe$			[126]
x = 0.01	322	8.7 for ΔB = 1.2 T	
x = 0.02	298	9.5	
x = 0.03	270	3.4	
$MnCo_{0.95}Ge_{1.14}$	331	6.4 for ΔB = 1 T	[127]
$Gd_5Si_2Ge_2$	272	36.4	[36]
MnAs	318	30	[136]
$MnFeP_{0.45}As_{0.55}$	305	18	[137]
$La(Fe_{0.88}Si_{0.12})_{13}H_1$	274	23	[40]
$Ni_{55.2}Mn_{18.6}Ga_{26.2}$	320	20.4	[138]
$Ni_2Mn_{1-x}Cu_xGa$			[41]
x = 0.25	318	64	
x = 0.26	309	42	

which is $0.37 \leq x \leq 0.40$. An increase in the FeCoGe concentration (x) shifts the transition temperature (T_M) towards lower temperature (see Fig. 4.2). Moreover, the applied hydrostatic pressure (P) also shows a similar effect, where the MST moves towards lower temperature at a rate of about 10 K per kbar ($dT_M/dP \sim$ -10 K/kbar).

The isothermal entropy change (ΔS) as a function of magnetic field and temperature was calculated using the integrated Maxwell relation, $\Delta S_{MCE} = \int_0^B (\partial M/\partial T)_B \, dB$. The

results are plotted in Fig. 4.3. This material shows a large entropy change at the MST for a concentration range of $0.37 \leq \mathrm{x} \leq 0.40$. Similar to the MST shown in the $M(T)$ curves of Fig. 4.2, an increase in FeCoGe concentration (x) shifts the peaks of the $\Delta S(T)$ curves towards lower temperature. The application of hydrostatic pressure also shifts the peaks of the $\Delta S(T)$ curves towards lower temperature at a rate of about -10 K/kbar.

The large magnetocaloric effect observed in this system exceeds or is comparable with the best magnetocaloric materials (see Table 4.1). Furthermore, the high sensitivity of the coupled MST to applied pressure, and the large volume change during the phase transition, bolster the possibility of observing the barocaloric effect in this system. In the next section, various aspects of the observed barocaloric effect in this system will be discussed.

4.4 Barocaloric Effects in $(\mathrm{MnNiSi})_{1-\mathrm{x}}(\mathrm{FeCoGe})_{\mathrm{x}}$

In Chapter 3, the experimental techniques to measure the barocaloric effect (BCE) were briefly discussed. The primary objective of these measurements is to measure the entropy change due to applied pressure. In general, the barocaloric effect arises due to a first-order phase transition, which involves latent heat. This feature of the first-order phase transition enables the utilization of calorimeters, since they can measure the latent heat during a phase transition. However, pressure-dependent calorimetry is required in order to measure the barocaloric effect. Since this type of experimental device is not readily or commercially available, we sent the samples to collaborators in Spain, where they had developed a purpose-built setup for pressure-dependent calorimetric measurements.

We selected a compound with $\mathrm{x} = 0.38$ from the $(\mathrm{MnNiSi})_{1-\mathrm{x}}(\mathrm{FeCoGe})_{\mathrm{x}}$ series. Since the application of pressure shifts the MST towards lower temperature, this particular composition was chosen as its transition temperature is above room temperature at ambient pressure ($T_M = 338$ K at $P = 0$). The idea was that, with an application of pressure, the MST would shift close to room temperature, and generate an entropy change at that temperature. In order to illustrate the effects of hydrostatic pressure and magnetic field on the MST, the temperature dependent magnetization $[M(T)]$ data measured at $B = 0.1$

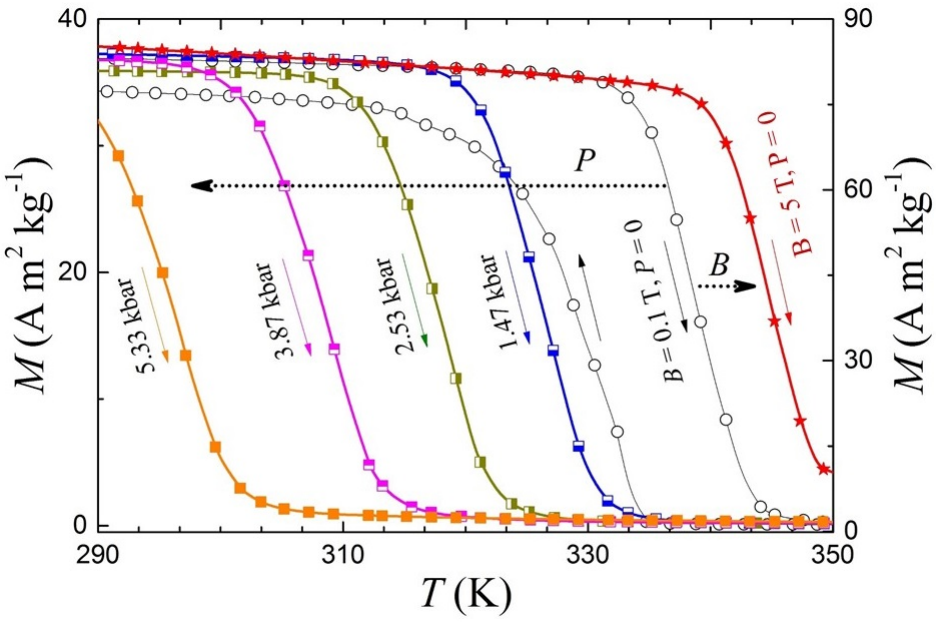

Figure 4.4: Temperature dependence of the magnetization (M) with $B = 0.1$ T for different applied hydrostatic pressures (P) and at ambient pressure for $(MnNiSi)_{(1-x)}(FeCoGe)_x$, x = 0.38 (left axis). $M(T)$ for the 5 T applied magnetic field (red line and symbols) is referred to the right axis. The dotted horizontal arrows indicate the shifts of the transition temperature with pressure and magnetic field.

T and 5 T magnetic fields, and for various applied hydrostatic pressures under $B = 0.1$ T, are shown in Fig. 4.4.

It is clear from from Fig. 4.4 that the application of hydrostatic pressure and magnetic field have opposite effects. An applied pressure shifts the MST (T_M) towards lower temperature, indicating the stabilization of the high-temperature, low-volume hexagonal phase. This feature gives rise to a positive isothermal entropy change (inverse BCE). On the other hand, an applied magnetic field stabilizes the low-temperature, ferromagnetic orthorhombic phase, which is associated with the shift of T_M towards higher temperature with increasing magnetic field. The observation of a negative isothermal entropy change (conventional MCE) due to the applied magnetic field is a manifestation of this feature.

The pressure-induced entropy change (ΔS_{BCE}) was calculated from the pressure dependent differential scanning calorimetry (DSC) data. The first step was to estimate the latent heat associated with the coupled first-order MST. For this purpose, the heat flow

curves ($\frac{dq}{dT}$ vs. T) were obtained from the DSC measurements at various pressures and temperature ranges spanning the first-order phase transitions. The area beneath the peak of a heat flow curve ($\frac{dq}{dT}$ vs. T) represents the latent heat of the phase transition. Next, the transition entropy change was calculated using the relation

$$\Delta S_t(T,P) = S(T,P) - S(T_0,P) = \int_{T_0}^{T} \frac{1}{T}\frac{\dot{Q}(P)}{\dot{T}}dT, \tag{4.1}$$

where $\dot{Q}$ and $\dot{T}$ are the heat flux and temperature rate, respectively. In this way, the transition entropy changes for various applied pressures were calculated and plotted against temperature. The pressure-induced entropy change (ΔS_{BCE}) can now be easily calculated using the relation

$$\Delta S_{BCE} = \Delta S_t(T,P) - \Delta S_t(T,0). \tag{4.2}$$

Here, $\Delta S_t(T,0)$ and $\Delta S_t(T,P)$ are the transition entropy changes at ambient pressure and at an applied pressure (P), respectively. Further details can be found in Ref. [139].

Fig. 4.5(a) shows the results, where $\Delta S_{BCE}(T)$ data were plotted for various applied pressures up to 2.7 kbar. The maximum value of the pressure-induced entropy change was found to be ΔS_{BCE}^{max} = 74 ± 4 J/kg K for P = 2.7 kbar. From a practical application point of view, it is advantageous to have the largest possible entropy change in the smallest possible volume. This is why it is more convenient to express the entropy change in terms of density rather than mass units [50]. For $(MnNiSi)_{1-x}(FeCoGe)_x$ with x = 0.38, ΔS_{BCE} = 540 ± 4 mJ/cm^3 K for P = 2.7 kbar. This value exceeds those reported for the best performing materials as summarized in Table 4.2.

Fig. 4.5(b) shows the field-induced magnetocaloric effect (ΔS_{MCE}) for this material. The same MST is responsible for the large ΔS_{MCE} as well as ΔS_{BCE}. Using a Maxwell relation, the ΔS_{MCE} was calculated from the magnetization isotherms, and a maximum value of ΔS_{MCE} = -58 J/kg K (or -425 mJ/cm^3 K) for B = 5 T was found. This value is also comparable to or larger than the other well-known magnetocaloric materials.

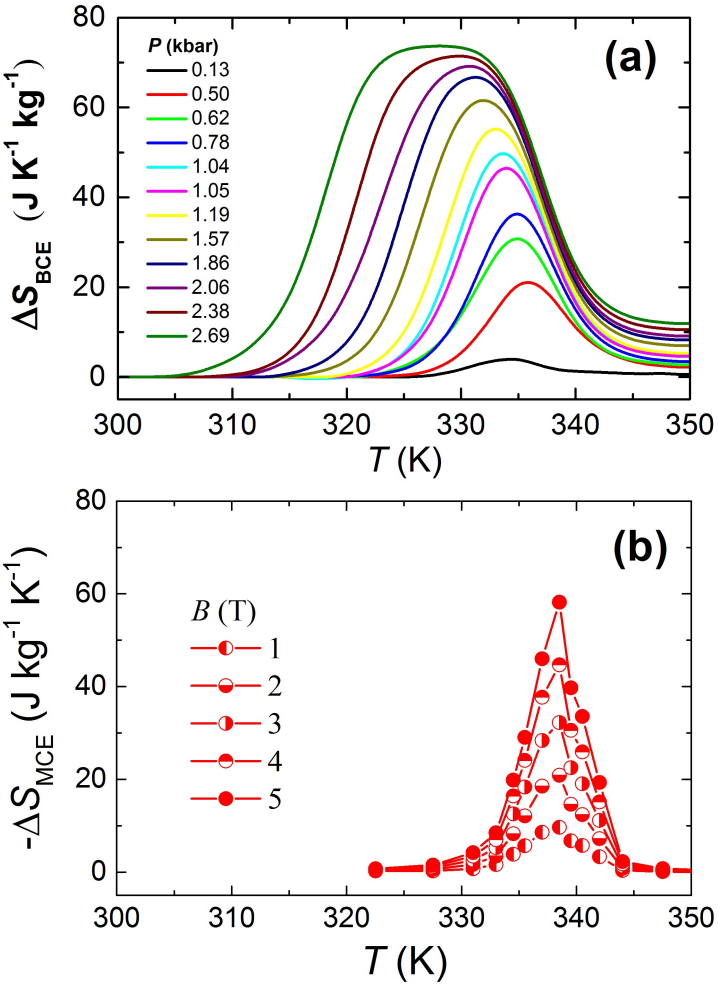

Figure 4.5: Entropy changes associated with (a) barocaloric and (b) magnetocaloric effects with the application of hydrostatic pressures up to 2.7 kbar and magnetic fields up to 5 T, respectively.

There is one important feature to be noted here: while the field-induced isothermal entropy change (ΔS_{MCE}) is negative (conventional), the pressure-induced isothermal entropy change (ΔS_{BCE}) is positive (inverse). Through a conventional magnetocaloric effect, an application of magnetic field should increase the temperature of the material, whereas the application of pressure would decrease its temperature through an inverse barocaloric effect. This particular feature of the inverse barocaloric effect, along with the fact that the MST is very close to room temperature, proved to be quite advantageous when we developed an experimental setup to directly measure the pressure-induced temperature change.

Table 4.2: Parameters of materials exhibiting giant multicaloric effects at first-order phase transitions including $(MnNiSi)_{1-x}(FeCoGe)_x$ with x = 0.38 (present work) including the isothermal entropy change $\mid \Delta S \mid$ and adiabatic temperature change $\mid \Delta T \mid$ due to changes of hydrostatic pressure P (BCE) and magnetic field H (MCE). Entries inside brackets {....} were derived from direct measurements. No data were available for entries indicated by "–". The mass density is ρ. Entries inside round brackets (....) denote parameters derived from $-c\Delta T \approx T\Delta S$ using zero-field heat capacity data.

Materials	T K	$\mid \Delta S_{BCE} \mid$ mJ/cm^{3}K	$\mid \Delta T_{BCE} \mid$ K	P kbar	$\mid \Delta S_{MCE} \mid$ mJ/cm^{3}K	$\mid \Delta T_{MCE} \mid$ K	H T	ρ g/cm^3	Refs.
$Ni_{49.26}Mn_{36.08}In_{14.66}$	293	200	(4.5)	2.6	82	(1.3)	0.94	8.2	[118]
$Gd_5Si_2Ge_2$	270	82.5	{1.1}	2.9	120	(7)	2	7.5	[36, 71]
$LaFe_{11.33}Co_{0.47}Si_{1.2}$	237	63.5	{2.2}	2.0	76	–	5	7.3	[68]
						{0.9}	1		
$Fe_{49}Rh_{51}$	308	123.5	(8.1)	1.1	120	(6)	2	9.8	[63, 64]
$MnCoGe_{0.99}In_{0.01}$	308	413	(18.5)	3.0	95	(2.8)	2	7.95	[133, 140]
			{9.4}	3.0		(0.9)	1		
Mn_3GaN	285	170	(4.8)	1.39	–	–	–	7.6	[69]
$(NH_4)_2SO_4$	219	106	(8)	1.0	–	–	–	1.8	[131]
$(MnNiSi)_{0.62}(FeCoGe)_{0.38}$	338	538	{3.1}	2.0	152	(2.4)	2	7.3	Present work
			{4.3}	2.5					
			(16)	2.7					

It is crucial to measure the adiabatic temperature change (ΔT_{BCE}) due to the BCE in order to have a complete understanding of the caloric behavior of the material. The pressure-induced adiabatic temperature change can be estimated indirectly through heat-capacity measurements at zero field and the transition entropy change $[\Delta S_t(T, P)]$ data. The details of this method can be found in Ref. [69]. In this way, an estimated $\mid \Delta T_{BCE} \mid$ = 16 K was calculated for P = 2.7 kbar, as shown in Fig. 4.6 ($\mid \Delta T \mid_{BCE,cal}$). However, this value of ΔT_{BCE} obtained through an indirect method is likely to be an overestimation. On the other hand, direct measurements are prone to underestimate ΔT_{BCE} because of the heat flow to and from the surroundings originating from the non-adiabatic conditions present in the experimental systems.

Nevertheless, direct decompression measurements carried out in Spain (see Ref. [71] for details of the experimental system) resulted in $\Delta T_{BCE} \sim +3.1$ K for P = 2 kbar as shown in Fig. 4.6 ($\Delta T_{BCE,exp}$). In light of the previous argument about the inverse

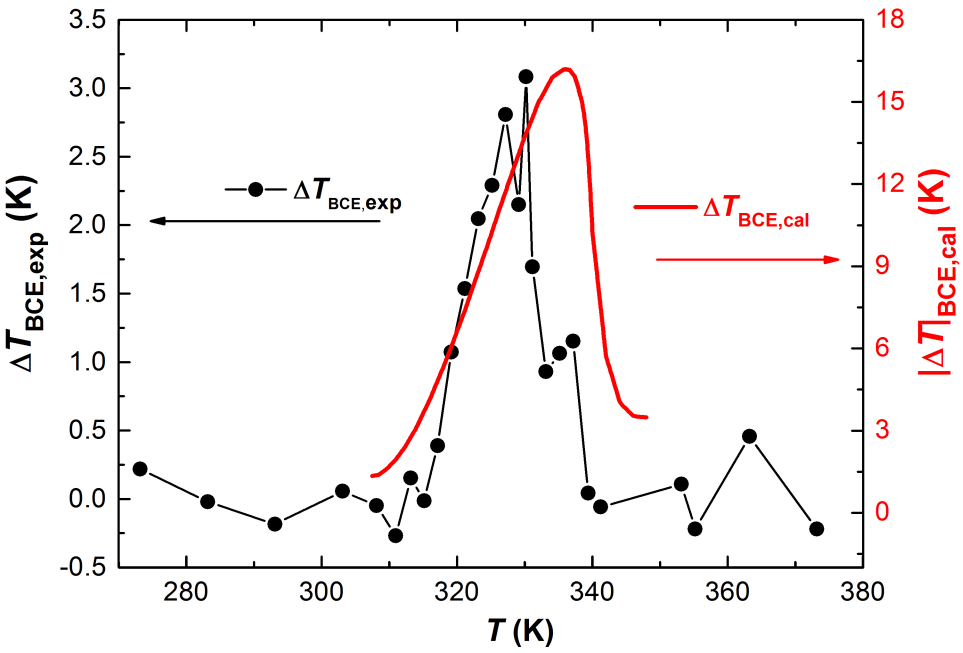

Figure 4.6: The adiabatic temperature change ($\Delta T_{BCE,exp}$) from depressurization from 2 kbar to atmospheric pressure (left axis) and the same ($\Delta T_{BCE,cal}$), estimated from zero-field heat capacity data (right axis).

barocaloric effect, the sign of the ΔT_{BCE} was expected to be positive during decompression. Inversely, ΔT_{BCE} should be negative during compression. In order to investigate this phenomenon, we constructed an experimental setup to measure the direct temperature change on compression. The details of this setup will be discussed in the next section.

4.5 An Experimental Setup to Directly Measure Temperature Change Due to Hydrostatic Pressure: Barocaloric Effects

An experimental setup was designed to directly measure the adiabatic temperature change (ΔT_{BCE}) with applied pressure. The advantage of this device is that it can measure during both compression and decompression. In this setup, a manually operated hydrostatic pressure generator was used to apply hydrostatic pressure up to 3 kbar to solid samples near room temperature. The resulting adiabatic temperature changes were successfully observed and recorded. In this section, a brief overview of the design and the working mechanism of this setup are provided. In order to obtain an accurate value of ΔT_{BCE}, it is important to conduct the experiment under adiabatic conditions. Although this simple

experimental setup did not maintain perfect adiabatic conditions, measures can be taken to improve the overall performance. The reasons for non-adiabatic conditions, as well as what steps can be taken in future to counter these issues, will be discussed.

Description

Fig. 4.7 shows a schematic diagram of the direct barocaloric measurement apparatus. The components include the following (going from left to right): a reservoir to contain the pressure conducting fluid, a high pressure valve V_1, a four-way "cross" or "sleeve" C_1, a high pressure generator, a pressure gauge (G_1), a high pressure valve (V_2), a three-way junction (C_2), a pressure gauge (G_2), an elbow (C_3), a reactor chamber, and a thermocouple. A clear tube (seen in Fig. 4.8) was also connected from the three-way valve V_1 to the reservoir via a check-valve (connected vertically at the left of pressure gauge G_1 in Fig. 4.8), which allowed the system to be purged of air bubbles. This check-valve allows fluid motion only from the system to the reservoir. The reservoir is also connected to the valve V_1 via another check-valve and clear tube (seen in Fig. 4.8) that allows flow only to the system from the reservoir. Using the two check-valves, the pressure conducting fluid could be drawn in from the reservoir on the out-stroke of the piston of the pressure generator. With the valve open to the check-valve return, the in-stroke of the piston would move fluid through the entire system, and fluid could return to the reservoir. This was repeated until no air bubbles were seen in the return tube. All of the abovementioned components were purchased from High Pressure Equipment Company.

In this instrument, a mixture of 4:1 (by volume) methanol to ethanol was used as the pressure conducting medium. The high pressure generator is a manually operated piston (hydrostatic) screw pump. It compresses any liquid within a small volume to develop pressure. To prepare the system for a measurement, the first step was to draw the pressure conducting fluid into the system so that it could be compressed and pressure can be generated. At this stage, valve V_1 was open while valve V_2 was closed and, by rotating the handle of pressure generator counter-clockwise, the piston recedes, and the alcohol mixture

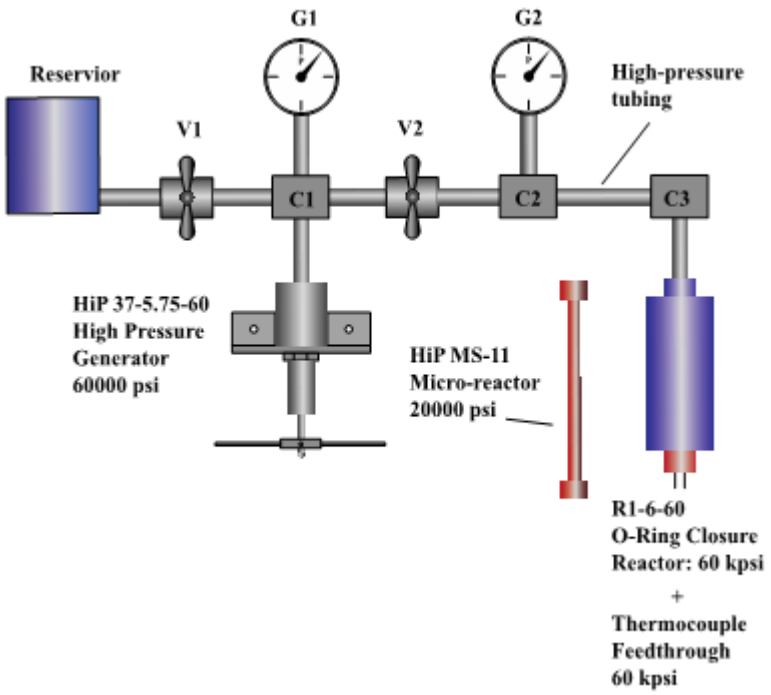

Figure 4.7: Schematic diagram of the barocaloric device to directly measure ΔT_{BCE}.

is drawn in. During this drawing process, bubbles sometimes formed in the pressure conducting fluid and, if these bubbles are present in the system during the compression stage, the maximum achievable pressure would be severely reduced. After drawing in fluid via the valve V_1, this valve was closed (valve V_2 is also closed), and by rotating the handle of the pressure generator the system becomes pressurized. During compression, the pressure can be read from the gauge. After one full stroke, the valve V_1 was opened for purging and, initially, a significant number of bubbles could be seen escaping the system through the purge point and traveling back to the reservoir via the check-valve. It should be noted that, during this process, fluid could not flow to the reservoir via any other path other than the purge point because of the other check-valve restricting flow to the reservoir. After the bubbles and fluid flow stopped, pressure conducting fluid was drawn again and the whole cycle was repeated until bubbles were no longer seen, or the desired pressure could be generated from one stroke of the pressure generator. The target pressure was 2.5 - 3.0 kbar.

Once one stroke of the pressure generator could generate the needed pressure, valve V_2 was opened, and the sample in the reactor could be pressurized (V_1 to be remained closed from now on unless drawing in fluid is required). Before opening valve V_2, the handle of the pressure generator was rotated counter-clockwise all the way to the initial position where pressure reads "zero" at the gauge. With V_1 closed and V_2 opened, the pressure generated by the generator is seen only by the sample and the gauge G_2 The handle could then be rotated clockwise to compress the fluid and pressurize the system in the reactor.

A type J thermocouple that can withstand up to 4 kbar pressure was inserted into the reactor through the high-pressure feedthrough at the bottom. A granulated sample was inserted into the reactor from one end of the reactor, while the thermocouple probe was inserted in the other end in such a way that it is buried at the center of the sample. The terminals of the thermocouple were connected to a Keithley voltmeter which read the thermocouple voltage. A National Instruments USB-232 adapter was used to relay data from the Keithley to a computer, where temperature vs. time data was plotted and observed in real time through a LabVIEW control program. In order to conduct one measurement, the system was pressurized by rotating the handle of the pressure generator

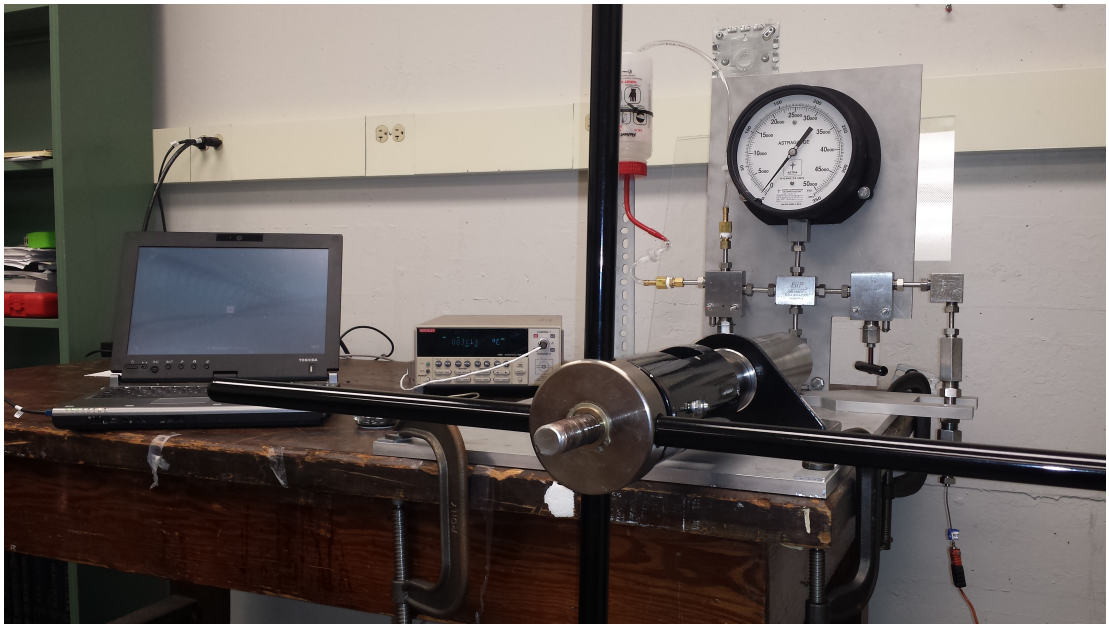

Figure 4.8: A picture of the experimental setup.

clockwise and, during this compression, the temperature change of the sample with respect to time was monitored and recorded through the LabVIEW program. It took about 30 seconds to pressurize the system from atmospheric pressure to ≈ 2.5 kbar. Fig. 4.8 shows a picture of the real experimental setup. In this picture, gauge G_1 was removed and replaced with a clear reservoir return tube and a check-valve.

Results

Fig. 4.9 shows the data obtained from one direct ΔT_{BCE} measurement. Since this home-built experimental device could not operate above room temperature, we chose a material whose phase transition temperature is close to room temperature. In the previous section, the barocaloric effects were measured for the x = 0.38 composition with $T_M = 338$ K at $P = 0$. In this device, a material with a slightly different composition (x = 0.39) was used (instead of x = 0.38) as its phase transition temperature is close to room temperature. Other than the lower transition temperature ($T_M \sim 300$ K), the material with x = 0.39 behaved nearly identical to that with x = 0.38. Before the measurement, the sample was heated well beyond and then cooled well below the transition temperature. This temperature cycling was necessary to remove the sample's structural and magnetization history, and to make sure that the pressurization process starts just above the transition temperature, so that the applied pressure can immediately shift the transition temperature. In this case (Fig. 4.9), the compression started at 18.4 °C and the temperature immediately started to increase due to the heating of the pressure conducting medium. During this time, the temperature of the sample started to decrease as the MST was being initiated, but this effect was not readily visible because of the rise of the pressure conducting fluid's temperature. As the pressure increases the cooling effect originating from the sample eventually surpasses the heating effect from the pressure conducting fluid, and a sharp drop in temperature was observed. For the sample shown in Fig. 4.9 this drop was 3.8 °C for an applied pressure of $\Delta P \sim 2.4$ kbar. This value represents the minimum directly measured temperature change, ΔT_{BCE}. After the application of the 2.4 kbar pressure, the

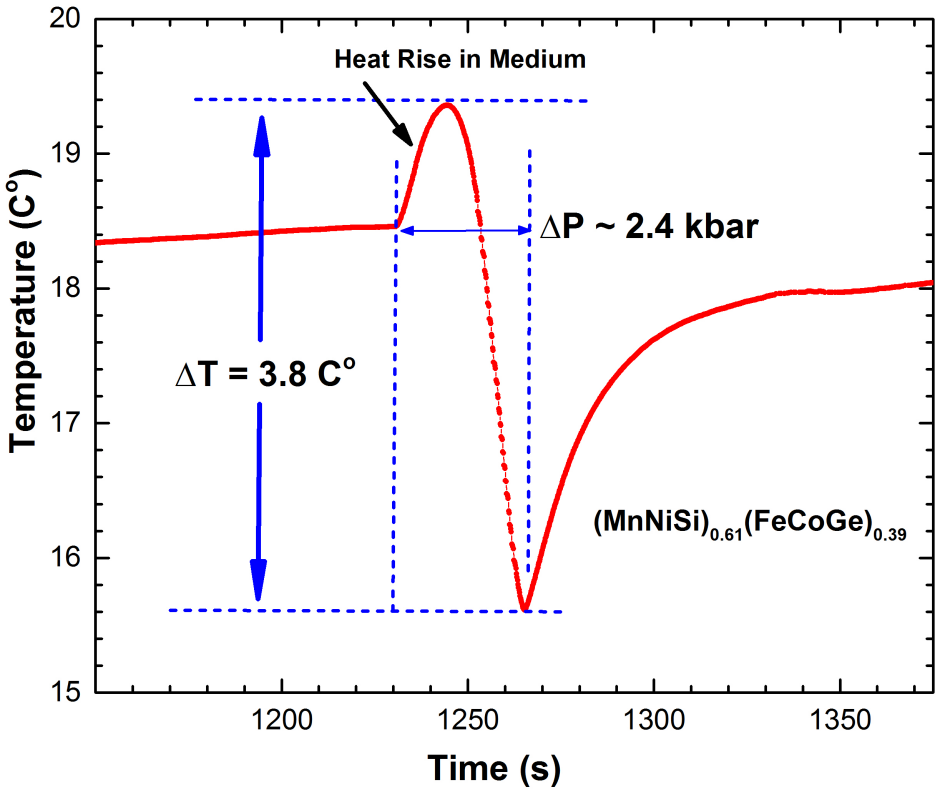

Figure 4.9: Direct measurement of ΔT_{BCE} conducted with the experimental device.

system was kept pressurized at that value until it warmed back to room temperature. The rise in temperature in Fig. 4.9 after the sharp drop represents this process and it can be directly attributed to the non-adiabatic condition and heat exchange of the sample reactor with the surroundings.

We utilized a larger reactor chamber to exert a higher amount of pressure on the sample. This chamber can contain more than 20 grams of sample (the smaller chamber only holds around 6 grams of sample). We used the same sample as in the smaller chamber (x = 0.39). With this larger chamber in place, a maximum $\Delta T_{BCE} \sim -$ 4.3 K for $P = 2.5$ kbar at $T = 295$ K was observed. The negative temperature change also confirms the effects of the inverse BCE. In both cases, compression and decompression, the values of ΔT_{BCE} are comparable to the magnetic field induced adiabatic temperature changes reported for giant magnetocaloric materials with $\Delta H = 2$ T (Table 4.2).

As discussed in the previous chapters, the magnetostructural transition temperatures

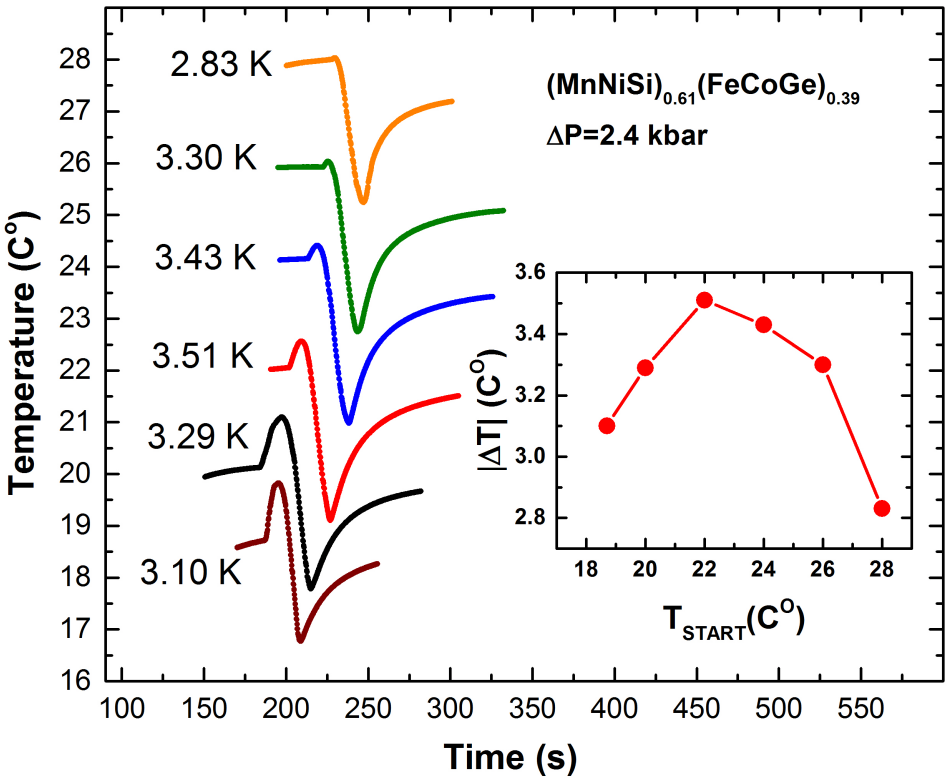

Figure 4.10: Dependence of ΔT_{BCE} on the starting temperature of pressurization, T_{START}. The curves are shifted horizontally for clarity. (Inset) The maximum values of ΔT_{BCE} for various starting temperatures (T_{START}).

of these systems are highly sensitive to applied pressure and they also posses thermal hysteresis. This is why, ΔT_{BCE} strongly depends on the temperature at which pressurization is started. This dependence is clearly visible from Fig. 4.10 where the inset shows ΔT_{BCE} as a function of T_{start}.

Discussion

The experimental setup demonstrates the inverse barocaloric effect by providing a direct measurement of the pressure-induced temperature change (ΔT_{BCE}). It can be noted here that the applied pressure (compression) decreased the temperature of the sample, in contrast to the usual scenario (i.e., conventional barocaloric materials), where pressure or stress increases the temperature of the material. For instance, before performing the measurement with the sample, we conducted the measurement with only the pressure conducting fluid. In that case, applied hydrostatic pressure increased the fluid's temperature,

which is also quite intuitive. However, in this sample $[(MnNiSi)_{0.61}(FeCoGe)_{0.39}]$, pressure shifts the transition temperature towards lower temperatures, indicating the stabilization of the high-temperature hexagonal phase with pressure. This causes the inverse BCE and a negative adiabatic temperature change. This negative temperature change due to inverse BCE was expected in this sample, and proves the veracity of the measurement.

As discussed in the previous chapters, the theoretical calculations predict much larger values of ΔT_{BCE}. The reduced values observed in the direct measurement are due to the non-adiabatic conditions in the setup and the heating of the pressure conducting medium. To achieve a good approximation to adiabatic conditions, the reactor (sample chamber) must be better isolated from the rest of the system and environment. By using double layered and thermally insulated reactor, the conditions may improve. However, the reactor will always be in some form of thermal contact with the system through the pressure

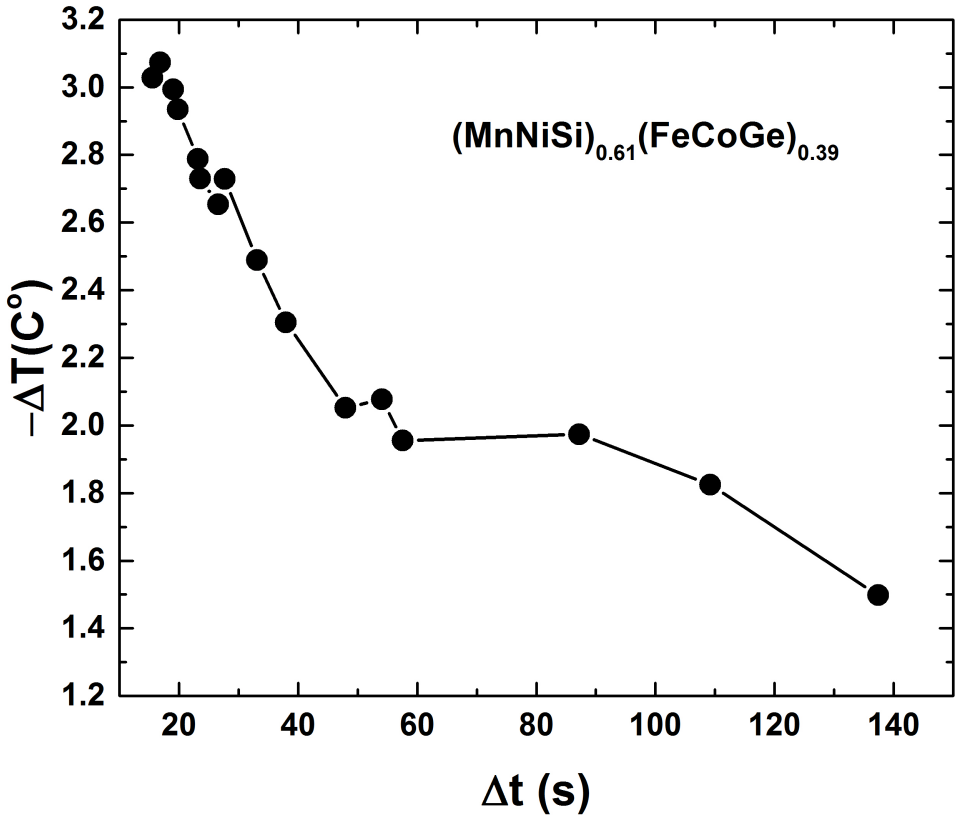

Figure 4.11: ΔT_{BCE} as a function of pressurization time (Δt).

conducting medium and thus damaging the adiabatic condition. Another way to improve the conditions would be to apply pressure on the material as quickly as possible and hence denying the time needed for the system to exchange heat. From Fig. 4.11, it can be seen that there is a dependence of ΔT_{BCE} on the speed at which pressure is applied. The faster the pressure application, the greater value of ΔT_{BCE} was observed.

There are plenty of opportunities for improvement in this setup. An automated pressure generator would greatly improve the rate at which pressure can be applied. Having a pressure gauge whose data can be read digitally and recorded in real-time would allow us to monitor the temperature change with respect to pressure. Moreover, having the ability to control temperature of the reactor (sample) would enable the system to investigate barocaloric effects in materials whose transition temperatures are not near room temperature. This temperature control would significantly increase the versatility of the instrument.

In this chapter, we observed the effects of applied hydrostatic pressure on coupled magnetostructural transitions. Hydrostatic pressure can also significantly modify metamagnetic transitions. In the next chapter, we will discuss the dramatic pressure dependence of the metamagnetic transitions and the magnetocaloric properties of $DyRu_2Si_2$.

Chapter 5
The Influence of Hydrostatic Pressure on the Magnetic and Magnetocaloric Properties of $DyRu_2Si_2$

5.1 Introduction

Although a large magnetocaloric effect near room temperature is the most sought after feature in MCE materials, MCE at low temperature is also useful for specific technological purposes, such as space science and, more prominently, in gas liquification [46–48]. Some antiferromagnetic systems are good candidates for that temperature range since they can show large MCE values due to magnetic field induced metamagnetic transitions from antiferromagnetic (AFM) to ferromagnetic (FM) states [46]. In this chapter, findings on the magnetocaloric and magnetic properties of $DyRu_2Si_2$ will be presented. This compound belongs to a class of materials with the general formula RT_2X_2, where R is a rare earth element, T is a transition metal, and X is silicon or germanium. These materials show a wide variety of properties such as heavy fermionic behavior, hidden order, superconductivity, complex and multiple magnetic transitions [141, 142], etc.

In this investigation, we observed a peak value of the total isothermal entropy change ΔS_T) of 6.64 J/kg K for a 7 T magnetic field change at $T = 29.2$ K. An adiabatic temperature change (ΔT_{ad}) of 8.2 K for a 5 T magnetic field change was observed at $T = 5.1$ K. For comparison, a few other materials in this class, including $GdCr_2Si_2$ [143], $HoRu_2Si_2$ [47], and $ErRu_2Si_2$ [46], were reported to show magnetic entropy changes (ΔS) of 14.1 J/kg K, 9.1 J/kg K, and 19.3 J/kg K at $T = 8$ K, 19 K, and 5.5 K, respectively, for a field change of 5 T. In the case of $ErRu_2Si_2$, an adiabatic temperature change of $\Delta T_{ad} =$ of 12.9 K was found at $T = 5.5$ K for a 5 T magnetic field change.

In our study, $DyRu_2Si_2$ showed magnetostrictive behavior, and the volume magnetostriction ($\Delta V/V$) was estimated from pressure-dependent magnetization measurements.

Reproduced from [Ahmad Us Saleheen, Tapas Samanta, Mojammel Khan, Philip W. Adams, David P. Young, Igor Dubenko, Naushad Ali, and Shane Stadler, *Journal of Applied Physics* **121(4)**, 045101 (2017)], with the permission of AIP Publishing (see Appendix A).

Hydrostatic pressure significantly altered the saturation magnetization and magnetic interactions, as well as the magnetocaloric properties of this compound.

5.2 Experimental Methods

Pollycrystalline $DyRu_2Si_2$ buttons (approximately 2 g) were fabricated from the high-purity elements (better than 99.9%) Dy, Ru, and Si by conventional arc-melting in an argon atmosphere. The weight loss after melting was found to be less than 0.3%. The samples were placed inside an evacuated quartz tube and annealed at 750 °C in a tube furnace for 5 days and slowly cooled to room temperature. X-ray diffraction (XRD) measurements were done with a room-temperature X-ray diffractometer using Cu Kα radiation and a θ - θ geometry. Magnetization measurements within a temperature interval of 2 - 400 K and up to 7 T applied magnetic fields were done with a superconducting quantum interference device (SQUID-MPMS) magnetometer by Quantum Design. Irregularly shaped samples of about 3 mg were used in these measurements. Magnetic measurements under hydrostatic pressure were performed using a commercial BeCu cylindrical pressure cell manufactured by Quantum Design. Daphene 7373 oil was used as the pressure transmitting medium. The magnitude of the applied pressure was calibrated by measuring the shift of the superconducting transition temperature of Pb, which was placed in the cell with the sample as a reference manometer. Heat capacity measurements were done with a Quantum Design Physical Properties Measurement System (PPMS). For this purpose, a $4.4 \times 1 \times 0.6$ mm sample with a mass of 18 mg was cut using a spark cutter.

5.3 Results and Discussion

$DyRu_2Si_2$ crystallizes at room temperature in the body centered tetragonal $ThCr_2Si_2$-type structure with space group $I4/mmm$, where only the Dy atoms possess a magnetic moment [144–147]. From the room temperature XRD pattern for $DyRu_2Si_2$ (Fig. 5.1), the $ThCr_2Si_2$-type tetragonal structure was verified. The lattice parameters were calculated as $a = 4.147(8)$ Å and $c = 9.522(8)$ Å, consistent with previously reported values [148].

The magnetization as a function of temperature (M vs. T) with $H = 0.1$ T at atmo-

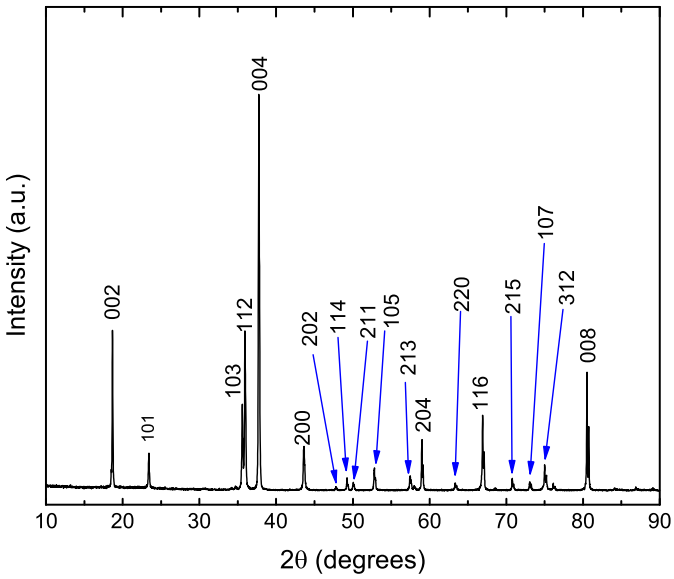

Figure 5.1: Room temperature powder XRD pattern for $DyRu_2Si_2$.

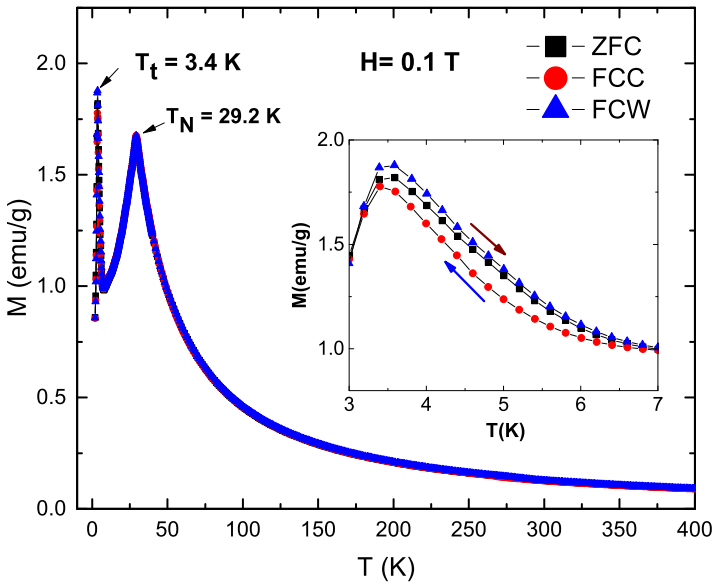

Figure 5.2: Magnetization (M) vs. temperature (T) for $DyRu_2Si_2$ at an applied magnetic field of $H = 0.1$ T at atmospheric pressure. (Inset) Zoomed in view of the same data to show thermal hysteresis.

spheric pressure is shown in Fig. 5.2. Two magnetic transitions, one at $T_N = 29.2$ K and another at $T_t = 3.4$ K, are clearly visible. A small but distinct hysteresis of about 0.3 K was observed between the zero-field-cooled (ZFC) warming and field-cooled-cooling (FCC) curves in the temperature range from $T_t = 3.4$ K to about 8 K. Previous studies reported another transition at $T_t^{'}$=1.5 K [144, 145, and references therein], but this was beyond the temperature range of our instrument. $DyRu_2Si_2$ has three temperature-dependent phases, namely: a low temperature phase (LTP) below $T_t^{'}$, an intermediate temperature phase (ITP) at $T_t^{'} < T < T_t$, and a high temperature phase (HTP) at $T_t < T < T_N$ [144, 145].

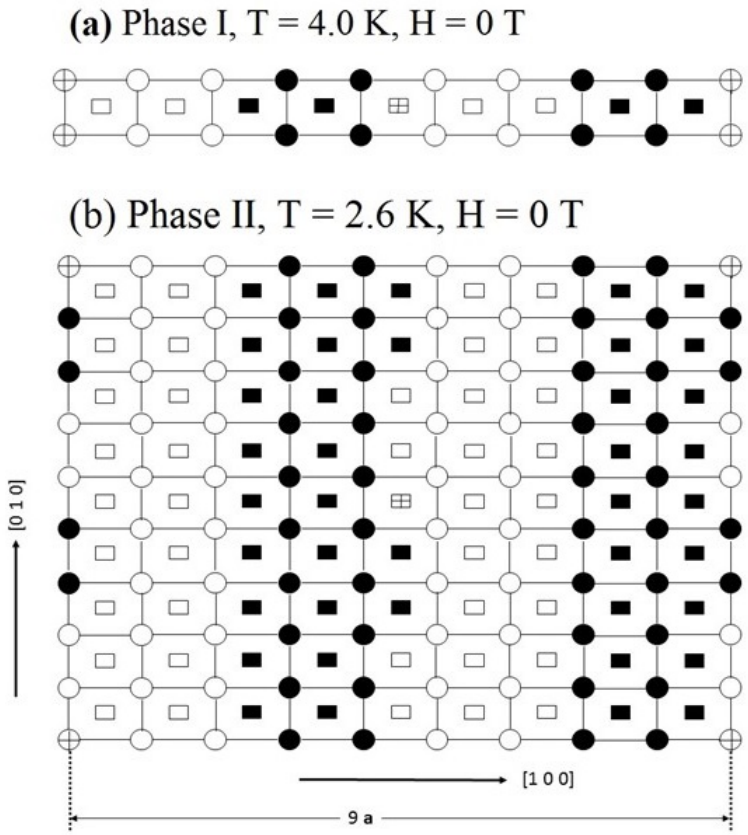

Figure 5.3: (a) One-dimensional modulation for the phase at $T_t < T < T_N$, and (b) two-dimensional modulation for $T < T_t$, projected on to the c - plane. Open (closed) symbols represent Dy spins parallel (anti-parallel) to the c – axis. Symbols with cross (+) marks inside represent frustrated paramagnetic Dy ions. Each parallelogram represents a chemical unit cell. These models are reproduced based on those developed by Kawano et al. [144, 145].

According to the model proposed by Kawano et al. [144, 145], the HTP has a one dimensional spin arrangement, described by the sequence $04\bar{4}04\bar{4}$ as shown in Fig. 5.3 (a). Here, $4(\bar{4})$ represents (200)/(100) planes with Dy moments up (down) to the c-axis, and 0 represents a paramagnetic (PM) plane. In the ITP, the system has a two dimensional magnetic unit cell of $9a \times 9a \times 9c$, where a and c represent the lattice constants of the chemical unit cell (Fig. 5.3 (b)). In this phase, the spin arrangement is given by $\circ 4\bar{4} \bullet 4\bar{4}$, which means that, for every ninth ferromagnetic (200) or (100) plane, there will be an antiferromagnetic (200) or (100) plane. In light of this model, the system transforms from a one dimensional magnetic structure to a two dimensional structure at T_t upon cooling, giving rise to a high magnetization phase that is evident from the peak in the magnetization around T_t (see Fig. 5.2). The origin of the thermal hysteresis in the M vs. T data may be the order-order transition between the two-dimensional and one-dimensional magnetic configurations.

Fig. 5.4 shows an Arrott plot analysis of the magnetization isotherms at atmospheric

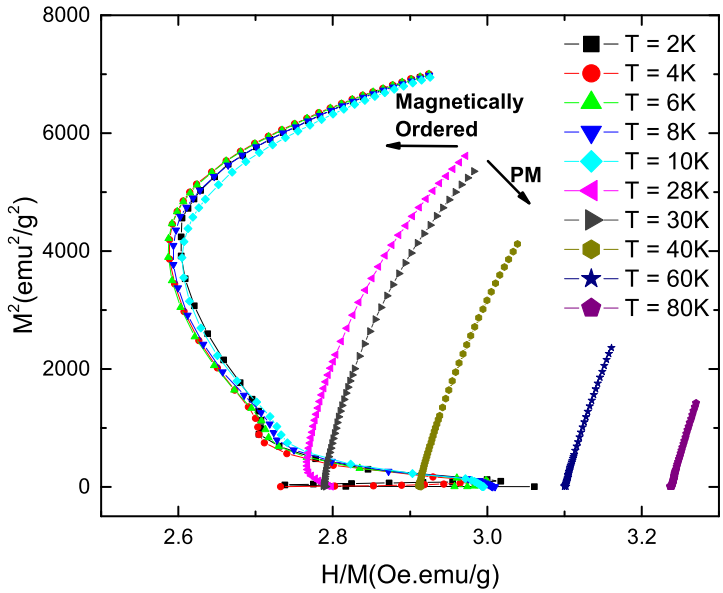

Figure 5.4: Arrott plots of the magnetization $[M(H)]$ data for $DyRu_2Si_2$ (M^2 vs. H/M) at selected temperatures and at atmospheric pressure.

pressure for some selected temperatures around T_t and T_N. It is known from the Banerjee criterion [103] that a negative slope in the Arrott plot is an indication of a first-order magnetic transition, whereas a positive slope indicates a second-order transition. The curves around T_t formed "S" like shapes with negative slopes at lower field values and positive slopes at higher fields. This occurrence of a negative curvature in Arrott plots is usually associated with a first-order magnetic transition [143, 149–153]. The small temperature hysteresis in the M vs. T data also points towards the first-order nature of the transition at T_t. Curves showing negative slopes continue up to the Néel temperature (T_N) and, starting from $T = 30$ K, they start to have positive slopes even at low fields. At higher temperatures no negative slopes were observed, implying a second-order transition to a PM state.

We also constructed a universal curve for the entropy change at atmospheric pressure (not shown), in light of the works by Franco et al. [154]. For materials showing second-order magnetic transitions, the ΔS vs. T curves measured at different fields should collapse into a single curve, whereas a failure to collapse is considered to be an indication of a first-order transition [154, 155]. In our case, the curves collapsed into a single universal curve around T_N. However, below T_N, and around T_t, the curves failed to collapse. This could be construed as an indication of a first-order transition. However, this view was challenged by Smith et al., [156] arguing that there was no one-to-one connection between the behavior of the scaling procedure and the order of the phase transition. Based on these findings, and especially the observed thermal hysteresis, it is plausible that the magnetic phase transition at T_t is not purely second-order.

Fig. 5.5 shows the magnetization isotherms measured at 2 K at various pressures. In increasing field, three distinct transitions were observed with critical fields of $H_1 = 0.2$ T, $H_2 = 1.2$ T, and $H_3 = 2.2$ T, consistent with previous reports [146]. For intermediate pressures of $P = 0.588$ and 0.654 GPa, the transitions at $H > 0.2$ T were suppressed (barely discernible in the data). At a higher pressure of 0.934 GPa these phases return and, at

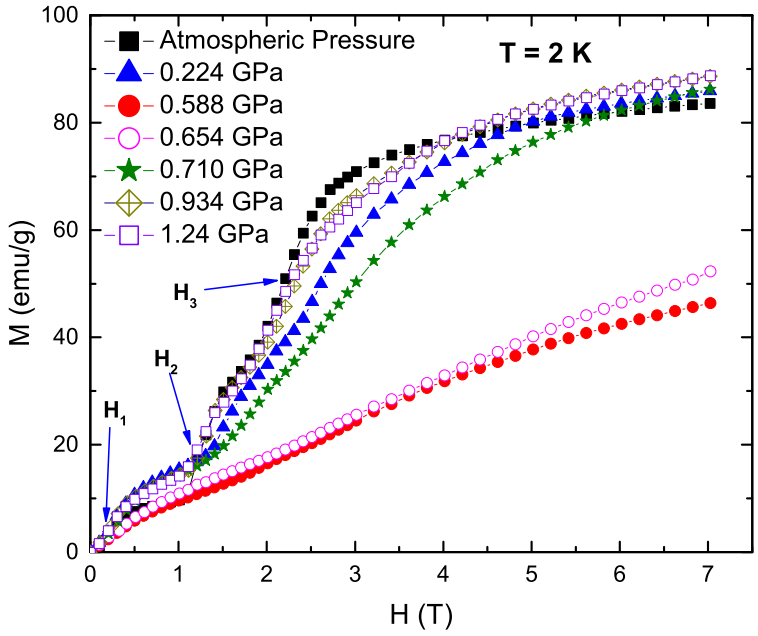

Figure 5.5: Magnetization (M) vs. magnetic field (H) for $DyRu_2Si_2$ at $T = 2$ K for various applied hydrostatic pressures.

the highest pressure of 1.24 GPa, they have nearly the same critical fields as they had had at atmospheric pressure. Moreover, at atmospheric pressure, although the M vs. H curve does not fully saturate even at 7 T, a saturation tendency could be seen around $H = 3$ T. For pressures of $P = 0.588$ and 0.654 GPa, this saturation tendency was not observed, and the curves follow a nearly linear dependence on increasing field, pointing towards a weaker magnetic ordering. Also, the magnetization values at $H = 7$ T for $P = 0.588$ and 0.654 GPa are considerably smaller than those at atmospheric pressure. This saturation tendency and non-linearity return at 0.934 GPa, and continue up to 1.24 GPa, but the magnetization starts to saturate at a higher field value than that observed at atmospheric pressure. Moreover, the magnetization at $H = 7$ T is larger for $P = 1.24$ GPa than at atmospheric pressure.

Heavy rare-earth elements, such as pure Dy and materials consisting of rare-earth elements, often show magnetostriction [157–159], which led us to explore the magnetostrictive

properties of this compound. Using the Maxwell relation

$$\left(\frac{\partial M}{\partial P}\right)_{H,T} = -\left(\frac{\partial V}{\partial H}\right)_{P,T}, \tag{5.1}$$

we calculated the volume magnetostriction, $\Delta V/V$, where V is the volume of the unit cell calculated from the lattice parameters obtained from the XRD measurements. In Eq. 5.1, M is the magnetization, P is the applied pressure, V is the volume, and H is the applied magnetic field. This method was also applied by S.A. Nikitin et al. [158, 159] to estimate the volume magnetostriction in single crystals of Dy and Y_2Fe_{17}.

Fig. 5.6 shows the temperature dependence of the volume magnetostriction at various pressures. At low fields, a peak in the volume magnetostriction was observed around $T_N \approx$

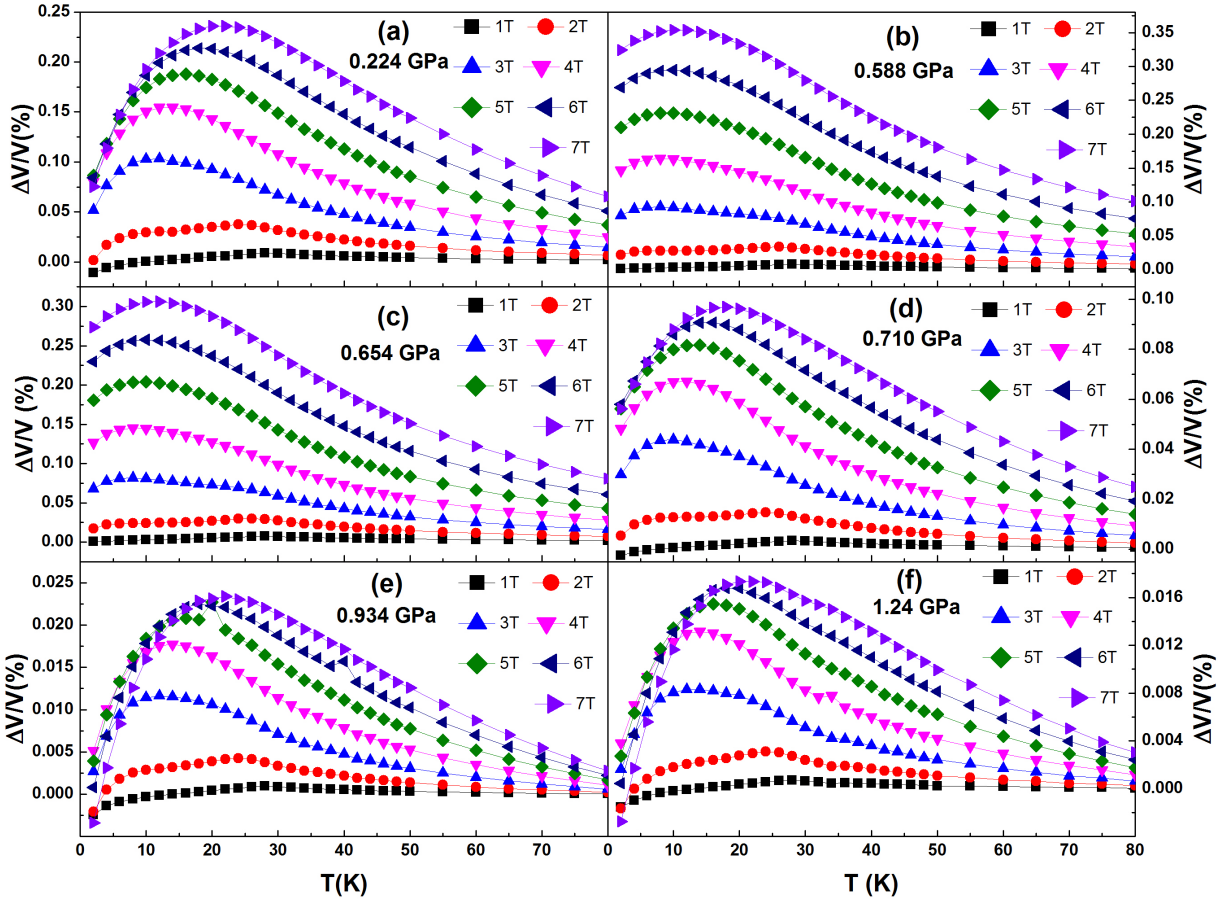

Figure 5.6: (a) - (f) Temperature (T) dependence of the volume magnetostriction ($\Delta V/V$) of $DyRu_2Si_2$ at magnetic fields up to 7 T for various pressures (P).

29 K (not shown). This is consistent with the observation that the onset of magnetic ordering gives rise to magnetostriction in heavy rare earth metals, as reported by Nikitin et al. [160]. As the magnetic field increases, the magnitude of the volume magnetostriction increases, and the peak in the $\Delta V/V$ vs. T curves shifts towards higher temperatures. The highest value of the volume magnetostriction was found to be 0.35% at $H = 7$ T and at $P = 0.588$ GPa. A volume magnetostriction of 0.7×10^{-3} at a field of 1.2 T was reported for a pure Dy single crystal [158], whereas the value calculated here for $DyRu_2Si_2$ is 0.1×10^{-3} for the same magnetic field. For pressures $P > 0.588$ GPa, the volume magnetostriction decreased systematically, as shown in Fig. 5.7 (a).

The presence of magnetostriction in this compound can be attributed to the decrease in magnetization due to applied hydrostatic pressure. This kind of pressure dependent behavior has been observed in invar alloys, heavy rare-earth elements such as Tb, Gd, Dy, Tb-Gd alloys, and others [161, 162]. According to Eq. 5.1, sharp changes in magnetization with pressure result in volume changes. We observed large changes in the magnetic behavior

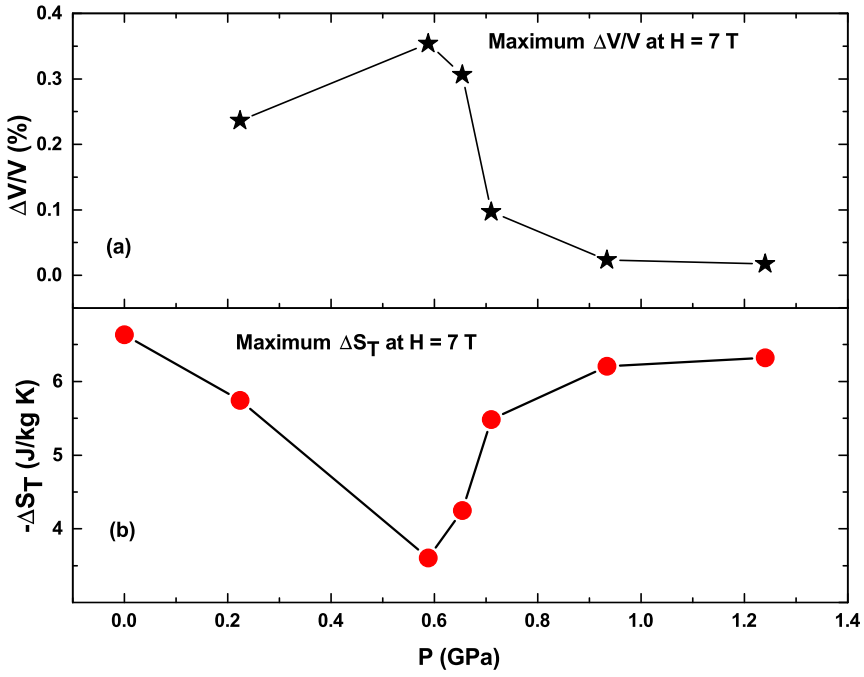

Figure 5.7: (a) The maximum values of $\Delta V/V$ at $H = 7$ T for $DyRu_2Si_2$ at various applied pressures. (b) The maximum values of ΔS_T at $H = 7$ T for various applied pressures.

of $DyRu_2Si_2$ at pressures $P = 0.588$ and 0.654 GPa (relative to that at atmospheric pressure) which translated to volume changes as expected from the Maxwell relation (Eq. 5.1). As pointed out by Doerr et al., crystal field and exchange striction are the two most important mechanisms for magnetostriction in rare-earth systems [157]. Tomala et al. [163] studied the crystal field properties of $DyRu_2Si_2$ by Mössbauer spectroscopy and calculated the crystal electric field (CEF) parameters, B_2^0 with an anomalously large value of -4.94 K. With the application of pressure, both the crystal electric field environment and the exchange interactions can change. However, identifying the mechanism that plays the dominant role in the magntostriction requires further investigation involving single crystals.

The total entropy change (ΔS_T) was calculated from the magnetization isotherms using the integrated Maxwell relation

$$\Delta S_T(T) = \int_0^{H'} \left(\frac{\partial M}{\partial T}\right)_H dH. \tag{5.2}$$

Fig. 5.8 shows the temperature dependence of ΔS_T for fields up to 7 T at various pressures. At atmospheric pressure, peaks were observed around T_N, and the highest value of ΔS_T was -6.64 J/kg K at $T = 29$ K for $\Delta H = 7$ T.

An inverse MCE ($\Delta S_T = +2.15$ J/kg K) was also observed at $T = 3$ K for $\Delta H = 7$ T, at atmospheric pressure. As the temperature increases beyond 3 K, the inverse MCE vanishes and a normal (i.e., negative) MCE emerges. For the 1 T curve at atmospheric pressure (Fig. 5.8(a)), the inverse (positive) MCE starts at 5 K and continues up to 27 K. This inverse MCE is associated with the low-temperature AFM phase. Subtle but clear signs of the transition at T_t were also evident, especially at lower fields. The value of ΔS_T decreased at an applied pressure of 0.588 GPa (Fig. 5.8(c)) and, in this case, two distinct peaks were observed, one at 5 K (around T_t) and the other at 31 K (around T_N) with ΔS_T values of -3.60 and -2.4 J/kg K, respectively. It was noted that, at this pressure, the largest value of ΔS_T was found near T_t rather than at T_N. This scenario prevails at $P = 0.654$

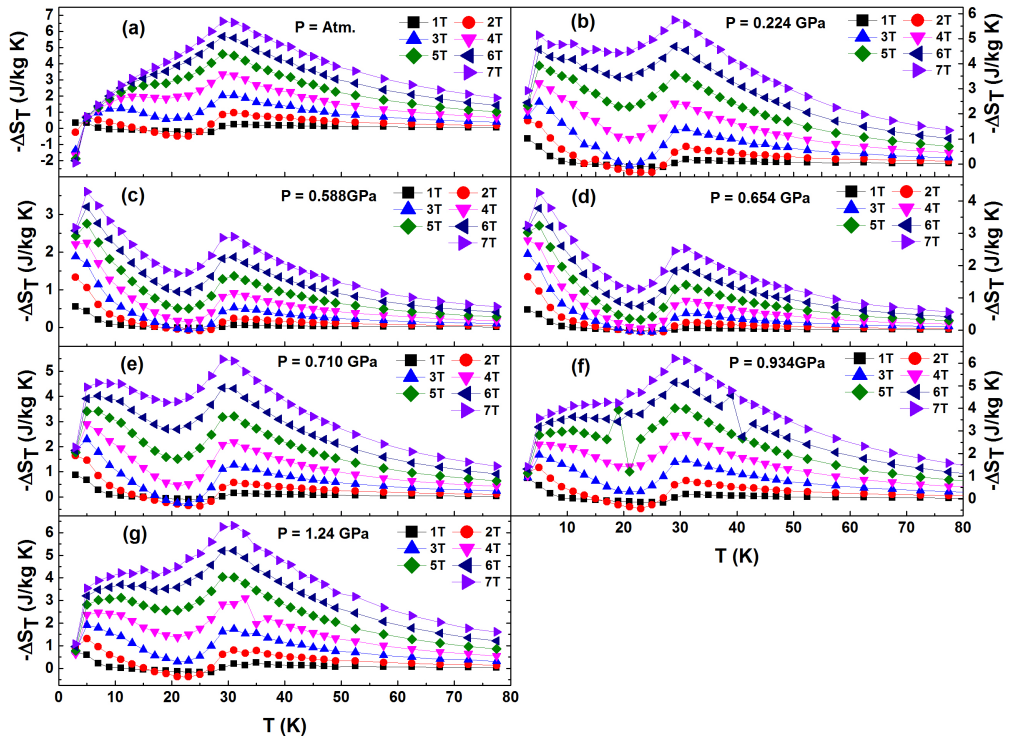

Figure 5.8: (a) - (g) Temperature (T) dependence of the total entropy change (ΔS_T) of $DyRu_2Si_2$ for various applied magnetic fields (H) and pressures (P).

GPa but, at P = 0.710 GPa, the largest value of ΔS_T was again observed at T_N. This trend continues up to the highest applied pressure of 1.24 GPa.

After the initial decrease in the overall values of ΔS_T for applied pressures of 0.588 GPa and 0.654 GPa, the values start to increase at pressures exceeding 0.710 GPa. At P = 1.24 GPa (Fig. 5.8(g)), the peak value of -6.32 J/kg K at H = 7 T is very close to the atmospheric pressure value of -6.64 J/kg K (Fig. 5.7 (b)). Moreover, the overall shape and features of the curves at P = 1.24 GPa are similar to those at atmospheric pressure. This tendency was also observed in the M vs. H curves at different pressures (Fig. 5.5).

The origin of this pressure-dependent behavior may lie with the change in the a/c ratio with pressure. As pointed out by A. Szytula et al. [141], in RT_2X_2 systems the magnetic interaction is governed by an RKKY model and the a/c ratio plays a crucial role in defining the nature and strength of the interaction. In RT_2X_2 systems containing heavy rare earths (R= Tb - Tm), a simple collinear AFM structure was observed when $a/c < 0.415$

and oscillatory magnetic structures emerge when $a/c > 0.415$. At atmospheric pressure, $DyRu_2Si_2$ has an a/c ratio of 0.435, well above the critical value of 0.415. At pressures of 0.588 and 0.654 GPa, the M vs. H (Fig. 5.5) data at $T = 2$ K point toward a simpler AFM structure than that which occurs at atmospheric pressure. But for $P > 0.710$ GPa, the curves again resemble those measured at atmospheric pressure. From this fact, and from Fig. 5.5, it is plausible that, at pressures between 0.588 and 0.654 GPa, the system favors a simpler AFM-like interaction, while at atmospheric pressure and at pressures greater than 0.654 GPa, the system tends towards more complicated interactions. Also, the exchange integral depends on the interatomic distances [161]. The change in volume, and hence the interatomic distances, due to applied pressure can affect the exchange integral, resulting in a variation of magnetic interactions. The observed variation in magnetic properties with pressure can possibly be attributed to the oscillatory nature of the RKKY interaction.

As there is a volume anomaly due to magnetostriction, the total field-induced entropy change is a sum of the magnetic and structural entropy changes, [104, 105] i.e.,

$$\Delta S_T = \Delta S_{mag} + \Delta S_{str}. \tag{5.3}$$

Gschneidner et al. [105] compiled a collection of ΔS_{str} (i.e, structural contribution to the total entropy change) for different materials undergoing magnetostructural transitions, as well as volume anomalies, and found a linear relationship between ΔS_{str} and $\Delta V/V$. In light of this, we can use the relationship $\delta[\Delta V/V(\%)]/\delta[\Delta S_{str}] = 0.08\,(\mathrm{J/kg\,K})^{-1}$ to estimate the structural contribution to the total entropy change [164, 165]. According to this relation, our observed volume magnetostriction of 0.35 % at $H = 7$ T and $P = 0.588$ GPa corresponds to a structural entropy change of $\Delta S_{str} = 4.375$ J/kg K.

In Fig. 5.7, it can be seen that, as the pressure increases, the volume magnetostriction $\Delta V/V$, and therefore ΔS_{str}, decrease, whereas the value of the total entropy change (ΔS_T) increases. This may indicate that the structural entropy change (ΔS_{str}) opposes

the magnetic entropy change (ΔS_{mag}), thereby reducing ΔS_T.

From the zero-field heat capacity measurements at atmospheric pressure (Fig. 5.9), a well defined anomaly was observed starting at $T = 28.3$ K and ending at $T = 29.3$ K with a drop of about 11.8 J/kg K during heating, which is a characteristic of magnetic ordering. No clear signature of an anomaly was observed in the C(T) data around $T_t = 3.4$ K, probably due to low resolution in that temperature range. However, sharp spikes in the C/T vs. T plot as shown in Fig. 5.9(b) were observed around $T = 2$ K and 29 K.

By integrating the C/T data for $H = 0$ T and 5 T, the entropy at these two fields, $S(0\,\mathrm{T})$ and $S(5\,\mathrm{T})$, were calculated and subtracted to get $\Delta S = S(5\,\mathrm{T}) - \mathrm{S}(0\,\mathrm{T})$, as shown in Fig. 5.10(b). A peak value of -5.5 J/kg K was found at $T_N = 29.3$ K which is the Néel temperature, while a value of -4.6 J/kg K was found from the atmospheric pressure magnetization data for an applied field of 5 T. These numbers are in reasonable agreement. To calculate the adiabatic temperature change (ΔT_{ad}), $S(0\,\mathrm{T})$ and $S(5\,\mathrm{T})$ were first inter-

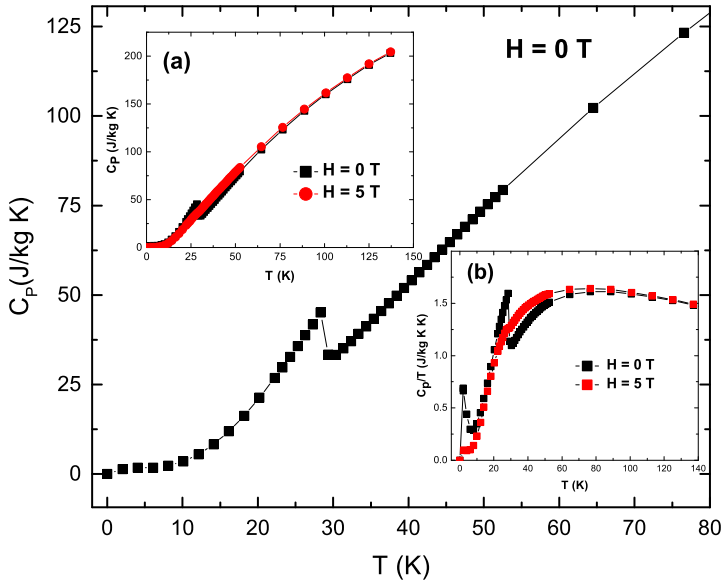

Figure 5.9: Temperature (T) dependence of the heat capacity (C_p) of $DyRu_2Si_2$ measured at atmospheric pressure and zero applied magnetic field. (a) Heat capacity (C_p) measured at $H = 0$ T and 5 T. (b) C_p/T vs. T at $H = 0$ T and 5 T.

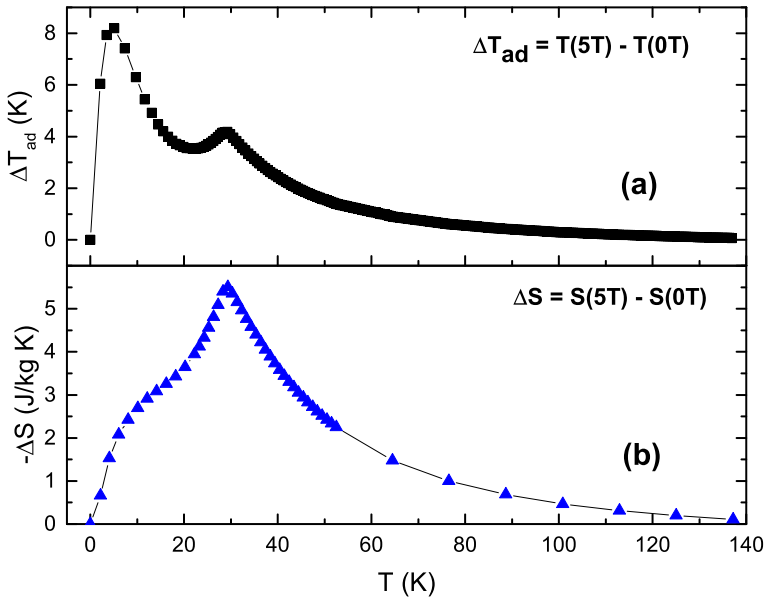

Figure 5.10: (a) Temperature (T) dependence of the adiabatic temperature change (ΔT_{ad}) of $DyRu_2Si_2$. (b) Temperature (T) dependence of the total entropy change (ΔS_T) calculated from the heat capacity data.

polated from the S vs. T plots. T vs. S plots were then plotted with the interpolated S data for 0 and 5 T magnetic fields and, after interpolating $T(0\,\mathrm{T})$ and $T(5\,\mathrm{T})$, ΔT_{ad} was calculated using the relation $\Delta T_{ad} = T(5\,\mathrm{T}) - \mathrm{T}(0\,\mathrm{T})$. Fig. 5.10(a) shows the adiabatic temperature change ΔT_{ad}, and a peak value of 8.2 K was observed at $T = 5.1$ K, which is near the transition temperature T_t. A second peak of magnitude 4.2 K was observed at $T = 29.2$ K (T_N).

5.4 Conclusions

Pressure-dependent magnetization measurements have been carried out on $DyRu_2Si_2$, from which we have estimated the volume magnetostriction and entropy changes (ΔS_T) as a function of hydrostatic pressure. We observed multi-step meta-magnetic transitions in the $M(H)$ curves at atmospheric pressure, the features of which diminished at intermediate pressures ($P = 0.588$ GPa and 0.654 GPa) and reappeared at higher pressures ($P \approx 1$ GPa). Moreover, the saturation magnetization decreased at intermediate pressures, fol-

lowing a near-linear dependence on increasing field, indicating a weaker magnetic ordering. At higher pressures, the saturation magnetization increased again and the $M(H)$ curves resembled those measured at atmospheric pressure. This trend of pressure dependence was also observed in the ΔS_T vs. T curves measured at various pressures. At intermediate pressures, the entropy changes (ΔS_T) decreased, whereas these values gradually increased with higher applied pressures. The variation of the magnetic properties with pressure is likely connected to the modulation of the exchange integral (RKKY-type behavior), caused by a change in interatomic distances due to applied hydrostatic pressure.

In the next chapter, we will discuss the magnetic interactions in a Heusler alloy system, where the magnetism is governed by the RKKY exchange interactions. Through analyzing the critical behavior in this system, we will shed light into the evolution of the magnetic interactions due to a particular substitution strategy.

Chapter 6
Critical Behavior in Ni_2MnGa and $Ni_2Mn_{0.85}Cu_{0.15}Ga$

6.1 Introduction

One of the most extensively studied materials in the Heusler alloy family is the Ni_2MnGa system. This compound shows a wide variety of properties, such as magnetic field induced strain (MFIS) [166], giant magnetocaloric effects (MCE) [41], etc., making it attractive from both technological and scientific points of view. Ni_2MnGa undergoes two transitions upon cooling: first is a second-order magnetic (order - disorder) transition at $T_C \approx 382$ K from a cubic ($L2_1$) paramagnetic (PM) phase to a cubic ferromagnetic (FM) phase. Secondly, it undergoes a structural (martensitic) transition from a cubic FM phase (austenite) to a complex FM tetragonal (martensitic) phase at $T_M \approx 209$ K. There is also a premartensitic transition at $T_p \approx 260$ K, which is due to a modulation in the austenitic phase [167, 168].

It has been observed that, in Heusler alloys, various substitution schemes and variations in stoichiometry can significantly modify the magnetic interactions. A critical exponent analysis can provide insight into the range of the exchange interactions as well as the lattice and spin dimensionalities. This is also useful in understanding the role of a particular substitution scheme or stioichiometry variation in modifying the magnetic interactions. Not surprisingly, this approach has been widely used by researchers to investigate the second-order phase transition in Heusler Alloys (see Refs. [169–173]). Some examples may be helpful in elucidating the scope of the critical exponent analysis. For instance, through critical exponent analysis of $Ni_{50}Mn_{50-x}Sn_x$, Phan et al. (Ref. [169]) argued that the Sn substitution drove the system from short-range to long-range FM order. In another study, it was revealed that Gd substitution for Ni in $Ni_{50}Mn_{37}Sn_{13}$, drove the system from short-range FM order to long-range order [170]. In a similar manner, the role of various substitution schemes in $Ni_{47}Mn_{40}Sn_{13-x}Cu_x$, $Ni_{43}Mn_{46}Sn_8X_3$ (x = In and Cr), $Ni_{2.2}Mn_{0.72-x}V_xGa_{1.08}$,

Reproduced from [Ahmad Us Saleheen, Jing-Han Chen, David P. Young, Igor Dubenko, Naushad Ali, and Shane Stadler, *Journal of Applied Physics* **123(20)**, 203904 (2018)], with the permission of AIP Publishing (see Appendix A).

$TbCo_{2-x}Fe_x$, and so on, were investigated through critical exponent analysis [171–174].

In $Ni_2Mn_{1-x}Cu_xGa$, increasing the Cu concentration drives the two transitions (T_C and T_M) towards each other and, when x = 0.25, the two transitions coincide at $T = 308$ K [41]. A large MCE (magnetic entropy change) has been reported for $Ni_2Mn_{0.75}Cu_{0.25}Ga$ at this coupled magnetostructural transition [41, 175]. Over the years, experimental and theoretical investigations were carried out to better understand the mechanism behind the shift of the transition temperatures, i.e., the role of dopants, etc. [167, 175–178]. S. Roy et al. investigated the role of Cu substitution in the $Ni_2Mn_{1-x}Cu_xGa$ compound using X-ray absorption spectroscopy and X-ray magnetic circular dichroism [175]. They showed that the substitution of Cu enhances the Ni - Ga hybridization and shifts the martensitic transition temperature (T_M) to higher temperature. Moreover, the magnetic ordering (Curie) temperature (T_C) decreases as the Mn concentration is reduced and the system becomes more magnetically delocalized. In Ni_2MnGa, long-range Ruderman-Kittel-Kasuya-Yosida (RKKY) exchange interaction between Mn atoms, mediated by the Ni atoms, is responsible for the ferromagnetism [179]. As pointed out previously (Ref. [175]), the substitution of non-magnetic Cu in the Mn site significantly modifies the magnetic properties of the system. This motivated us to conduct a critical exponents analysis for these compounds.

In this investigation, the critical behaviors near the second-order phase transitions in polycrystalline Ni_2MnGa and $Ni_2Mn_{0.85}Cu_{0.15}Ga$ have been examined. Bulk magnetization measurements were used to obtain the critical exponents, β, γ, and δ, for each system. The range of exchange interactions, lattice and spin dimensionalities, and the overall modification of the magnetic interactions due to the Cu substitution will be discussed through the critical exponents.

6.2 Theoretical Background

The critical behavior of a magnetic material undergoing a second-order (continuous) phase transition can be characterized by a set of critical exponents in the vicinity of the Curie temperature (T_C). Materials with the same critical exponents belong to the same uni-

versality class, manifesting a universal behavior around the critical region. These critical exponents depend only on the dimension of the lattice (d), order parameter (n), and the range of exchange interactions [180–182]. In the critical region near T_C, various thermodynamic quantities show power-law dependencies on the reduced temperature, $\epsilon = (T - T_C)/T_C$. The spontaneous magnetization [$M_S \equiv M_{H=0}$], initial susceptibility [$\chi_0 \equiv \frac{\partial M}{\partial H}\big|_{H=0}$], and the critical isotherm [$M(H)_{T=T_C}$] are respectively given by the following equations:

$$M_S(T) = M_0(-\epsilon)^{\beta} \quad (\epsilon < 0) \tag{6.1}$$

$$\chi_0^{-1} = \Gamma(\epsilon)^{\gamma} \quad (\epsilon > 0) \tag{6.2}$$

$$M = XH^{(1/\delta)} \quad (\epsilon = 0) \tag{6.3}$$

where, M_0, Γ, and X are the critical amplitudes [181, 183, 184]. According to the scaling hypothesis [181, 182, 185, 186], various formulations of a magnetic equation of state can be expressed as

$$m = f_{\pm}(h) \tag{6.4}$$

$$H = M^{\delta} h(x) \tag{6.5}$$

$$h/m = \pm a_{\pm} + b_{\pm} m^2, \tag{6.6}$$

where $m \equiv |\epsilon|^{-\beta} M(H, \epsilon)$ is the renormalized magnetization, $h \equiv |\epsilon|^{-(\beta\,\delta)} H$ is the renormalized field, and $x \equiv \epsilon M^{-1/\beta}$. In eq. (6.4), the terms f_+ for $T > T_C$ and f_- for $T < T_C$ are unspecified scaling functions [185]. According to eq. (6.4), a plot of m vs. h should collapse into two universal curves, one above and one below T_C for the correct values of the critical exponents. This feature can be used to obtain the critical exponents of a magnetic system. However, a more accurate approach is to use the Arrott - Noakes equation of state [181], which is given by

$$(H/M)^{(1/\gamma)} = A\epsilon + BM^{(1/\beta)} \tag{6.7}$$

and the plot of $M^{1/\beta}$ vs. $(H/M)^{1/\gamma}$, which is known as the modified Arrott plot (MAP). For the right choices of β and γ, this plot consists of a series of parallel straight lines with the isotherm at $T = T_C$ passing through the origin. From the intercepts on the vertical and horizontal axes, the spontaneous magnetization $M_S(T)$ and the initial susceptibility $\chi_0^{-1}(T)$ can be calculated, respectively. Once the intercepts are obtained, eqs. (6.1) and (6.2) can be used to find the values of the critical exponents, β and γ.

6.3 Experimental Methods

Pollycrystalline Ni_2MnGa and $Ni_2Mn_{0.85}Cu_{0.15}Ga$ ingots (approximately 5 g) were fabricated from the high-purity elements (better than 99.9%) Ni, Mn, Cu, and Ga in an induction furnace under a high purity argon atmosphere. The weight loss after melting was found to be less than 0.1 %. The samples were placed inside an evacuated quartz tube and annealed at 850 °C in a tube furnace for 3 days and slowly cooled to room temperature. X-ray diffraction (XRD) measurements were done with a room-temperature X-ray diffractometer using Cu Kα radiation and θ - θ geometry. Magnetic measurements were carried out using a superconducting quantum interference device magnetometer (SQUID-MPMS by Quantum Design). Temperature dependent magnetization measurements, $M(T)$, were performed in a temperature interval of 10 - 400 K. The magnetization isotherms, $M(H)$, were measured in the vicinity of the Curie temperatures (T_C) in temperature increments of $\Delta T = 0.5$ K. At each temperature set point, a 5 minute wait time was imposed for better temperature stabilization. The magnetic field was applied in increments of $\Delta H = 0.25$ T up to $H = 7$ T in no-overshoot mode.

6.4 Results: Critical Behavior in Ni_2MnGa

From the temperature dependent magnetization measurement for Ni_2MnGa shown in Fig. 6.1(a), the initial value of T_C was calculated as the minimum of the dM/dT vs. T curve (not shown). The $M(H)$ curves (isotherms) were obtained in $\Delta T = 0.5$ K increments in the critical region as shown in Fig. 6.1(b). These data were rescaled according to eq. (6.7) by adjusting β and γ. For $\beta = 0.5$ and $\gamma = 1$, the $M^{1/\beta}$ vs. $(H/M)^{1/\gamma}$ plot is just

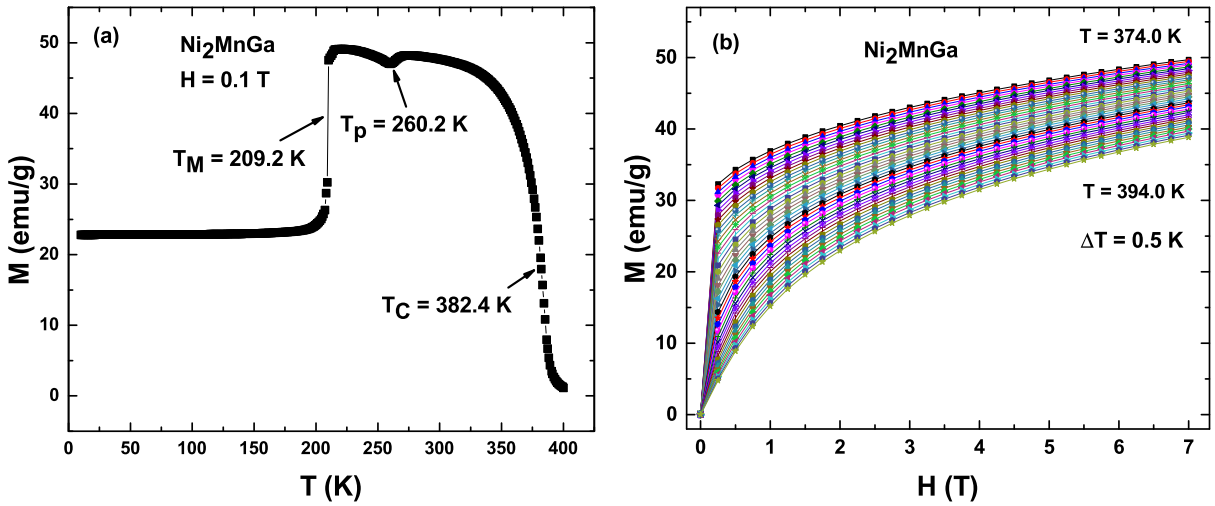

Figure 6.1: (a) Magnetization (M) vs. temperature (T) for Ni_2MnGa measured in an applied field of $H = 0.1$ T. T_M, T_p, and T_C represent the martensitic, pre-martensitic, and Curie temperatures, respectively. (b) Magnetization isotherms, $M(H)$, measured in increments of $\Delta T = 0.5$ K.

the conventional Arrott plot (see Fig. 6.2(a)). Two things can be observed immediately from the Arrott plot: first, the non-linearity of the isotherms indicates that the mean-field theories may not be best suited to describe the critical behavior in this system and, second, the absence of negative slopes throughout the entire range of fields indicates that the transition from the ferromagnetic (FM) to paramagnetic (PM) phase is a second-order transition, consistent with the Banerjee criterion [103].

Known values of the critical exponents for various universality classes, such as 3D - Heisenberg, 3D - Ising, 3D - XY, etc., were used to construct corresponding modified Arrott plots (MAPs). The isotherms in the MAP constructed with the critical exponents of the 3D - Heisenberg class exhibited the most linear behavior compared to the MAPs constructed with other exponents. Therefore, theoretical values of the critical exponents for the 3D - Heisenberg model [181, 187] ($\beta = 0.365, \gamma = 1.336$) were taken as the initial trial values to construct an initial MAP similar to that in Fig. 6.2(b). The isotherms were extrapolated from high field linear regions to find the intercepts of the $M^{1/\beta}$ and $(H/M)^{1/\gamma} = (\chi_0^{-1})^{(1/\gamma)}$ axes to calculate the values of $M_S(T)$ and χ_0^{-1} shown in Fig. 6.3(a). From these values of

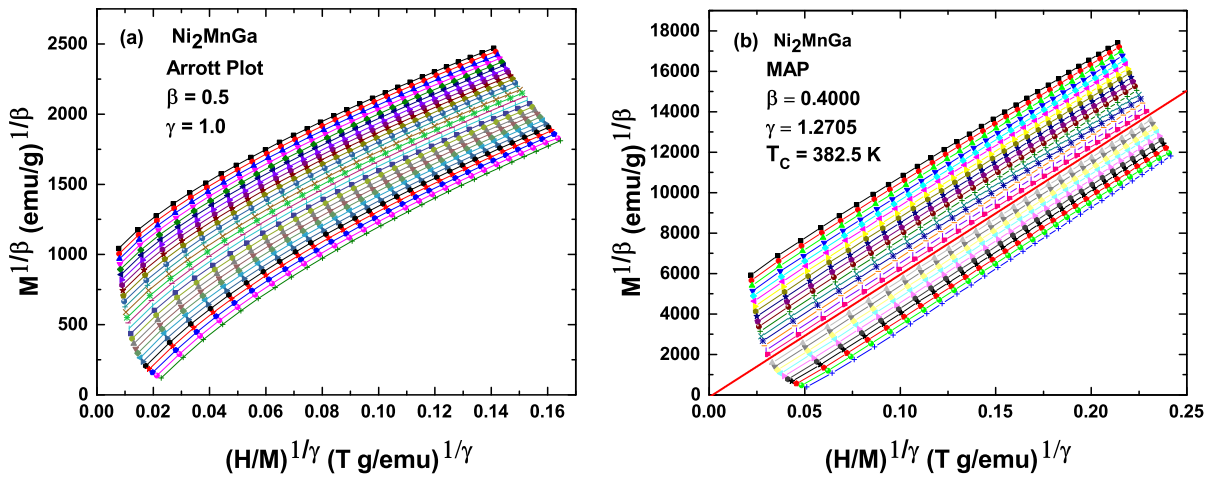

Figure 6.2: (a) Arrott Plot of magnetization isotherms measured in the temperature range of T = 374.0 - 388.0 K with ΔT = 0.50 K for Ni_2MnGa. (b) Modified Arrott plot (MAP) using $\beta = 0.4000$ and $\gamma = 1.2705$. The solid red line indicates the linear fit to the isotherm at T_C = 382.5 K.

$M_S(T)$ and χ_0^{-1}, a new set of critical exponents β and γ were calculated using the Kouvel - Fisher method [188]. This is considered to be the most reliable method in extracting accurate values of the critical exponents based on MAPs [181, 183, 186]. According to this method, eqs. (6.1) and (6.2) can be written as

$$M_S(T)\left[\frac{dM_S(T)}{dT}\right]^{-1} = (T - T_C)/\beta \tag{6.8}$$

$$\chi_0^{-1}\left[\frac{d\chi_0^{-1}(T)}{dT}\right]^{-1} = (T - T_C)/\gamma. \tag{6.9}$$

The plots of $M_S(T)[dM_S(T)/dT]^{-1}$ vs. T and $\chi_0^{-1}[d\chi_0^{-1}(T)/dT]^{-1}$ vs. T are straight lines with slopes of $1/\beta$ and $1/\gamma$, respectively, as shown in Fig. 6.3(b). Next, the values of β and γ found from the Kouvel - Fisher plot were used to generate a new MAP. This process was iterated until the values converged, and a stable set of critical exponents (β, γ) and T_C were obtained. For Ni_2MnGa, after multiple iterations, the critical exponents converged to the following values: $\beta = 0.401 \pm 0.003$, $\gamma = 1.27 \pm 0.02$, and $T_C = 382.42$ K $\pm$ 5.13 K (see Table 6.1). One notable feature of the Kouvel - Fisher method is that,

unlike other methods, no prior knowledge of T_C is required, as the intercept of the straight lines with the temperature axis gives T_C [181, 186].

A ln - ln plot of some representative isotherms in the vicinity of T_C are shown in Fig. 6.4. According to eq. (6.3), a $ln(M)$ vs. $ln(H)$ plot for the critical isotherm should be a straight line with a slope of $1/\delta$. For Ni_2MnGa, the isotherm at $T = 382.5$ K was considered to be the critical isotherm as it was closest to $T_C = 382.42$ K. The exponent $\delta = 4.10$ was calculated by performing a linear fit to the critical isotherm. The β and γ values obtained through the Kouvel - Fisher method can be used to calculate δ by using the Widom relation [182, 189]

$$\delta = 1 + \frac{\gamma}{\beta}. \tag{6.10}$$

This relation yielded $\delta = 4.17 \pm 0.08$, which is very close to the value $\delta = 4.100 \pm 0.007$ obtained from the critical isotherm (see Table 6.1). The values of δ obtained from the two independent methods (Kouvel - Fisher and critical isotherm) are in reasonable agreement, indicating the reliability of the β and γ values.

As discussed in the previous section, according to eq. (6.4), a plot of the reduced

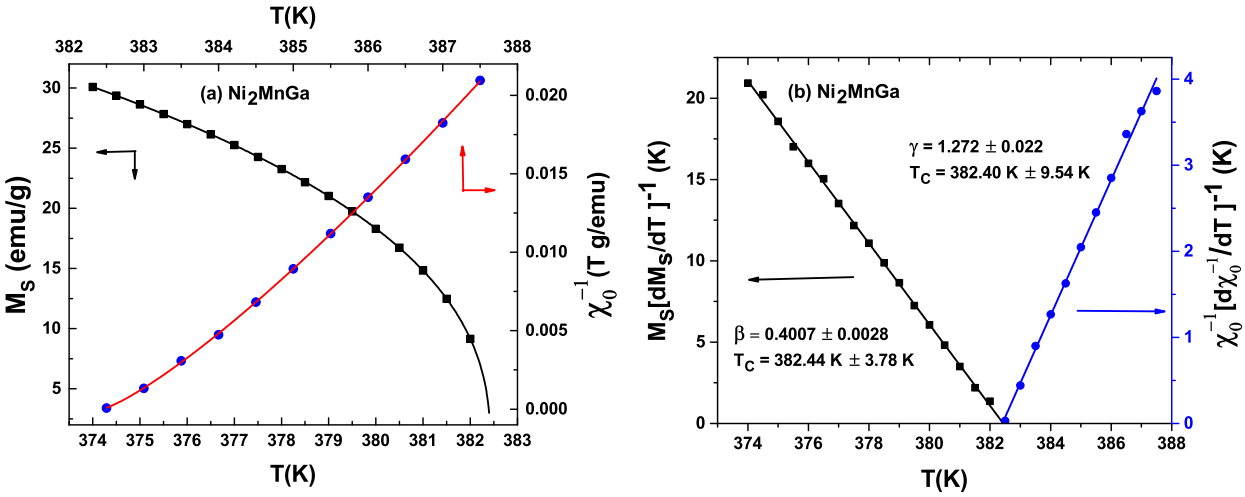

Figure 6.3: (a) Temperature dependence of the spontaneous magnetization $[M_S(T, 0)]$ and inverse susceptibility $[\chi_0^{-1}]$ obtained from the linear extrapolation of the MAP of Fig. 6.2(b). The lines represent best fits to eqs. (6.1) and (6.2). (b) Kouvel-Fisher plots for Ni_2MnGa. Straight lines are linear fits to the data, from which β, γ, and T_C were calculated.

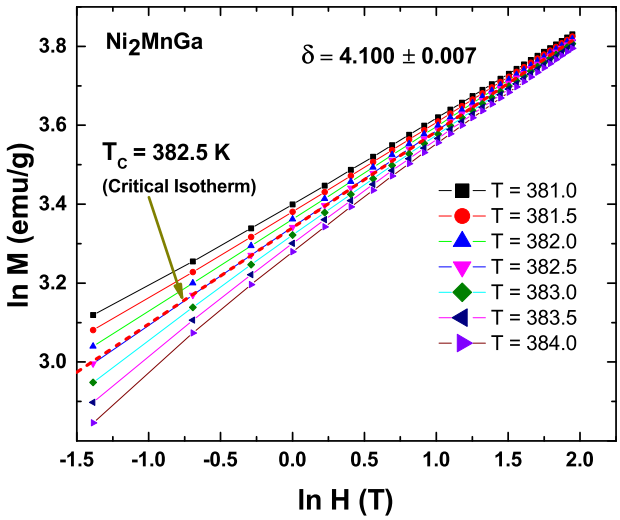

Figure 6.4: A plot of $ln(M)$ vs. $ln(H)$ near the critical isotherm for Ni_2MnGa. The dashed red line represents the linear fit to the critical isotherm at $T_C = 382.5$ K; δ was calculated from the slope of this line.

magnetization ($m \equiv |\epsilon|^{-\beta} M(H, \epsilon)$ vs. reduced field ($h \equiv |\epsilon|^{-(\beta+\gamma)} H$) should collapse into two separate branches, one above and one below T_C, for the correct choice of critical exponents. This behavior is seen in Fig. 6.5(a), where the $m(h)$ curves clearly collapsed into two symmetric curves, one above and one below that for $T = T_C$. The inset of Fig. 6.5(a) shows the $ln(m)$ vs. $ln(h)$ plot, which demonstrates the collapsed curves more clearly. This feature confirms the reliability of the critical exponents to some degree. However, the insensitive nature of the logarithms may result in the collapse of the data into two branches, even for up to 10% deviations from the true β and γ values (see Refs. [181, 190, 191]).

The reliability of the exponent values can be further verified in a more rigorous manner by using eq. (6.6), which is more sensitive to the critical exponent values [181, 183]. In Fig. 6.5(b), the m^2 vs. h/m plot clearly collapse into two branches: one above and one below T_C. This further validates the reliability of the critical exponents obtained through the Kouvel - Fisher method.

6.5 Results: Critical Behavior in $Ni_2Mn_{0.85}Cu_{0.15}Ga$

Experiment and analysis procedures identical to those described above for Ni_2MnGa were applied to $Ni_2Mn_{0.85}Cu_{0.15}Ga$. The substitution of Cu reduces the second-order tran-

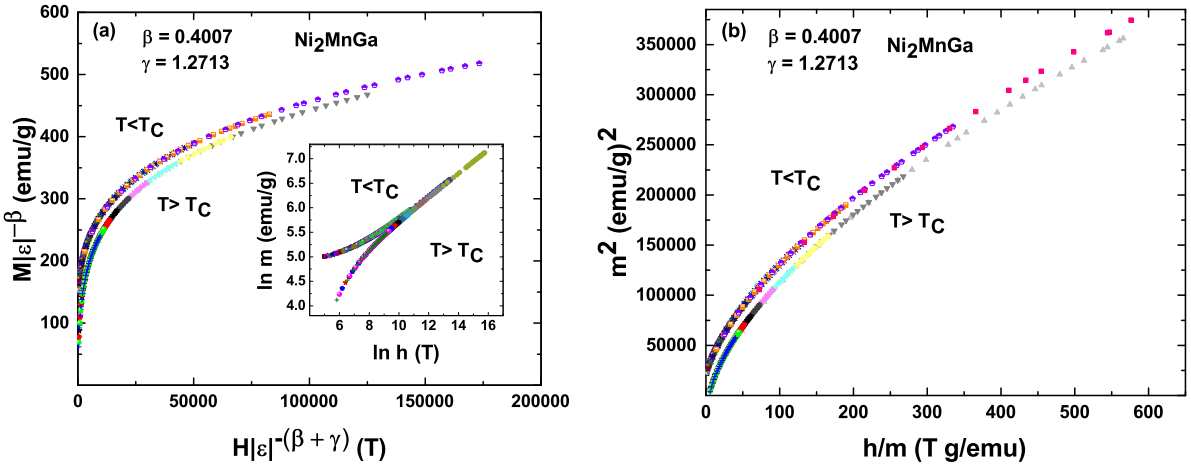

Figure 6.5: (a) The renormalized magnetization $[m \equiv M|\epsilon|^{-\beta}]$ vs. magnetic field $[h \equiv H|\epsilon|^{-(\beta+\gamma)}]$ curves according to eq. (6.4) with $\beta = 0.4007$ and $\gamma = 1.2713$ for Ni_2MnGa. The data collapse into two distinct branches, one above and one below T_C. Each color in the curves represents the contribution from a different isotherm. (Inset) A plot of $ln\,(m)$ vs. $ln\,(h)$. (b) The renormalized magnetization and field are plotted as m^2 vs. h/m according to eq. (6.6). The data collapse into two branches, one above and one below T_C.

sition temperature from $T_C = 382.4$ K in Ni_2MnGa to $T_C = 327.5$ K in $Ni_2Mn_{0.85}Cu_{0.15}Ga$. Concurrently, the first-order (martensitic) transition temperature increases from $T_M \approx 209$ K in Ni_2MnGa to $T_M \approx 273$ K in $Ni_2Mn_{0.85}Cu_{0.15}Ga$. It is to be noted that the two transitions do not overlap for a 15% Cu (x = 0.15) substitution, whereas they do occur at the same temperature for a 25% (x = 0.25) Cu substitution (not shown) [41].

In order to determine whether the martensitic phase transitions affect the critical exponents calculated for the second-order transitions, we followed the analysis procedure described by Phan et al. (see Ref. [192]), and constructed the universal entropy change (ΔS) vs. temperature (T) curves for both alloys following these steps [193]:

- The temperature axis above and below T_C was rescaled according to

$$\Theta \equiv \Theta_1 = (T - T_C)/(T_r - T_C). \tag{6.11}$$

Here, T_r is the reference temperature where $\Delta S = f \times \Delta S^{pk}$, and f is a certain

fraction, which was chosen to be 0.66 for the present case.

- The temperature axis was also rescaled using two well separated reference temperatures T_{r1} and T_{r2}, below and above T_C, respectively.

$$\theta \equiv \theta_2 = \begin{cases} -(T - T_C)/(T_{r1} - T_C) & T \leq T_C \\ (T - T_C)/(T_{r2} - T_C) & T > T_C \end{cases} \tag{6.12}$$

- All of the ΔS vs. T curves were normalized with respect to their peak values (ΔS^{pk}), and the normalized entropy change axis is $\Delta S' = \Delta S/\Delta S^{pk}$.

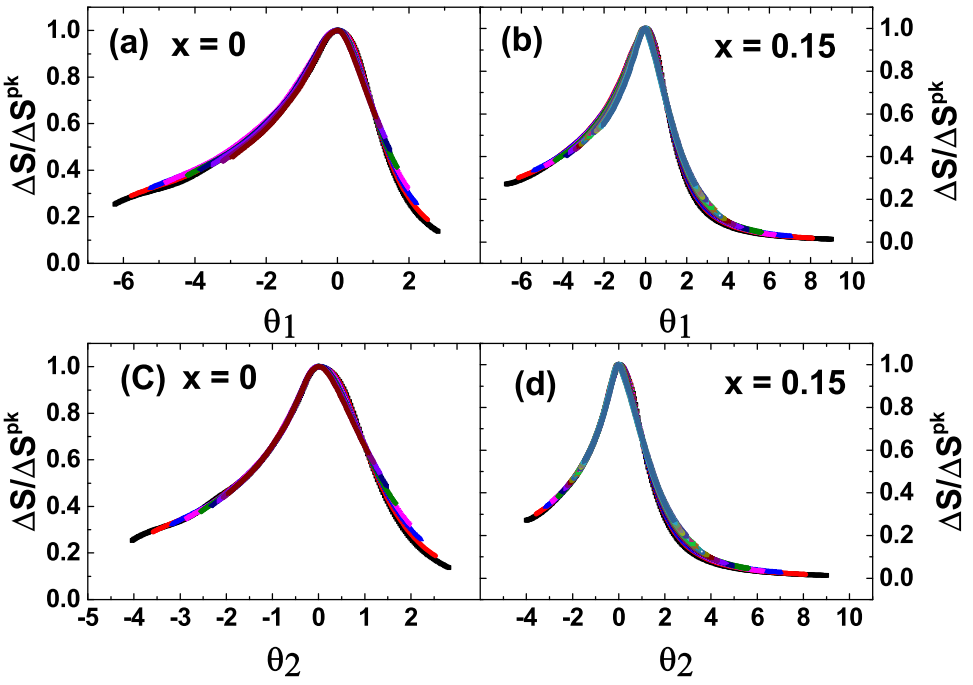

Figure 6.6: The universal curves for Ni_2MnGa (x = 0) and $Ni_2Mn_{0.85}Cu_{0.15}Ga$ (x = 0.15) using θ_1 (eq. 6.11) and θ_2 (eq. 6.12).

According to the work by Phan et al. [192], a perfect overlap (or collapse) of the ΔS vs. T curves using only one reference temperature T_r, as in eq. 6.11, is expected for a material with a single magnetic phase. However, in the presence of multiple magnetic phases, two reference temperatures, above and below T_C as in eq. 6.12, are needed in order to observe the collapse of the curves into a single universal curve. We created the universal curves for

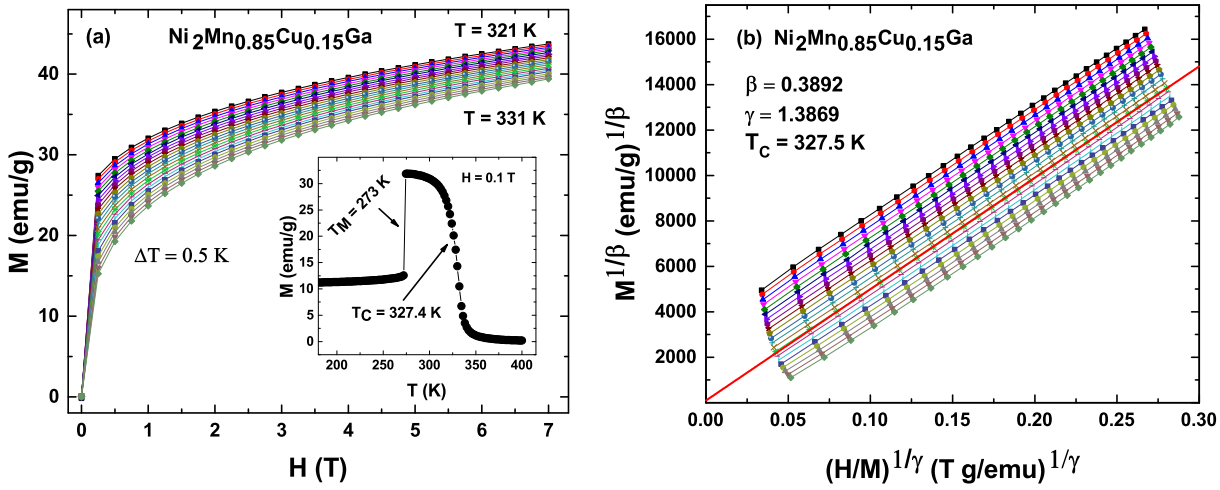

Figure 6.7: (a) Magnetization isotherms, $M(H)$, measured in $\Delta T = 0.5$ K increments from $H = 0$ T to $H = 7$ T for $Ni_2Mn_{0.85}Cu_{0.25}Ga$. (Inset) Magnetization (M) vs. temperature (T) in an applied magnetic field of $H = 0.1$ T. (b) Modified Arrott plot (MAP) using $\beta = 0.3892$ and $\gamma = 1.3869$. The solid red line indicates the linear fit to the isotherm at $T_C = 327.5$ K.

both alloys following both the one and two reference temperature protocols. A good collapse of the curves was observed for both of the alloys when only one reference temperature was used [Figs. 6.6(a) and 6.6(b)]. A slightly better collapse was achieved when two reference temperatures were used [Figs. 6.6(c) and 6.6(d)]. However, the difference is subtle, further demonstrating the fact that both of the alloys behave as single magnetic phase materials around their critical temperatures (T_C), where the isotherms were measured. Taking these features into account, we conclude that the martensitic phase and the martensitic transition did not significantly affect the values of the calculated critical exponents, i.e., the first-order transitions are far enough away from the second-order ones as to not alter the critical exponent analysis.

The $M(H)$ curves (isotherms) were collected in $\Delta T = 0.5$ K increments using the same protocol described earlier (Fig. 6.7(a)). Similar to Ni_2MnGa, the critical exponents for the 3D - Heisenberg model ($\beta = 0.365$ and $\gamma = 1.336$) were used as the initial trial values to construct the first MAP. Following the same iterative Kouvel - Fisher method, the critical

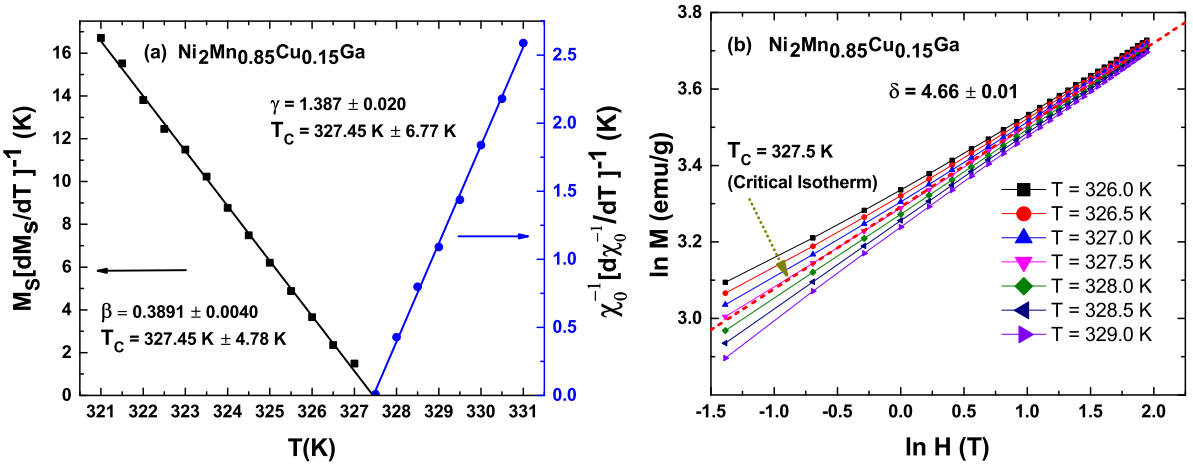

Figure 6.8: (a) Kouvel-Fisher plots for $Ni_2Mn_{0.85}Cu_{0.15}Ga$. Straight lines are linear fits to the data, from which β, γ, and T_C were calculated. (b) A plot of $ln(M)$ vs. $ln(H)$ near the critical isotherm for $Ni_2Mn_{0.85}Cu_{0.15}Ga$. The dashed red line represents the linear fit to the critical isotherm at $T_C = 327.5$ K; δ was calculated from the slope of this line.

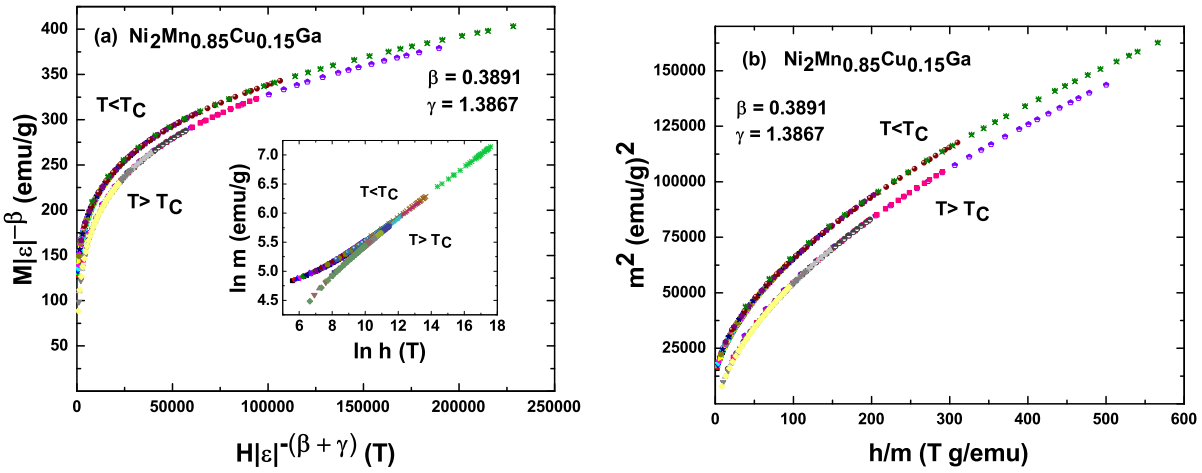

Figure 6.9: (a) The renormalized magnetization $[m \equiv M|\epsilon|^{-\beta}]$ vs. magnetic field $[h \equiv H|\epsilon|^{-(\beta+\gamma)}]$ curves according to eq. (6.4) with $\beta = 0.3891$ and $\gamma = 1.3867$ for $Ni_2Mn_{0.85}Cu_{0.15}Ga$. The data collapse into two distinct branches, one above and one below T_C. Each color in the curves represents the contribution from a different isotherm. (Inset) A plot of $ln\,(m)$ vs. $ln\,(h)$. (b) The renormalized magnetization and field are plotted as m^2 vs. h/m according to eq. (6.6). The data collapse into two branches, one above and one below T_C.

exponent values converged to $\beta = 0.389 \pm 0.004$, $\gamma = 1.39 \pm 0.02$, and $T_C = 327.45$ K $\pm$ 4.14 K (see Fig. 6.8(a) and Table 6.1).

A linear fitting of the critical isotherm at T = 327.5 K yielded $\delta = 4.66 \pm 0.01$. This exponent value was also calculated by using the β and γ values obtained through the Kouvel-Fisher method in the Widom relation (eq. (6.10)), which resulting in $\delta = 4.56 \pm 0.08$. As the isotherms were obtained in ΔT = 0.5 K increments, there was no isotherm at exactly T_C = 327.4 K. Instead, the isotherm at T = 327.5 K was chosen to be the critical isotherm, as it was closest to T_C. This may explain the slight difference in the δ values. Still, the agreement between the δ values obtained from two independent methods indicates the reliability of the critical exponents, β and γ. In Fig. 6.9(a), the m(h) curves collapsed into two branches, one above and one below T_C. Moreover, this collapsing feature was also observed in the m^2 vs. h/m plot (Fig. 6.9(b)).

For a second order magnetic transition, the peak magnetic entropy change (ΔS^{pk}) follows a power-law dependence in magnetic field, namely, $\Delta S^{pk} \propto H^n$ with $n = 2/3$ [194, 195]. The scaling exponent n is related to the exponents, β and γ, through the relation [196]

$$n = 1 + \frac{\beta - 1}{\beta + \gamma}. \tag{6.13}$$

Using the β and γ values obtained through the Kouvel-Fisher method in eq. (6.13) yielded $n = 0.64$ and 0.66 for Ni_2MnGa and $Ni_2Mn_{0.85}Cu_{0.15}Ga$, respectively. These values of n are quite close to the value of 2/3 predicted for a second-order magnetic phase transition. The magnetic entropy change (ΔS) was calculated from the magnetization isotherms using the integrated Maxwell relation, $\Delta S = \int_0^H \left(\frac{\partial M}{\partial T}\right)_H dH$. Fig. 6.10 shows the peak entropy change (ΔS^{pk}) vs. the rescaled magnetic field (H^n) plots. These plots demonstrate the linear relationship expected for second-order magnetic phase transitions. However, for $Ni_2Mn_{0.75}Cu_{0.25}Ga$, the peak entropy change (ΔS^{pk}) does not obey any power-law dependence in magnetic field (H), as shown in the inset of Fig. 6.10. This behavior is expected, as $Ni_2Mn_{0.75}Cu_{0.25}Ga$ undergoes a first-order coupled magnetostructural transition, which

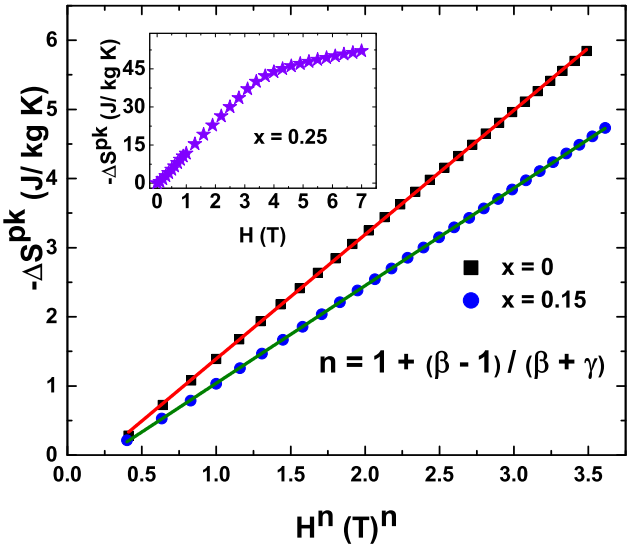

Figure 6.10: Plots of the peak entropy change (ΔS^{pk}) vs. rescaled magnetic field (H^n) for Ni_2MnGa (x = 0) and $Ni_2Mn_{0.85}Cu_{0.15}Ga$ (x = 0.15), where $n = 0.64$ and 0.66 were used, respectively. The solid lines in red and green represent linear fits. (Inset) A plot of peak entropy change (ΔS^{pk}) vs. magnetic field (H) for $Ni_2Mn_{0.75}Cu_{0.25}Ga$ (x = 0.25).

gives rise to a giant magnetocaloric effect.

It has been observed that the presence of short-range interactions or a weakening of long-range interactions can cause a broadening of the entropy change vs. temperature (ΔS vs. T) curves [192, 197, 198]. To investigate whether the Cu substitution broadens the ΔS vs. T curves, we calculated the full-width at half-maximum (δT_{FWHM}) of these curves. The relative cooling power at the full-width at half-maximum (RCP_{FWHM}) was also calculated using the relation, $RCP_{FWHM} = |-\Delta S^{pk} \times \delta T_{FWHM}|$. Here, ΔS^{pk} is the maximum value of the entropy change for a particular magnetic field. Fig. 6.11(a) shows that the δT_{FWHM} for $Ni_2Mn_{0.85}Cu_{0.15}Ga$ is larger at each field value compared to that of Ni_2MnGa, indicating a broadening of the ΔS vs. T curves. However, the RCP_{FWHM} remains essentially the same for both of the alloys (Fig. 6.11(b)). We have also observed that the peak values of the entropy change decreased due to the Cu substitution (not shown). In $Ni_2Mn_{0.85}Cu_{0.15}Ga$, a decrease in the maximum entropy change values and an increase in the width of the ΔS vs. T curves, as evident in Fig. 6.11(b), kept the RCP_{FWHM} values close to those of Ni_2MnGa. These facts point towards a broadening of the ΔS vs. T curves due to the

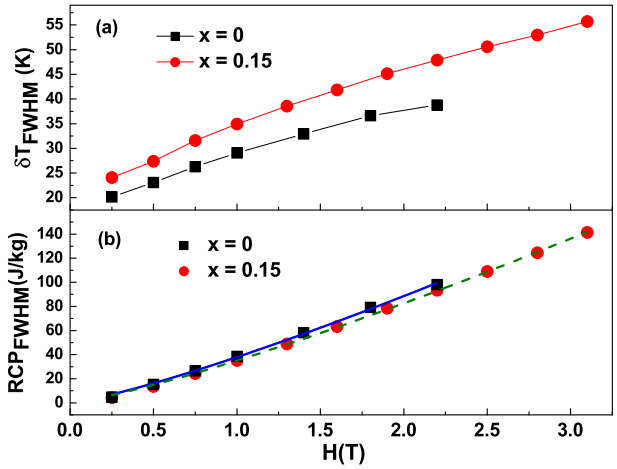

Figure 6.11: (a) The full-width at half-maximum (δT_{FWHM}) of the ΔS vs. T curves measured at various applied magnetic fields for Ni_2MnGa (x = 0) and $Ni_2Mn_{0.85}Cu_{0.15}Ga$ (x = 0.15). (b) The relative cooling power at the full-width at half-maximum (RCP_{FWHM}) for Ni_2MnGa (x = 0) and $Ni_2Mn_{0.85}Cu_{0.15}Ga$ (x = 0.15). The solid blue and dashed green lines represent power-law fits.

Cu substitution, indicating the presence of short-range exchange interactions. Similar to ΔS^{pk}, the RCP_{FWHM} is predicted to follow a power-law dependence in magnetic field [199], given by $RCP_{FWHM} \propto H^{1+1/\delta}$. The power-law fitting of the data as shown in Fig. 6.11(b), resulted in $\delta = 4.54$ and 4.56 for Ni_2MnGa and $Ni_2Mn_{0.85}Cu_{0.15}Ga$, respectively. These values are close to the values obtained through other methods (see Table 6.1).

6.6 Discussion

The Heisenberg model is best suited to describe ferromagnetism in localized systems [181]. Despite the localized nature of the ferromagnetism in Ni_2MnGa [175], the critical exponents deviate significantly from the Heisenberg values towards the mean-field values. However, the exponents for $Ni_2Mn_{0.85}Cu_{0.15}Ga$ are closer to the Heisenberg values (see Table 6.1). As mentioned previously, the critical exponents depend on the lattice dimensionality (d), spin dimensionality (n), and range of exchange interaction (σ). A relation between these quantities and the critical exponent γ (eq. (6.14)) was derived through a renormalization group approach [183, 190, 200, 201], and can be used to estimate the

range of spin interactions. This relation is given by

$$\gamma = 1 + (4/d)\left(\frac{n+2}{n+8}\right)\Delta\sigma + \frac{8(n+2)(n-4)}{d^2(n+8)^2}\left[1 + \frac{2G(d/2)(7n+20)}{(n-4)(n+8)}\right]\Delta\sigma^2, \qquad (6.14)$$

where $\Delta\sigma = (\sigma - \frac{d}{2})$ and $G(\frac{d}{2}) = 3 - \frac{1}{4}(\frac{d}{2})^2$.

According to this approach, the exchange interaction is long-range when $\sigma < 2$, and short-range if $\sigma > 2$. Following the procedure described by Fisher et al. [190] and Pramanik et al. [183], for a particular set of values of $\{d : n\}$, the parameter σ was adjusted until the γ value from the above equation was equal to the one obtained experimentally. This value of σ was then used to calculate other exponents using the following relations: $\nu = \gamma/\sigma$, $\alpha = 2 - \nu d$, $\beta = (2 - \alpha - \gamma)/2$, and $\delta = 1 + \gamma/\beta$.

For Ni_2MnGa, $\{d : n\} = \{2 : 3\}$ and $\sigma = 1.216$ produced exponent values of $\beta = 0.4098$, $\gamma = 1.272$, and $\delta = 4.10$, which are close to the experimentally determined values. Similarly, for $Ni_2Mn_{0.85}Cu_{0.15}Ga$, $\{d : n\} = \{2 : 3\}$ and $\sigma = 1.283$ resulted in critical exponent values of $\beta = 0.3875$, $\gamma = 1.387$, and $\delta = 4.58$, also close to the experimentally determined values. These calculations suggest that the effective dimensionality of spin interactions in both alloys is less than three. This may originate from the fact that, in Mn-based Heusler alloys, the magnetic moment is mostly confined to the two-dimensional Mn sublattices, and the magnetism is governed by the Mn atoms [183, 202]. Because of the large distance between the Mn atoms ($d_{Mn-Mn} > 4$ Å) [202], there is no considerable overlapping of the Mn 3d states and, hence, no significant direct interaction between the Mn atoms [203]. This is why an indirect Ruderman-Kittel-Kasuya-Yosida (RKKY) exchange interaction mediated by the Ni conduction electrons gives rise to the ferromagnetism in Ni_2MnGa [175, 179, 202, 204]. Therefore, the manifestation of long-range interactions in Ni_2MnGa is not surprising. It is clear that the Cu substitution for Mn in Ni_2MnGa decreases the values of β and T_C, while it increases the value of γ. A somewhat opposite scenario was described by Halder et al. for $TbCo_{2-x}Fe_x$ [174]. In that case, the critical exponents for the parent

Table 6.1: The critical exponent values (β, γ, and δ) and the transition temperatures (T_C) obtained from the Kouvel-Fisher (KF) method and the critical isotherms (CI). The theoretical values of the critical exponents for various universality classes are given for comparison.

Composition	Technique	β	γ	T_C	δ
Ni_2MnGa (This work)	KF	0.401 ± 0.003	1.27 ± 0.02	382.42 ± 5.13 K	4.17 ± 0.08
	CI				4.100 ± 0.007
$Ni_2Mn_{0.85}Cu_{0.15}Ga$ (This work)	KF	0.389 ± 0.004	1.39 ± 0.02	327.45 ± 4.14 K	4.56 ± 0.08
	CI				4.66 ± 0.01
Mean Field Model [183, 186]	Theory	0.5	1.0		3.0
3D Heisenberg Model [181, 186]	Theory	0.365	1.336		4.66
$Ni_{50}Mn_{50-x}Sn_x$ [169]					
x = 13	KF	0.385 ± 0.035	1.083 ± 0.060	303.6 K	-
x = 14	KF	0.496 ± 0.015	1.024 ± 0.059	304.5 K	-
$Ni_{50-y}Gd_yMn_{37}Sn_{13}$ [170]					
y = 1	KF	0.473 ± 0.020	1.141 ± 0.017	299.0 ± 0.02 K	-
y = 3	KF	0.469 ± 0.068	1.214 ± 0.042	302.9 ± 0.7 K	-
$Ni_{43}Mn_{46}Sn_8In_3$ [171]	KF	0.485 ± 0.013	0.987 ± 0.017	296.8 K	3.035
$Ni_{43}Mn_{46}Sn_8Cr_3$ [171]	KF	0.549 ± 0.008	0.965 ± 0.012	301.8 K	2.758
$Ni_{2.2}Mn_{0.6}V_{0.18}Ga_{1.08}$ [172]	KF	0.48	1.05	268 K	3.02
$Ni_{47}Mn_{40}Sn_{13-x}Cu_x$ [173]					
x = 0	KF	0.479 ± 0.010	1.087 ± 0.017	313.50 K	3.269
x = 0.5	KF	0.521 ± 0.008	1.061 ± 0.010	315.96 K	3.036
$TbCo_{2-x}Fe_x$ [174]					
x = 0	KF	0.380(4)	1.407(8)	224.83(7) K	4.85(3)
x = 0.1	KF	0.541(1)	1.023(2)	304.48(5) K	2.75(4)

compound $TbCo_2$ were very close to the Heisenberg values. However, for $TbCo_{1.9}Fe_{0.1}$, the T_C and the critical exponent β increased, while the value of γ decreased. Overall, the critical exponents for $TbCo_{1.9}Fe_{0.1}$ were close to the mean-field values. They argued that the Fe substitution causes the RKKY interactions to dominate over the exchange interactions. The RKKY interactions extend beyond the nearest neighbors, and this long-range interaction causes a deviation of the critical exponents from the Heisenberg values toward the mean-field values. In another investigation, Zhang et al. [170] studied the role of Gd substitution in $Ni_{50-y}Gd_yMn_{37}Sn_{13}$ through critical exponent analysis. While the parent compound (y = 0) exhibited short-range FM interactions, the Gd-substituted compounds indicated long-range FM interactions with the critical exponents close to the mean-field values. They argued that the substitution of the rare-earth Gd atom in the Ni

site reestablished the long-range RKKY-type FM interactions, drove the system towards long-range order and, hence, towards mean-field like critical behavior.

In the case of Ni_2MnGa, the deviation of the critical exponent values from the 3D - Heisenberg values toward the mean-field values could be attributed to the presence of long-range RKKY interactions [174, 185, 201]. The substitution of nonmagnetic Cu in the Mn site likely weakens the RKKY interactions and hence the observed reduction in T_C in $Ni_2Mn_{0.85}Cu_{0.15}Ga$. As stated earlier, Cu substitution enhances the hybridization effects between the Ni d states and Ga p states, and causes the system to be more magnetically delocalized [175]. This factor can cause the short-range interactions to dominate, which, along with the weakening of the long-range interactions, may explain why the critical exponents for $Ni_2Mn_{0.85}Cu_{0.15}Ga$ are closer to the 3D-Heisenberg values.

6.7 Conclusions

In summary, we calculated the critical exponents (β and γ) of the ferromagnetic transitions in polycrystalline Ni_2MnGa and $Ni_2Mn_{0.85}Cu_{0.15}Ga$ using the Kouvel-Fisher method. For both compounds, the exponent δ was obtained from critical isotherms, as well as through the Widom scaling relation. For the obtained values of the critical exponents, the reduced magnetization vs. field data collapsed into two branches, one above and one below T_C, in compliance with the scaling equation of state. In Ni_2MnGa, the critical exponents deviate from the 3D-Heisenberg values toward the mean-field values. This is consistent with the presence of long-range RKKY exchange interactions, which govern the magnetism in Ni_2MnGa. The critical exponents in $Ni_2Mn_{0.85}Cu_{0.15}Ga$ are close to the theoretical values of the 3D-Heisenberg model with short-range interactions. The substitution of nonmagnetic Cu in the Mn site weakens the long-range RKKY interactions and enhances the Ni-Ga hybridization. These factors may explain the similarity of the critical exponent values in $Ni_2Mn_{0.85}Cu_{0.15}Ga$ to those of the 3D-Heisenberg model. In order to obtain the desired functional properties, and to study the underlying physics in magnetic materials, various strategies, such as stoichiometry variation, elemental substitution, etc., are often

employed. Although critical exponents cannot be obtained for discontinuous first-order transitions, analyzing the critical behavior in the vicinity of second-order phase transitions can be used to understand how the interactions change with substitution. This can provide some insight as to how the interactions evolve as the substitution levels increase toward values that produce coupled, first-order transitions.

Chapter 7
Concluding Remarks

The investigations in this dissertation focused on the magnetocaloric effects (MCE), barocaloric effects (BCE), and phase transitions. For the MnNiSi-based system, a coupled first-order magnetostructural transition (MST) was realized through isostructural alloying with FeCoGe. In the new system, $(MnNiSi)_{1-x}(FeCoGe)_x$, the coupled MST produced giant MCEs and BCEs. The observation of these two caloric effects in the same material due to the same phase transition qualify this compound as a multicaloric material. The giant caloric effects, repeatable synthesis process, and the fact that this material consists of non-toxic, inexpensive, and naturally abundant elements are some of the factors that can make it a good candidate for application in solid-state cooling devices. This material also presents a unique opportunity to investigate the combined/simultaneous effects of magnetic field and hydrostatic pressure on the caloric effects, since it exhibits both the magnetic field induced MCE and pressure induced BCE. The mechanisms behind coupled magnetostructural transitions are not yet fully understood. In this respect, this material can be used as a test-bed to further investigate the first-order phase transitions from theoretical and experimental points of view.

In the second project, the pressure dependence of the metamagnetic transitions in $DyRu_2Si_2$ was investigated. We concluded that the disappearance, and the subsequent reappearance, of the metamagnetic transitions with increasing applied hydrostatic pressure are connected to the modulation of the long-range Ruderman-Kittel-Kasuya-Yosida (RKKY) exchange interactions, caused by a change in interatomic distances due to the applied pressure. We also investigated the magnetocaloric and magnetostrictive properties of this material at various pressures.

The calculated values of the critical exponents for the parent compound, Ni_2MnGa, which indicated a deviation from a 3D-Heisenberg behavior to a mean-field-like behavior due to the long-range RKKY interactions. On the other hand, the critical exponents for

$Ni_2Mn_{0.85}Cu_{0.15}Ga$ pointed towards a 3D-Heisenberg-type behavior due to the weakening of the long-range interactions caused by the substitution of the non-magnetic Cu. This was consistent with the Ni-Ga hybridization effects reported for x = 0.25, which could not be studied using this method since it only has a first-order phase transition. This type of analysis can be applied to any material system that shows a second-order magnetic phase transition in order to get a better understanding of the nature of the phase transition, exchange interaction, and so on. Furthermore, it can also shed light into the evolution of the magnetic interactions with various strategies (e.g., elemental substitution, stoichiometry variation, pressure, etc.) that lead to first-order phase transitions.

References

[1] V. Franco, J.S. Blázquez, B. Ingale, and A. Conde. *Annual Review of Materials Research*, 42(1):305–342, 2012.

[2] US energy Information Administration. Annual Energy Review 2009, 2010. Washington, DC: US Gov. Print. Off.

[3] Melvin M Vopson. *Journal of Physics D: Applied Physics*, 46(34):345304, 2013.

[4] J. Romero Gómez, R. Ferreiro Garcia, A. De Miguel Catoira, and M. Romero Gómez. *Renewable and Sustainable Energy Reviews*, 17:74 – 82, 2013.

[5] D. Coulomb. In *Proceedings of the Second International Conference on Magnetic Refrigeration at Room Temperature*, pages 3–5, Paris, 2007. International Institute of Refrigeration,.

[6] K.A. Gschneidner Jr. and V.K. Pecharsky. *International Journal of Refrigeration*, 31:945 – 961, 2008.

[7] M. Ujihara, G. P. Carman, and D. G. Lee. *Applied Physics Letters*, 91(9):093508, 2007.

[8] Claudio Palmy. *European Journal of Physics*, 27(6):1289, 2006.

[9] A.M. Tishin, Y.I. Spichkin, V.I. Zverev, and P.W. Egolf. *International Journal of Refrigeration*, 68:177 – 186, 2016.

[10] Sudip Pandey, Abdiel Quetz, Anil Aryal, Igor Dubenko, Dipanjan Mazumdar, Shane Stadler, and Naushad Ali. *International Journal of Hyperthermia*, 33(7):779–784, 2017.

[11] Lluis Manosa, Antoni Planes, and Mehmet Acet. *J. Mater. Chem. A*, 1:4925–4936, 2013.

[12] X. Moya, S. Kar-Narayan, and N. D. Mathur. *Nature Materials*, 13:439, 2014.

[13] Anders Smith. *The European Physical Journal H*, 38(4):507–517, 2013.

[14] James Joule. *Phil. Mag., Ser. 3*, 23:263–276, 1843.

[15] William Thomson. *Phil. Mag., Ser.*, 5:4–27, 1878.

[16] Anders Smith, Christian R.H. Bahl, Rasmus Bjørk, Kurt Engelbrecht, Kaspar K. Nielsen, and Nini Pryds. *Advanced Energy Materials*, 2(11):1288–1318, 2012.

[17] E. Warburg. *Annals of Physics*, 13:141–164, 1881.

[18] J. Stefan. *Wien. Ber.*, 64:193–224, 1871.

[19] J. Stefan. *Annalen der Physik*, 274(11):427–440, 1889.

[20] Thomas Edison. Pyromagnetic motor. *U.S. Patent* US380100, 1888.

[21] Thomas Edison. Pyromagnetic generator. *U.S. Patent* US3476983, 1892.

[22] Nikola Tesla. Thermo-magnetic motor. *U.S. Patent* US396121, 1889.

[23] Nikola Tesla. Pyromagneto-electric generator. *U.S. Patent* US428057, 1890.

[24] A. Piccard P. Weiss. *Compt Rend Ac Sci*, 166:352, 1918.

[25] P Debye. *Annals of Physics*, 81:1154–1160, 1926.

[26] P. Weiss and R. Forrer. *Ann. Phys*, 5:153, 1926.

[27] WF Giauque. *Journal of the American Chemical Society*, 49:1864–1870, 1927.

[28] W. F. Giauque and D. P. MacDougall. *Phys. Rev.*, 43:768–768, 1933.

[29] G. V. Brown. *Journal of Applied Physics*, 47(8):3673–3680, 1976.

[30] John A Barclay. *Journal of Alloys and Compounds*, 207-208:355 – 361, 1994.

[31] W. A. Steyert. *Journal of Applied Physics*, 49(3):1216–1226, 1978.

[32] J.A. Barclay and W.A. Steyert. Active magnetic regenerator. *U.S. Patent* US428057, 1982.

[33] C. Zimm, A. Jastrab, A. Sternberg, V. Pecharsky, K. Gschneidner, M. Osborne, and I. Anderson. *Description and Performance of a Near-Room Temperature Magnetic Refrigerator*, pages 1759–1766. Springer US, Boston, MA, 1998.

[34] M.L. Lawton Jr., C.B. Zimm, and A.G. Jastrab. Reciprocating active magnetic regenerator refrigeration apparatus. *U.S. Patent* US428057, 1999.

[35] K.A. Gschneidner Jr., V.K. Pecharsky, C.B. Zimm, and A. Sternberg. Magnetic refrigerators/freezers and air conditioners. In *Proceedings of the Domotechnica Appliance Engineering Conference*, Cologne, Germany, 2001.

[36] V. K. Pecharsky and K. A. Gschneidner, Jr. *Phys. Rev. Lett.*, 78:4494–4497, 1997.

[37] V. K. Pecharsky and K. A. Gschneidner Jr. *Applied Physics Letters*, 70:3299–3301, 1997.

[38] H. Wada and Y. Tanabe. *Applied Physics Letters*, 79(20):3302–3304, 2001.

[39] Sergio Gama, Adelino A. Coelho, Ariana de Campos, A. Magnus G. Carvalho, Flávio C. G. Gandra, Pedro J. von Ranke, and Nilson A. de Oliveira. *Phys. Rev. Lett.*, 93: 237202, 2004.

[40] A. Fujita, S. Fujieda, Y. Hasegawa, and K. Fukamichi. *Phys. Rev. B*, 67:104416, 2003.

[41] Shane Stadler, Mahmud Khan, Joseph Mitchell, Naushad Ali, Angelo M. Gomes, Igor Dubenko, Armando Y. Takeuchi, and Alberto P. Guimarães. *Appl. Phys. Lett.*, 88:192511, 2006.

[42] Massimo Pasquale, Carlo Paolo Sasso, and L. H. Lewis. *Journal of Applied Physics*, 95(11):6918, 2004.

[43] N. T. Trung, L. Zhang, L. Caron, K. H. J. Buschow, and E. Brück. *Applied Physics Letters*, 96:172504, 2010.

[44] Tapas Samanta, Daniel L. Lepkowski, Ahmad Us Saleheen, Alok Shankar, Joseph Prestigiacomo, Igor Dubenko, Abdiel Quetz, Iain W. H. Oswald, Gregory T. McCandless, Julia Y. Chan, Philip W. Adams, David P. Young, Naushad Ali, and Shane Stadler. *Phys. Rev. B*, 91:020401, 2015.

[45] Tapas Samanta, Daniel L. Lepkowski, Ahmad Us Saleheen, Alok Shankar, Joseph Prestigiacomo, Igor Dubenko, Abdiel Quetz, Iain W. H. Oswald, Gregory T. McCandless, Julia Y. Chan, Philip W. Adams, David P. Young, Naushad Ali, and Shane Stadler. *Journal of Applied Physics*, 117(12):123911, 2015.

[46] Tapas Samanta, I. Das, and S. Banarjee. *Appl. Phys. Lett.*, 91:152506, 2007.

[47] Tapas Paramanik, Kalipada Das, Tapas Samanta, and I. Das. *J. Appl. Phys.*, 115: 083914, 2014.

[48] H. Zhang, B. G. Shen, Z. Y. Xu, J. Shen, F. X. Hu, J. R. Sun, and Y. Long. *Appl. Phys. Lett.*, 102:092401, 2013.

[49] B.F Yu, Q Gao, B Zhang, X.Z Meng, and Z Chen. *International Journal of Refrigeration*, 26:622 – 636, 2003.

[50] K. A. Gschneidner Jr., V. K. Pecharsky, and A. O. Tsokol. *Reports on Progress in Physics*, 68:1479, 2005.

[51] Lluís Mañosa and Antoni Planes. *Advanced Materials*, 29(11):1603607, 2017.

[52] C. A. Jenkins, A. Scholl, R. Kainuma, H. J. Elmers, and T. Omori. *Applied Physics Letters*, 100(3):032401, 2012.

[53] Aleksandr N Vasil'ev, Vasilii D Buchel'nikov, T Takagi, Vladimir V Khovailo, and Emmanuil I Estrin. *Physics-Uspekhi*, 46(6):559, 2003.

[54] Erell Bonnot, Ricardo Romero, Lluís Mañosa, Eduard Vives, and Antoni Planes. *Phys. Rev. Lett.*, 100:125901, Mar 2008.

[55] Lluís Mañosa, Antoni Planes, Eduard Vives, Erell Bonnot, and Ricardo Romero. *Functional Materials Letters*, 02(02):73–78, 2009.

[56] Eduard Vives, Susan Burrows, Rachel S. Edwards, Steve Dixon, Lluís Mañosa, Antoni Planes, and Ricardo Romero. *Applied Physics Letters*, 98(1):011902, 2011.

[57] J Quarini and A Prince. *Proceedings of the Institution of Mechanical Engineers, Part C: Journal of Mechanical Engineering Science*, 218(10):1175–1179, 2004.

[58] Jun Cui, Yiming Wu, Jan Muehlbauer, Yunho Hwang, Reinhard Radermacher, Sean Fackler, Manfred Wuttig, and Ichiro Takeuchi. *Applied Physics Letters*, 101(7): 073904, 2012.

[59] J. Tušek, K. Engelbrecht, L. P. Mikkelsen, and N. Pryds. *Journal of Applied Physics*, 117(12):124901, 2015.

[60] C. Bechtold, C. Chluba, R. Lima de Miranda, and E. Quandt. *Applied Physics Letters*, 101(9):091903, 2012.

[61] C. Chluba, H. Ossmer, C. Zamponi, M. Kohl, and E. Quandt. *Shape Memory and Superelasticity*, 2(1):95–103, 2016.

[62] S.A. Nikitin, G. Myalikgulyev, M.P. Annaorazov, A.L. Tyurin, R.W. Myndyev, and S.A. Akopyan. *Physics Letters A*, 171(3):234 – 236, 1992.

[63] Enric Stern-Taulats, Antoni Planes, Pol Lloveras, Maria Barrio, Josep-Lluís Tamarit, Sabyasachi Pramanick, Subham Majumdar, Carlos Frontera, and Lluís Mañosa. *Phys. Rev. B*, 89:214105, 2014.

[64] Enric Stern-Taulats, Adrià Gràcia-Condal, Antoni Planes, Pol Lloveras, Maria Barrio, Josep-Lluís Tamarit, Sabyasachi Pramanick, Subham Majumdar, and Lluís Mañosa. *Applied Physics Letters*, 107(15):152409, 2015.

[65] S.A. Nikitin, G. Myalikgulyev, A.M. Tishin, M.P. Annaorazov, K.A. Asatryan, and A.L. Tyurin. *Physics Letters A*, 148(6):363 – 366, 1990.

[66] G. Shirane, R. Nathans, and C. W. Chen. *Phys. Rev.*, 134:A1547–A1553, 1964.

[67] B. G. Shen, J. R. Sun, F. X. Hu, H. W. Zhang, and Z. H. Cheng. *Advanced Materials*, 21(45):4545–4564, 2009.

[68] Lluís Mañosa, David González-Alonso, Antoni Planes, Maria Barrio, Josep-Lluís Tamarit, Ivan S. Titov, Mehmet Acet, Amitava Bhattacharyya, and Subham Majumdar. *Nature Communications*, 2:595, 2011.

[69] Daichi Matsunami, Asaya Fujita, Koshi Takenaka, and Mika Kano. *Nature Materials*, 14:73, 2014.

[70] N. A. de Oliveira. *Applied Physics Letters*, 90(5):052501, 2007.

[71] Suheyla Yuce, Maria Barrio, Baris Emre, Enric Stern-Taulats, Antoni Planes, Josep-Lluís Tamarit, Yaroslav Mudryk, Karl A. Gschneidner Jr., Vitalij K. Pecharsky, and Lluís Mañosa. *Applied Physics Letters*, 101(7):071906, 2012.

[72] Marvin Schmidt, Andreas Schütze, and Stefan Seelecke. *International Journal of Refrigeration*, 54:88 – 97, 2015.

[73] Suxin Qian, Yunlong Geng, Yi Wang, Jiazhen Ling, Yunho Hwang, Reinhard Radermacher, Ichiro Takeuchi, and Jun Cui. *International Journal of Refrigeration*, 64:1 – 19, 2016.

[74] Sheng-Guo Lu and Qiming Zhang. *Advanced Materials*, 21(19):1983–1987, 2009.

[75] Matjaz Valant. *Progress in Materials Science*, 57(6):980 – 1009, 2012.

[76] E. Birks, M. Dunce, and A. Sternberg. *Ferroelectrics*, 400(1):336–343, 2010.

[77] L.A. Shebanov, E.K. Birks, and K.Y. Borman. *Fizika Tverdogo Tela*, 30(8):2464–2469, 1988.

[78] P. Kobeko and J. Kurtschatov. *Zeitschrift für Physik*, 66(3):192–205, Mar 1930.

[79] Gordon G. Wiseman and Juergen K. Kuebler. *Phys. Rev.*, 131:2023–2027, Sep 1963.

[80] H Baumgartner. *Helvetica Physica Acta*, 23(6–7):651–696, 1950.

[81] W. N. Lawless and A. J. Morrow. *Ferroelectrics*, 15(1):159–165, 1977.

[82] Y. V. Sinyavsky and V. M. Brodyansky. *Ferroelectrics*, 131(1):321–325, 1992.

[83] A. S. Mischenko, Q. Zhang, J. F. Scott, R. W. Whatmore, and N. D. Mathur. *Science*, 311(5765):1270–1271, 2006.

[84] Y. R. Kucherov. Piezo-pyroelectric energy converter and method. *U.S. Patent* 5644184, 1997.

[85] N. Mathur and A. Mischenko. Solid state electrocaloric cooling devices and methods. *U.S. Patent* WO 2006/056809, 2006.

[86] Melvin M. Vopson. *Solid State Communications*, 152(23):2067 – 2070, 2012.

[87] Hui Meng, Bing Li, Weijun Ren, and Zhidong Zhang. *Physics Letters A*, 377(7):567 – 571, 2013.

[88] M. Vopsaroiu, M.G. Cain, G. Sreenivasulu, G. Srinivasan, and A.M. Balbashov. *Materials Letters*, 66(1):282 – 284, 2012.

[89] Martin Gajek, Manuel Bibes, Stéphane Fusil, Karim Bouzehouane, Josep Fontcuberta, Agnès Barthélémy, and Albert Fert. *Nature Materials*, 6:296, 2007.

[90] Manuel Bibes and Agnès Barthélémy. *Nature Materials*, 7:425, 2008.

[91] J. F. Scott. *Nature Materials*, 6:256, 2007.

[92] Shuxiang Dong, J. F. Li, and D. Viehland. *Applied Physics Letters*, 84(21):4188–4190, 2004.

[93] Vijay Srivastava, Yintao Song, Kanwal Bhatti, and R. D. James. *Advanced Energy Materials*, 1(1):97–104, 2011.

[94] K. Alex Müller, François Fauth, Stephan Fischer, Max Koch, Albert Furrer, and Philippe Lacorre. *Applied Physics Letters*, 73(8):1056–1058, 1998.

[95] Vitalij K. Pecharsky and Karl A. Gschneidner Jr. *Journal of Magnetism and Magnetic Materials*, 200:44 – 56, 1999.

[96] N.A. de Oliveira and P.J. von Ranke. *Physics Reports*, 489:89 – 159, 2010.

[97] N.A. de Oliveira, P.J. von Ranke, and A. Troper. *International Journal of Refrigeration*, 37:237 – 248, 2014.

[98] A.M. Tishin and Y.I. Spichkin. *The Magnetocaloric Effect and its Applications*. Institute of Physics, London, 2003.

[99] O Tegus, E Brück, L Zhang, Dagula, K.H.J Buschow, and F.R de Boer. *Physica B: Condensed Matter*, 319(1):174 – 192, 2002.

[100] V. K. Pecharsky, K. A. Gschneidner, A. O. Pecharsky, and A. M. Tishin. *Phys. Rev. B*, 64:144406, 2001.

[101] Sindhunil Barman Roy. *Journal of Physics: Condensed Matter*, 25(18):183201, 2013.

[102] V.K. Pecharsky, K.A. Gschneidner, Ya. Mudryk, and Durga Paudyal. *Journal of Magnetism and Magnetic Materials*, 321(21):3541 – 3547, 2009.

[103] B.K. Banerjee. *Physics Letters*, 12:16–17, 1964.

[104] V. K. Pecharsky, A. P. Holm, K. A. Gschneidner, and R. Rink. *Phys. Rev. Lett.*, 91: 197204, 2003.

[105] Jr. K.A. Gschneidner, Y. Mudryk, and V.K. Pecharsky. *Scripta Materialia*, 67:572–577, 2012.

[106] V. K. Pecharsky and K. A. Gschneidner. *Advanced Materials*, 13(9):683–686, 2001.

[107] A. Barcza, Z. Gercsi, H. Michor, K. Suzuki, W. Kockelmann, K. S. Knight, and K. G. Sandeman. *Phys. Rev. B*, 87:064410, Feb 2013.

[108] Vittorio Basso. *Journal of Physics: Condensed Matter*, 23(22):226004, 2011.

[109] Vitalij K. Pecharsky, Jun Cui, and Duane D. Johnson. *Phil. Trans. R. Soc. A*, 374 (2074):20150305, 2016.

[110] A. Giguère, M. Foldeaki, B. Ravi Gopal, R. Chahine, T. K. Bose, A. Frydman, and J. A. Barclay. *Phys. Rev. Lett.*, 83:2262–2265, Sep 1999.

[111] Milan Bratko. *The magnetocaloric effect at a first order phase transition*. PhD thesis, Imperial College London, Department of Physics, 2013.

[112] J. R. Sun, F. X. Hu, and B. G. Shen. *Phys. Rev. Lett.*, 85:4191–4191, Nov 2000.

[113] S. M. Benford and G. V. Brown. *Journal of Applied Physics*, 52(3):2110–2112, 1981.

[114] S. Yu. Dan'kov, A. M. Tishin, V. K. Pecharsky, and K. A. Gschneidner Jr. *Review of Scientific Instruments*, 68(6):2432–2437, 1997.

[115] W. Otowski, C. Glorieux, R. Hofman, and J. Thoen. *Thermochimica Acta*, 218:123 – 133, 1993.

[116] R. Bjørk, C.R.H. Bahl, and M. Katter. *Journal of Magnetism and Magnetic Materials*, 322(24):3882 – 3888, 2010.

[117] Jordi Marcos, Fèlix Casanova, Xavier Batlle, Amılcar Labarta, Antoni Planes, and Lluıs Mañosa. *Review of Scientific Instruments*, 74(11):4768–4771, 2003.

[118] Lluís Mañosa, David González-Alonso, Antoni Planes, Erell Bonnot, Maria Barrio, Josep-Lluís Tamarit, Seda Aksoy, and Mehmet Acet. *Nature Materials*, 9:478, 2010.

[119] E. Liu, W. Wang, L. Feng, W. Zhu, G. Li, J. Chen, H. Zhang, G. Wu, C. Jiang, H. Xu, and F. de Boer. *Nature Commun.*, 3:873, 2012.

[120] N. T. Trung, L. Zhang, L. Caron, K. H. J. Buschow, and E. Brück. *Appl. Phys. Lett.*, 96:172504, 2010.

[121] T. Samanta, I. Dubenko, A. Quetz, S. Stadler, and N. Ali. *Appl. Phys. Lett.*, 101: 242405, 2012.

[122] C. L. Zhang, D. H. Wang, Z. D. Han, B. Qian, H. F. Shi, C. Zhu, J. Chen, and T. Z. Wang. *Appl. Phys. Lett.*, 103:132411, 2013.

[123] T. Samanta, I. Dubenko, A. Quetz, S. Temple, S. Stadler, and N. Ali. *Appl. Phys. Lett.*, 100:052404, 2012.

[124] E. K. Liu, W. Zhu, L. Feng, J. L. Chen, W. H. Wang, G. H. Wu, H. Y. Liu, F. B. Meng, H. Z. Luo, and Y. X. Li. *EPL*, 91:17003, 2010.

[125] N. T. Trung, V. Biharie, L. Zhang, L. Caron, K. H. J. Buschow, and E. Brück. *Appl. Phys. Lett.*, 96:162507, 2010.

[126] S. C. Ma, Y. X. Zheng, H. C. Xuan, L. J. Shen, Q. Q. Cao, D. H. Wang, Z. C. Zhong, and Y. W. Du. *J. Magn. Magn. Mater.*, 324:135, 2012.

[127] Y. K. Fang, C. C. Yeh, C. W. Chang, W. C. Chang, M. G. Zhu, and W. Li. *Scr. Mater.*, 57:453, 2007.

[128] V. Johnson. *Inorg. Chem.*, 14:1117, 1975.

[129] W. Bazela, A. Szytula, J. Todorovic, and A. Zieba. *Phys. Status Solidi A*, 64:367, 1981.

[130] A. SzytuLa, A. T. Pedziwiatr, Z. Tomkowicz, and W. Bazela. *J. Magn. Magn. Mater.*, 25:176, 1981.

[131] P. Lloveras, E. Stern-Taulats, M. Barrio, J. Ll Tamarit, S. Crossley, W. Li, V. Pomjakushin, A. Planes, Ll Mañosa, N. D. Mathur, and X. Moya. *Nature Communications*, 6:8801, 2015.

[132] S. Crossley, N. D. Mathur, and X. Moya. *AIP Advances*, 5(6):067153, 2015.

[133] Rong-Rong Wu, Li-Fu Bao, Feng-Xia Hu, Hui Wu, Qing-Zhen Huang, Jing Wang, Xiao-Li Dong, Guan-Nan Li, Ji-Rong Sun, Fei-Ran Shen, Tong-Yun Zhao, Xin-Qi Zheng, Li-Chen Wang, Yao Liu, Wen-Liang Zuo, Ying-Ying Zhao, Ming Zhang, Xian-Cheng Wang, Chang-Qing Jin, Guang-Hui Rao, Xiu-Feng Han, and Bao-Gen Shen. *Scientific Reports*, 5:18027, 2015.

[134] Juan M. Bermúdez-García, Manuel Sánchez-Andújar, Socorro Castro-García, Jorge López-Beceiro, Ramón Artiaga, and María A. Señarís-Rodríguez. *Nature Communications*, 8:15715, 2017.

[135] N. A. Oliveira. *Appl. Phys. Lett.*, 90:052501, 2007.

[136] H. Wada and Y. Tanabe. *Appl. Phys. Lett.*, 79:3302, 2001.

[137] O. Tegus, E. Bruck, K. H. J. Buschow, and F. R. de Boer. *Nature (London)*, 415: 150, 2002.

[138] X. Zhou, W. Li, H. P. Kunkel, and G. Williams. *J. Phys.: Condens. Matter*, 16:L39, 2004.

[139] Tapas Samanta, Pol Lloveras, Ahmad Us Saleheen, Daniel L. Lepkowski, Emily Kramer, Igor Dubenko, Philip W. Adams, David P. Young, Maria Barrio, Josep Ll. Tamarit, Naushad Ali, and Shane Stadler. *Applied Physics Letters*, 112(2):021907, 2018.

[140] Y. Liu, F.R. Shen, M. Zhang, L.F. Bao, R.R. Wu, Y.Y. Zhao, F.X. Hu, J. Wang, W.L. Zuo, J.R. Sun, and B.G. Shen. *Journal of Alloys and Compounds*, 649:1048 – 1052, 2015.

[141] *Handbook on the Physics and Chemistry of Rare Earths*, volume 12, chapter 83, pages 133–211. Elsevier Science Publishers B.V., 1989.

[142] P. Chandra, P. Coleman, and J. A. Mydosh. *Nature*, 417(Supplement C):831, 2002.

[143] Lingwei Li, Guanghui Hu, Izuru Umehara, Dexuan Huo, Wayne D. Hutchison, Takahiro Namiki, and Katsuhiko Nishimura. *Journal of Alloys and Compounds*, 575:1–4, 2013.

[144] S. Kawano, M. Takahashi, T. Shigeoka, N. Iwata, and T. Kosugi. *Appl. Phys. A*, 74: S646–S648, 2002.

[145] S. Kawano, M. Takahashi, T. Shigeoka, N. Iwata, and M.J. Bull. *Physica B*, 346-347: 99–103, 2004.

[146] B Andreani, G L F Fraga, A Garnier, D Gignoux, D Maurin, D Schmitt, and T Shigeoka. *Journal of Physics: Condensed Matter*, 7:1889–1896, 1995.

[147] N. Iwata, K. Hattori, M. Kadota, M. Takahashi, S. Kawano, and T. Shigeoka. *J. Magn. Magn. Mater.*, 256:189, 2003.

[148] K. Hiebl, C. Horvath, P. Rogl, and M.J. Sienko. *J. Magn. Magn. Mater*, 37:287, 1983.

[149] S. Pramanick, P. Dutta, S. Chatterjee, S. Giri, and S. Majumdar. *Journal of Magnetism and Magnetic Materials*, 405:270 – 273, 2016.

[150] Bibekananda Maji, Mayukh K. Ray, K. G. Suresh, and S. Banerjee. *Journal of Applied Physics*, 116(21):213913, 2014.

[151] Wang Dunhui, Tang Shaolong, Huang Songling, Zhang Jianrong, and Du Youwei. *Journal of Magnetism and Magnetic Materials*, 268:70 – 74, 2004.

[152] X. Chen, Y.H. Zhuang, J.L. Yan, and F. Fei. *Journal of Alloys and Compounds*, 479: 35 – 38, 2009.

[153] N. T. Trung, Z. Q. Ou, T. J. Gortenmulder, O. Tegus, K. H. J. Buschow, and E. Brück. *Applied Physics Letters*, 94:102513, 2009.

[154] V. Franco and A. Conde. *International Journal of Refrigeration*, 33:465 – 473, 2010.

[155] Claudia Marcela Bonilla, Julia Herrero-Albillos, Fernando Bartolomé, Luis Miguel García, María Parra-Borderías, and Victorino Franco. *Phys. Rev. B*, 81:224424, 2010.

[156] Anders Smith, Kaspar K. Nielsen, and Christian R. H. Bahl. *Phys. Rev. B*, 90:104422, 2014.

[157] M. Doerr, M. Rotter, and A. Lindbaum. *Advances in Physics*, 54:1–66, 2005.

[158] S.A. Nikitin, A.M. Tishin, and P.I. Leontiev. *Journal of Magnetism and Magnetic Materials*, 92:405–416, 1991.

[159] S.A. Nikitin, A.M. Tishin, M.D. Kuz'min, and Yu.I. Spichkin. *Physics Letters A*, 153:155–161, 1991.

[160] S.A. Nikitin, D. Kim, and O.D. Chistyakov. *Zh. Eksp. Teor. Fiz*, 71:1610–1619, 1976.

[161] S. A. Nikitin. *Moscow University Physics Bulletin*, 66:519–533, 2011.

[162] S. A. Nikitin and R. V. Bezdushnyĭ. *Sov. Phys. JETP*, 66:1058–1062, 1987.

[163] K Tomala, J P Sanchez, and R Kmieć. *Journal of Physics: Condensed Matter*, 1: 4415–4423, 1989.

[164] T. Samanta, D. L. Lepkowski, A. Us Saleheen, A. Shankar, J. Prestigiacomo, I. Dubenko, A. Quetz, I. W. H. Oswald, G. T. McCandless, J. Y. Chan, P. W. Adams, D. P. Young, N. Ali, and S. Stadler. *Phys. Rev. B*, 91:020401(R), 2015.

[165] J. L. Wang, L. Caron, S. J. Campbell, S. J. Kennedy, M. Hofmann, Z. X. Cheng, M. F. Md Din, A. J. Studer, E. Brück, and S. X. Dou. *Phys. Rev. Lett.*, 110:217211, 2013.

[166] L. Caron, B. Dutta, P. Devi, M. Ghorbani Zavareh, T. Hickel, R. Cabassi, F. Bolzoni, S. Fabbrici, F. Albertini, C. Felser, and Sanjay Singh. *Phys. Rev. B*, 96:054105, 2017.

[167] M. Kataoka, K. Endo, N. Kudo, T. Kanomata, H. Nishihara, T. Shishido, R. Y. Umetsu, M. Nagasako, and R. Kainuma. *Phys. Rev. B*, 82:214423, 2010.

[168] Takuya Ohba, Naohiro Miyamoto, Koudai Fukuda, Takashi Fukuda, Tomoyuki Kakeshita, and Kenichi Kato. *Smart Materials and Structures*, 14:S197, 2005.

[169] The-Long Phan, P. Zhang, N. H. Dan, N. H. Yen, P. T. Thanh, T. D. Thanh, M. H. Phan, and S. C. Yu. *Applied Physics Letters*, 101:212403, 2012.

[170] P. Zhang, T.L. Phan, N.H. Dan, T.D. Thanh, and S.C. Yu. *Journal of Alloys and Compounds*, 615:S335 – S339, 2014.

[171] W.Z. Nan, Tran Dang Thanh, G. Nam, T.S. You, H.G. Piao, L.Q. Pan, and S.C. Yu. *Journal of Magnetism and Magnetic Materials*, 443:171 – 178, 2017.

[172] U Devarajan, M Kannan, R Thiyagarajan, M Manivel Raja, N V Rama Rao, Sanjay Singh, D Venkateshwarlu, V Ganesan, M Ohashi, and S Arumugam. *Journal of Physics D: Applied Physics*, 49:065001, 2016.

[173] A. Ghotbi Varzaneh, P. Kameli, T. Amiri, K.K. Ramachandran, A. Mar, I. Abdolhosseini Sarsari, J.L. Luo, T.H. Etsell, and H. Salamati. *Journal of Alloys and Compounds*, 708:34 – 42, 2017.

[174] Madhumita Halder, S. M. Yusuf, M. D. Mukadam, and K. Shashikala. *Phys. Rev. B*, 81:174402, 2010.

[175] S. Roy, E. Blackburn, S. M. Valvidares, M. R. Fitzsimmons, S. C. Vogel, M. Khan, I. Dubenko, S. Stadler, N. Ali, S. K. Sinha, and J. B. Kortright. *Phys. Rev. B*, 79: 235127, 2009.

[176] V. Sokolovskiy, V. Buchelnikov, K. Skokov, O. Gutfleisch, D. Karpenkov, Yu. Koshkid'ko, H. Miki, I. Dubenko, N. Ali, S. Stadler, and V. Khovaylo. *Journal of Applied Physics*, 114:183913, 2013.

[177] Mahmud Khan, J. Jung, S. S. Stoyko, Arthur Mar, Abdiel Quetz, Tapas Samanta, Igor Dubenko, Naushad Ali, Shane Stadler, and K. H. Chow. *Applied Physics Letters*, 100:172403, 2012.

[178] Mahmud Khan, Igor Dubenko, Shane Stadler, and Naushad Ali. *Journal of Applied Physics*, 97(10):10M304, 2005.

[179] S. R. Barman, S. Banik, and Aparna Chakrabarti. *Phys. Rev. B*, 72:184410, 2005.

[180] Stephen Blundell. *Magnetism in Condensed Matter*, chapter 6. Oxford University Press, 2001.

[181] P. Lampen, M. H. Phan, H. Srikanth, K. Kovnir, P. Chai, and M. Shatruk. *Phys. Rev. B*, 90:174404, 2014.

[182] H. Eugene Stanley. *Introduction to Phase Transitions and Critical Phenomena*, chapter 11. Oxford University Press, 1971.

[183] A. K. Pramanik and A. Banerjee. *Phys. Rev. B*, 79:214426, 2009.

[184] Yantao Su, Yu Sui, J.-G. Cheng, J.-S. Zhou, Xianjie Wang, Yang Wang, and J. B. Goodenough. *Phys. Rev. B*, 87:195102, 2013.

[185] J. Lago, M. J. Rosseinsky, S. J. Blundell, P. D. Battle, M. Diaz, I. Uriarte, and T. Rojo. *Phys. Rev. B*, 83:104404, 2011.

[186] S.N. Kaul. *Journal of Magnetism and Magnetic Materials*, 53:5 – 53, 1985.

[187] Massimo Campostrini, Martin Hasenbusch, Andrea Pelissetto, Paolo Rossi, and Ettore Vicari. *Phys. Rev. B*, 65:144520, 2002.

[188] James S. Kouvel and Michael E. Fisher. *Phys. Rev.*, 136:A1626–A1632, 1964.

[189] B. Widom. *The Journal of Chemical Physics*, 43:3898–3905, 1965.

[190] S. F. Fischer, S. N. Kaul, and H. Kronmüller. *Phys. Rev. B*, 65:064443, 2002.

[191] P D Babu and S N Kaul. *Journal of Physics: Condensed Matter*, 9:7189, 1997.

[192] Manh-Huong Phan, Victorino Franco, Anurag Chaturvedi, Stevce Stefanoski, George S. Nolas, and Hariharan Srikanth. *Phys. Rev. B*, 84:054436, 2011.

[193] V. Franco, J. S. Blázquez, and A. Conde. *Applied Physics Letters*, 89(22):222512, 2006.

[194] Jiyu Fan, Li Pi, Lei Zhang, Wei Tong, Langsheng Ling, Bo Hong, Yangguang Shi, Weichun Zhang, Di Lu, and Yuheng Zhang. *Applied Physics Letters*, 98:072508, 2011.

[195] H. Oesterreicher and F. T. Parker. *Journal of Applied Physics*, 55:4334–4338, 1984.

[196] V Franco, A Conde, J M Romero-Enrique, and J S Blázquez. *Journal of Physics: Condensed Matter*, 20:285207, 2008.

[197] X. B. Liu and Z. Altounian. *Journal of Applied Physics*, 99(8):08Q101, 2006.

[198] Aihua Wang, Yang Liu, Zeyu Zhang, Yi Long, and Guohui Cao. *Solid State Communications*, 130(3):293 – 296, 2004.

[199] V. Franco, J.S. Blázquez, J.J. Ipus, J.Y. Law, L.M. Moreno-Ramírez, and A. Conde. *Progress in Materials Science*, 93:112 – 232, 2018.

[200] Michael E. Fisher, Shang-keng Ma, and B. G. Nickel. *Phys. Rev. Lett.*, 29:917–920, 1972.

[201] Renwen Li, Z. Ma, E. Agurgo Balfour, H. Fu, and Y. Luo. *Journal of Alloys and Compounds*, 658:672 – 677, 2016.

[202] E. Şaşıoğlu, L. M. Sandratskii, and P. Bruno. *Phys. Rev. B*, 77:064417, 2008.

[203] J. F. Duan, Y. Long, B. Bao, H. Zhang, R. C. Ye, Y. Q. Chang, F. R. Wan, and G. H. Wu. *Journal of Applied Physics*, 103(6):063911, 2008.

[204] J. Kübler, A. R. William, and C. B. Sommers. *Phys. Rev. B*, 28:1745–1755, 1983.

Appendix A
Consent Policy

AIP PUBLISHING LICENSE
TERMS AND CONDITIONS

Oct 09, 2018

This Agreement between Mr. Ahmad Us Saleheen ("You") and AIP Publishing ("AIP Publishing") consists of your license details and the terms and conditions provided by AIP Publishing and Copyright Clearance Center.

License Number	4445010165714
License date	Oct 09, 2018
Licensed Content Publisher	AIP Publishing
Licensed Content Publication	Journal of Applied Physics
Licensed Content Title	Effects of hydrostatic pressure on magnetostructural transitions and magnetocaloric properties in (MnNiSi)1−x(FeCoGe)x
Licensed Content Author	Tapas Samanta, Daniel L. Lepkowski, Ahmad Us Saleheen, et al
Licensed Content Date	Mar 28, 2015
Licensed Content Volume	117
Licensed Content Issue	12
Type of Use	Thesis/Dissertation
Requestor type	Author (original article)
Format	Print and electronic
Portion	Excerpt (> 800 words)
Will you be translating?	No
Title of your thesis / dissertation	THE EFFECTS OF PRESSURE AND MAGNETIC FIELD ON PHASE TRANSITIONS AND RELATED PHYSICAL PROPERTIES IN SOLID STATE CALORIC MATERIALS
Expected completion date	Dec 2018
Estimated size (number of pages)	138
Requestor Location	Mr. Ahmad Us Saleheen 752 Jennifer Jean Dr BATON ROUGE, LA 70803 United States Attn: Mr. Ahmad Us Saleheen
Billing Type	Invoice
Billing Address	Mr. Ahmad Us Saleheen 752 Jennifer Jean Dr BATON ROUGE, LA 70803 United States Attn: Mr. Ahmad Us Saleheen
Total	0.00 USD

Terms and Conditions

AIP Publishing -- Terms and Conditions: Permissions Uses

AIP Publishing hereby grants to you the non-exclusive right and license to use and/or distribute the Material according to the use specified in your order, on a one-time basis, for the specified term, with a maximum distribution equal to the number that you have ordered. Any links or other content accompanying the Material are not the subject of this license.

1. You agree to include the following copyright and permission notice with the reproduction of the Material:"Reprinted from [FULL CITATION], with the permission of AIP Publishing." For an article, the credit line and permission notice must be printed on the first page of the article or book chapter. For photographs, covers, or tables, the notice may appear with the Material, in a footnote, or in the reference list.
2. If you have licensed reuse of a figure, photograph, cover, or table, it is your responsibility to ensure that the material is original to AIP Publishing and does not contain the copyright of another entity, and that the copyright notice of the figure, photograph, cover, or table does not indicate that it was reprinted by AIP Publishing, with permission, from another source. Under no circumstances does AIP Publishing purport or intend to grant permission to reuse material to which it does not hold appropriate rights.
   You may not alter or modify the Material in any manner. You may translate the Material

into another language only if you have licensed translation rights. You may not use the Material for promotional purposes.

3. The foregoing license shall not take effect unless and until AIP Publishing or its agent, Copyright Clearance Center, receives the Payment in accordance with Copyright Clearance Center Billing and Payment Terms and Conditions, which are incorporated herein by reference.
4. AIP Publishing or Copyright Clearance Center may, within two business days of granting this license, revoke the license for any reason whatsoever, with a full refund payable to you. Should you violate the terms of this license at any time, AIP Publishing, or Copyright Clearance Center may revoke the license with no refund to you. Notice of such revocation will be made using the contact information provided by you. Failure to receive such notice will not nullify the revocation.
5. AIP Publishing makes no representations or warranties with respect to the Material. You agree to indemnify and hold harmless AIP Publishing, and their officers, directors, employees or agents from and against any and all claims arising out of your use of the Material other than as specifically authorized herein.
6. The permission granted herein is personal to you and is not transferable or assignable without the prior written permission of AIP Publishing. This license may not be amended except in a writing signed by the party to be charged.
7. If purchase orders, acknowledgments or check endorsements are issued on any forms containing terms and conditions which are inconsistent with these provisions, such inconsistent terms and conditions shall be of no force and effect. This document, including the CCC Billing and Payment Terms and Conditions, shall be the entire agreement between the parties relating to the subject matter hereof.

This Agreement shall be governed by and construed in accordance with the laws of the State of New York. Both parties hereby submit to the jurisdiction of the courts of New York County for purposes of resolving any disputes that may arise hereunder.

V1.2

Questions? customercare@copyright.com or +1-855-239-3415 (toll free in the US) or +1-978-646-2777.

AIP PUBLISHING LICENSE
TERMS AND CONDITIONS

Oct 09, 2018

This Agreement between Mr. Ahmad Us Saleheen ("You") and AIP Publishing ("AIP Publishing") consists of your license details and the terms and conditions provided by AIP Publishing and Copyright Clearance Center.

License Number	4445010473079
License date	Oct 09, 2018
Licensed Content Publisher	AIP Publishing
Licensed Content Publication	Applied Physics Letters
Licensed Content Title	Barocaloric and magnetocaloric effects in (MnNiSi)1−x(FeCoGe)x
Licensed Content Author	Tapas Samanta, Pol Lloveras, Ahmad Us Saleheen, et al
Licensed Content Date	Jan 8, 2018
Licensed Content Volume	112
Licensed Content Issue	2
Type of Use	Thesis/Dissertation
Requestor type	Author (original article)
Format	Print and electronic
Portion	Excerpt (> 800 words)
Will you be translating?	No
Title of your thesis / dissertation	THE EFFECTS OF PRESSURE AND MAGNETIC FIELD ON PHASE TRANSITIONS AND RELATED PHYSICAL PROPERTIES IN SOLID STATE CALORIC MATERIALS
Expected completion date	Dec 2018
Estimated size (number of pages)	138
Requestor Location	Mr. Ahmad Us Saleheen 752 Jennifer Jean Dr BATON ROUGE, LA 70803 United States Attn: Mr. Ahmad Us Saleheen
Billing Type	Invoice
Billing Address	Mr. Ahmad Us Saleheen 752 Jennifer Jean Dr BATON ROUGE, LA 70803 United States Attn: Mr. Ahmad Us Saleheen
Total	0.00 USD

Terms and Conditions

AIP Publishing -- Terms and Conditions: Permissions Uses

AIP Publishing hereby grants to you the non-exclusive right and license to use and/or distribute the Material according to the use specified in your order, on a one-time basis, for the specified term, with a maximum distribution equal to the number that you have ordered. Any links or other content accompanying the Material are not the subject of this license.

1. You agree to include the following copyright and permission notice with the reproduction of the Material:"Reprinted from [FULL CITATION], with the permission of AIP Publishing." For an article, the credit line and permission notice must be printed on the first page of the article or book chapter. For photographs, covers, or tables, the notice may appear with the Material, in a footnote, or in the reference list.
2. If you have licensed reuse of a figure, photograph, cover, or table, it is your responsibility to ensure that the material is original to AIP Publishing and does not contain the copyright of another entity, and that the copyright notice of the figure, photograph, cover, or table does not indicate that it was reprinted by AIP Publishing, with permission, from another source. Under no circumstances does AIP Publishing purport or intend to grant permission to reuse material to which it does not hold appropriate rights.
   You may not alter or modify the Material in any manner. You may translate the Material into another language only if you have licensed translation rights. You may not use the

Material for promotional purposes.

3. The foregoing license shall not take effect unless and until AIP Publishing or its agent, Copyright Clearance Center, receives the Payment in accordance with Copyright Clearance Center Billing and Payment Terms and Conditions, which are incorporated herein by reference.
4. AIP Publishing or Copyright Clearance Center may, within two business days of granting this license, revoke the license for any reason whatsoever, with a full refund payable to you. Should you violate the terms of this license at any time, AIP Publishing, or Copyright Clearance Center may revoke the license with no refund to you. Notice of such revocation will be made using the contact information provided by you. Failure to receive such notice will not nullify the revocation.
5. AIP Publishing makes no representations or warranties with respect to the Material. You agree to indemnify and hold harmless AIP Publishing, and their officers, directors, employees or agents from and against any and all claims arising out of your use of the Material other than as specifically authorized herein.
6. The permission granted herein is personal to you and is not transferable or assignable without the prior written permission of AIP Publishing. This license may not be amended except in a writing signed by the party to be charged.
7. If purchase orders, acknowledgments or check endorsements are issued on any forms containing terms and conditions which are inconsistent with these provisions, such inconsistent terms and conditions shall be of no force and effect. This document, including the CCC Billing and Payment Terms and Conditions, shall be the entire agreement between the parties relating to the subject matter hereof.

This Agreement shall be governed by and construed in accordance with the laws of the State of New York. Both parties hereby submit to the jurisdiction of the courts of New York County for purposes of resolving any disputes that may arise hereunder.

V1.2

Questions? customercare@copyright.com or +1-855-239-3415 (toll free in the US) or +1-978-646-2777.

AIP PUBLISHING LICENSE
TERMS AND CONDITIONS

Oct 09, 2018

This Agreement between Mr. Ahmad Us Saleheen ("You") and AIP Publishing ("AIP Publishing") consists of your license details and the terms and conditions provided by AIP Publishing and Copyright Clearance Center.

License Number	4445010710332
License date	Oct 09, 2018
Licensed Content Publisher	AIP Publishing
Licensed Content Publication	Journal of Applied Physics
Licensed Content Title	The influence of hydrostatic pressure on the magnetic and magnetocaloric properties of DyRu2Si2
Licensed Content Author	Ahmad Us Saleheen, Tapas Samanta, Mojammel Khan, et al
Licensed Content Date	Jan 28, 2017
Licensed Content Volume	121
Licensed Content Issue	4
Type of Use	Thesis/Dissertation
Requestor type	Author (original article)
Format	Print and electronic
Portion	Excerpt (> 800 words)
Will you be translating?	No
Title of your thesis / dissertation	THE EFFECTS OF PRESSURE AND MAGNETIC FIELD ON PHASE TRANSITIONS AND RELATED PHYSICAL PROPERTIES IN SOLID STATE CALORIC MATERIALS
Expected completion date	Dec 2018
Estimated size (number of pages)	138
Requestor Location	Mr. Ahmad Us Saleheen 752 Jennifer Jean Dr BATON ROUGE, LA 70803 United States Attn: Mr. Ahmad Us Saleheen
Billing Type	Invoice
Billing Address	Mr. Ahmad Us Saleheen 752 Jennifer Jean Dr BATON ROUGE, LA 70803 United States Attn: Mr. Ahmad Us Saleheen
Total	0.00 USD

Terms and Conditions

AIP Publishing -- Terms and Conditions: Permissions Uses

AIP Publishing hereby grants to you the non-exclusive right and license to use and/or distribute the Material according to the use specified in your order, on a one-time basis, for the specified term, with a maximum distribution equal to the number that you have ordered. Any links or other content accompanying the Material are not the subject of this license.

1. You agree to include the following copyright and permission notice with the reproduction of the Material:"Reprinted from [FULL CITATION], with the permission of AIP Publishing." For an article, the credit line and permission notice must be printed on the first page of the article or book chapter. For photographs, covers, or tables, the notice may appear with the Material, in a footnote, or in the reference list.
2. If you have licensed reuse of a figure, photograph, cover, or table, it is your responsibility to ensure that the material is original to AIP Publishing and does not contain the copyright of another entity, and that the copyright notice of the figure, photograph, cover, or table does not indicate that it was reprinted by AIP Publishing, with permission, from another source. Under no circumstances does AIP Publishing purport or intend to grant permission to reuse material to which it does not hold appropriate rights.
   You may not alter or modify the Material in any manner. You may translate the Material

AIP PUBLISHING LICENSE
TERMS AND CONDITIONS

Oct 09, 2018

This Agreement between Mr. Ahmad Us Saleheen ("You") and AIP Publishing ("AIP Publishing") consists of your license details and the terms and conditions provided by AIP Publishing and Copyright Clearance Center.

License Number	4445010605232
License date	Oct 09, 2018
Licensed Content Publisher	AIP Publishing
Licensed Content Publication	Journal of Applied Physics
Licensed Content Title	Critical behavior in Ni2MnGa and Ni2Mn0.85Cu0.15Ga
Licensed Content Author	Ahmad Us Saleheen, Jing-Han Chen, David P. Young, et al
Licensed Content Date	May 28, 2018
Licensed Content Volume	123
Licensed Content Issue	20
Type of Use	Thesis/Dissertation
Requestor type	Author (original article)
Format	Print and electronic
Portion	Excerpt (> 800 words)
Will you be translating?	No
Title of your thesis / dissertation	THE EFFECTS OF PRESSURE AND MAGNETIC FIELD ON PHASE TRANSITIONS AND RELATED PHYSICAL PROPERTIES IN SOLID STATE CALORIC MATERIALS
Expected completion date	Dec 2018
Estimated size (number of pages)	138
Requestor Location	Mr. Ahmad Us Saleheen 752 Jennifer Jean Dr BATON ROUGE, LA 70803 United States Attn: Mr. Ahmad Us Saleheen
Billing Type	Invoice
Billing Address	Mr. Ahmad Us Saleheen 752 Jennifer Jean Dr BATON ROUGE, LA 70803 United States Attn: Mr. Ahmad Us Saleheen
Total	0.00 USD

Terms and Conditions

AIP Publishing -- Terms and Conditions: Permissions Uses

AIP Publishing hereby grants to you the non-exclusive right and license to use and/or distribute the Material according to the use specified in your order, on a one-time basis, for the specified term, with a maximum distribution equal to the number that you have ordered. Any links or other content accompanying the Material are not the subject of this license.

1. You agree to include the following copyright and permission notice with the reproduction of the Material:"Reprinted from [FULL CITATION], with the permission of AIP Publishing." For an article, the credit line and permission notice must be printed on the first page of the article or book chapter. For photographs, covers, or tables, the notice may appear with the Material, in a footnote, or in the reference list.
2. If you have licensed reuse of a figure, photograph, cover, or table, it is your responsibility to ensure that the material is original to AIP Publishing and does not contain the copyright of another entity, and that the copyright notice of the figure, photograph, cover, or table does not indicate that it was reprinted by AIP Publishing, with permission, from another source. Under no circumstances does AIP Publishing purport or intend to grant permission to reuse material to which it does not hold appropriate rights.
   You may not alter or modify the Material in any manner. You may translate the Material into another language only if you have licensed translation rights. You may not use the

Material for promotional purposes.

3. The foregoing license shall not take effect unless and until AIP Publishing or its agent, Copyright Clearance Center, receives the Payment in accordance with Copyright Clearance Center Billing and Payment Terms and Conditions, which are incorporated herein by reference.
4. AIP Publishing or Copyright Clearance Center may, within two business days of granting this license, revoke the license for any reason whatsoever, with a full refund payable to you. Should you violate the terms of this license at any time, AIP Publishing, or Copyright Clearance Center may revoke the license with no refund to you. Notice of such revocation will be made using the contact information provided by you. Failure to receive such notice will not nullify the revocation.
5. AIP Publishing makes no representations or warranties with respect to the Material. You agree to indemnify and hold harmless AIP Publishing, and their officers, directors, employees or agents from and against any and all claims arising out of your use of the Material other than as specifically authorized herein.
6. The permission granted herein is personal to you and is not transferable or assignable without the prior written permission of AIP Publishing. This license may not be amended except in a writing signed by the party to be charged.
7. If purchase orders, acknowledgments or check endorsements are issued on any forms containing terms and conditions which are inconsistent with these provisions, such inconsistent terms and conditions shall be of no force and effect. This document, including the CCC Billing and Payment Terms and Conditions, shall be the entire agreement between the parties relating to the subject matter hereof.

This Agreement shall be governed by and construed in accordance with the laws of the State of New York. Both parties hereby submit to the jurisdiction of the courts of New York County for purposes of resolving any disputes that may arise hereunder.

V1.2

Questions? customercare@copyright.com or +1-855-239-3415 (toll free in the US) or +1-978-646-2777.

Vita

Ahmad Ikhwan Us Saleheen was born in Bangladesh, and received his bachelor's degree in physics from the University of Dhaka in 2009. He had started his doctoral studies at the Louisiana State University in the fall of 2011, under the supervision of Professor Shane Stadler. His research interests are in magneto- and barocaloric effects, magnetic phase transitions, rare-earth compounds, Heusler alloys, and so on. His PhD in experimental condensed matter physics is in progress, and he is expecting to graduate in December 2018. Currently, he is looking forward to conduct research as a postdoctoral researcher.